공학박사 학위논문

Metal-graphene oxide coordination network

금속-산화그래핀 결합 네트워크

2016년 8월

서울대학교 대학원

기계항공공학부

김 태 우

Abstract

Metal-graphene oxide coordination network

Taewoo Kim
School of Mechanical and Aerospace Engineering
Seoul National University

Three-dimensional (3-D) macroscopic graphene structures are quite attractive for various applications where large specific surface area, high porosity, low density, and outstanding electrochemical performance are needed. 3-D graphene structures have been used as energy harvester, energy storage device, stretchable electronics, sensor, cell growth scaffold, and oil absorber, showing outstanding performances compared to conventional materials and devices.

Here, an ion-mediated assembly (IMA) method is developed for a substrate-initiated assembly of 3-D graphene structures. In particular, metal ions dissolved from a metal substrate by an applied voltage bring about the formation of 3-D graphene structures in the form of a coordination network of the metal and graphene oxide. Fabrication mechanism of metal-graphene oxide coordination network (MGCN) and its basic properties were investigated and discussed. The dimension and interior structure of MGCN can be precisely controlled by varying the process parameters of IMA.

The ability to fabricate a 3-D graphene structure on a substrate could help open various attractive applications. In this thesis, three applications were demonstrated with the characteristic features of MGCN including selective capillarity, countless sharp edges, and expanded thermal convection.

MGCN formed on a mesh was used as an oil permeable filter to separate oil and water with its selective capillarity. Countless sharp edges of MGCN were utilized to make high performance field emitter. Cylindrical and planer field emitters were fabricated by forming MGCN on metal rod and plate, respectively. MGCN formed on copper or aluminum block showed outstanding heat dissipation performance with enhanced heat transfer coefficient which comes from expanded thermal convection by MGCN.

Keywords: ion-mediated assembly, three-dimensional structure, coordination network, metal-graphene oxide coordination, gelation, graphene

Student Number: 2008-20727

Contents

List of Tables

List of Figures

Chapter 1. Introduction

Graphene, one-atom-thick carbon material, has attracted much attention because of its extraordinary electrical [1], mechanical [2], and thermal [3] properties. Assembly of the two-dimensional graphene into three-dimensional (3-D) macroscopic structures is quite attractive for various applications where large specific surface area, high porosity, low density, and outstanding electrochemical performance are needed. Therefore, the 3-D structures have been used as energy harvester [4, 5], supercapacitor [6, 7], Li-battery [8, 9], stretchable electronics [10], sensors [11], cell growth scaffold [12], and oil absorber [13-15].

Various techniques for the preparation of 3-D graphene structures have been reported including leavening process [16], chemical activation [17], templated-directed chemical vapor deposition [10], ice-templated synthesis [18], templated-directed assembly [19, 20], laser scribing [6], and gelation of graphene oxide (GO) by hydrothermal process [7, 21] and sol-gel reaction [22, 23]. The gelation of GO, in particular, has been studied extensively because it is an industrially scalable process.

Most gelation methods, however, provide only a bulk 3-D graphene structure. For applications involving substrates, therefore, an additional adhesion process is needed to bond the 3-D structure to a substrate. This restriction placed a limit in applications related to energy storage [24-26] and oil absorber [13, 15].

The ability to fabricate a 3-D graphene structure on a substrate could help open various attractive applications. For example, a graphene structure formed on a mesh can be used as an oil permeable filter to separate oil and water in addition to absorbing oil. For another, a vertically oriented graphene structure on a metal plate can be utilized as a high performance field emitter for terahertz (THz) generator. Such a structure would also be a good candidate for a heat dissipation material.

Developed here is an ion-mediated assembly (IMA) for a substrate-initiated assembly of 3-D graphene structures. In particular, metal ions dissolved from a metal substrate by an applied voltage bring about the formation of 3-D graphene structures in the form of a three-dimensional coordination network of the metal and a graphene derivative, which is graphene oxide (GO) here. This metal-graphene oxide coordination network (MGCN) can be formed on a plate, rod, wire, foil, or even mesh substrate, providing flexibility to meet the needs of applications. The dimension and interior structure of MGCN can be precisely controlled for a given application.

In this thesis, fabrication mechanism and basic properties of MGCN are investigated. Moreover, the characteristic features of MGCN, including selective capillarity, countless sharp edges, and expanded thermal convection, are investigated and utilized for practical applications.

Chapter 2. Three-dimensional metal-graphene oxide network

In this chapter, ion-mediated assembly (IMA) method is developed for the fabrication of 3-D metal-graphene oxide coordination network (MGCN) on metal substrates. Fabrication mechanism, structure of MGCN, and process parameters of IMA are discussed. Basic properties of MGCN, including morphology, chemical structure, and physical properties, are investigated and discussed.

2.1 Gelation of graphene oxide

2.1.1 Graphene oxide

Graphene oxide (GO), a chemically modified graphene, has been studied extensively in recent years in many different fields because of its exceptional characteristics [27-30]. GO is a two-dimensional structure of carbon atoms decorated with abundant oxygen functional groups on both basal planes and edges such as hydroxyl, epoxy, carbonyl, and carboxyl groups. As shown in Figure 2-1, GO retains the layer structure of graphene or graphite although there has been considerable debate among scholars over the structure of GO.

The morphology and structural features of GO have been revealed by atomic force microscopy (AFM) [31, 32], transmission electron microscopy (TEM) [33], and scanning tunneling microscopy (STM) [34-36]. AFM gives the lateral dimension and apparent thickness of GO as shown in Figure 2-2(a). The lateral size ranges from several hundred nanometers to several micrometers. The apparent thickness of GO monolayer is around 1 nm much larger than that of graphene (0.34 nm), which comes from its puckered plane, oxygen functional groups, and absorbed water molecules [37]. GO is comprised of three major regions having different atomic structures as shown in Figure 2-2(b), (c). The regions are; 1) graphitic region: it has the original honeycomb-lattice structure of graphene. 2) disordered region: carbon atoms in this region are covalently bonded with oxygen functional groups. 3) hole: large defect.

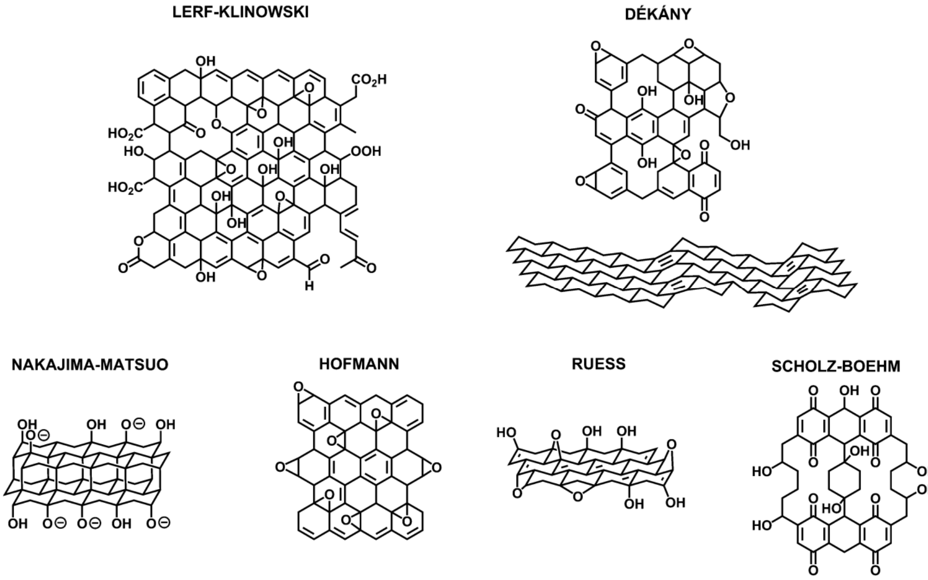

LERF-KLINOWSKI

DÉKÁNY

NAKAJIMA-MATSUO

HOFMANN

RUESS

SCHOLZ-BOEHM

Figure 2-1. Structural models of GO that have been proposed [38].

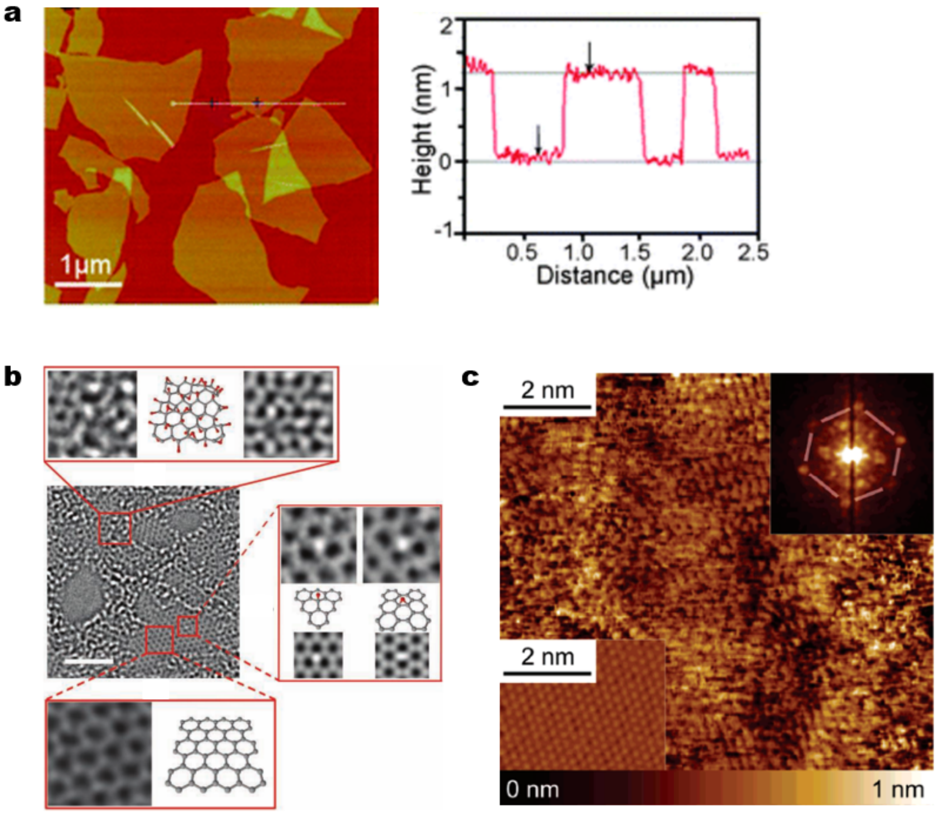

Figure 2-2. (a) AFM image of GO [31]. (b) Aberration-corrected TEM image of GO [33]. The scale bar is 2 nm. (c) STM image of GO [36]. Inset on the right top is the Fourier transform of the image. Inset on the left bottom is the image of highly oriented pyrolytic graphite.

The chemical composition of GO has been investigated using a variety of spectroscopies including solid-state nuclear magnetic resonance spectroscopy (SSNMR) [39-41], X-ray photoelectron spectroscopy (XPS) [39, 42, 43], Raman spectroscopy [36, 43], and Fourier transform infrared spectroscopy (FT-IR) [41, 42] as shown in Figure 2-3. Predominant chemical bonds in GO are identified to be C=C (sp^2 carbon), C-OH (hydroxyl group), C-O-C (epoxy group), C=O (carbonyl group), and COOH (carboxyl group). The degree of oxidation is dependent on synthesis methods of GO (oxidant agents, oxidation time, and temperature). The oxygen content of GO typically ranges from 20 to 40 at% [44-46]. Abundant oxygen functional groups provide chemically reactive sites for functionalization and make aqueous GO colloidal solution stable.

Synthetic methods for producing GO involves oxidation of a graphitic material followed by exfoliation. The typical oxidizing reagents are $KMnO_4$, H_2SO_4 [47-50] or $KClO_3$, HNO_3 [51-53]. Table 1 shows the summary of synthetic methods previously reported [38]. Carbon-to-oxygen ratio is affected by synthetic methods as mentioned above.

In contrast to graphene which has high electrical conductivity and solubility in organic solvents, GO shows high electrical resistance and high solubility in water rather than in organic solvents. This differences mostly come from oxygen functional groups and the break of conjugated network of graphitic lattice. Therefore, GO can partially recover or tune the properties of graphene including electrical conductivity and hydrophobicity by a reduction process [46]. Common reduction methods are thermal and chemical reduction. Thermal reduction method, such as thermal annealing [54, 55], microwave [56] and photo reduction [57], is suitable for the reduction of 3-D structure or film because of its dry process. On the other hands, chemical reduction using chemical reagents [58, 59] is more efficient to reduce GO sheets dispersed in a solvent.

Table 1. Summary of synthetic methods for producing GO [38].

Method	Oxidant	Reaction media	Carbon-to-oxygen ratio
Staudenmaier [52]	$KClO_3$	Fuming HNO_3	1.17
Brodie [51]	$KClO_3$	$HNO_3 + H_2SO_4$	-
Hofmann [53]	$KClO_3$	HNO_3	1.15
Hummers [47]	$KMnO_4 + NaNO_3$	H_2SO_4	0.84
Tour [50]	$KMnO_4$	$H_2SO_4 + H_3PO_4$	0.74

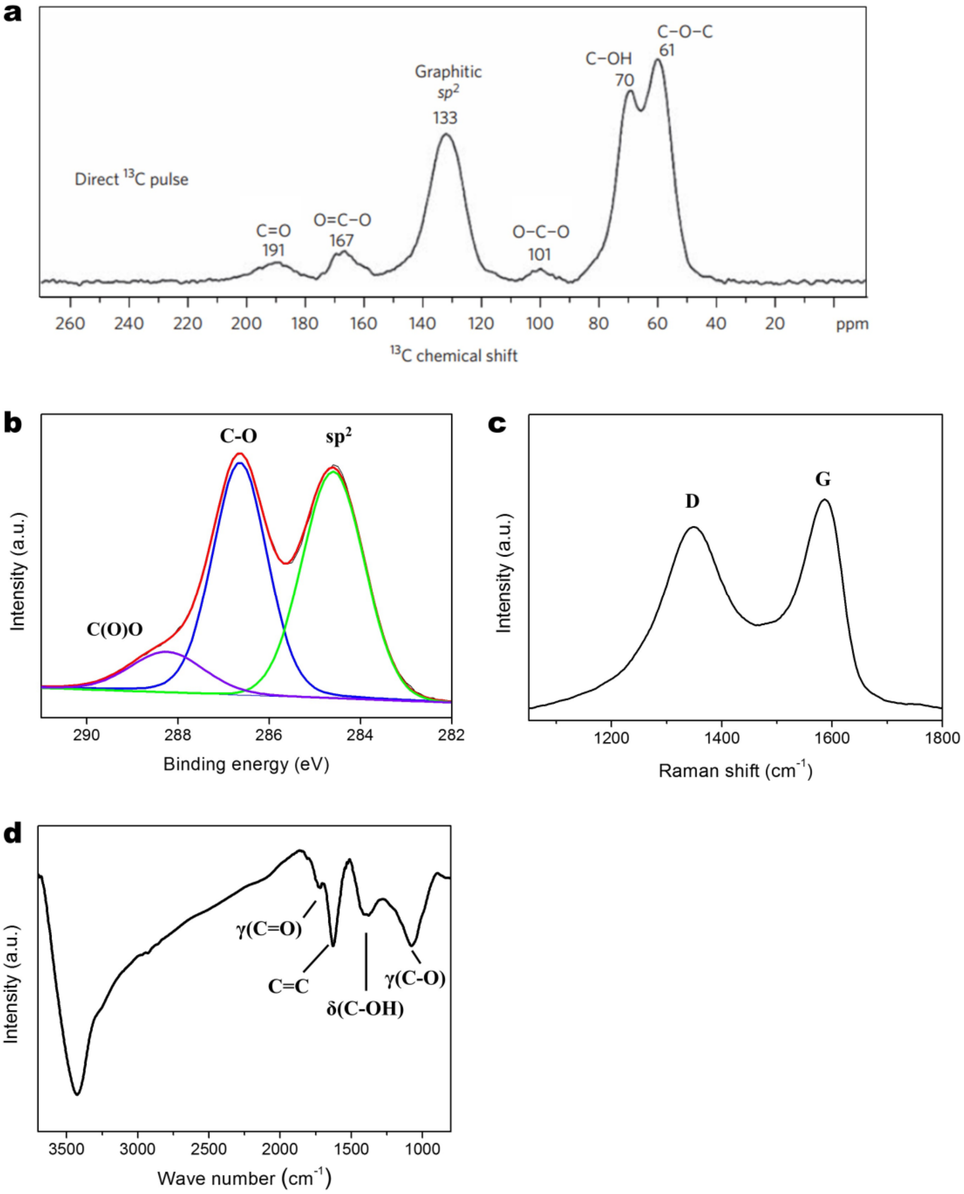

Figure 2-3. (a) SSNMR spectrum of GO [39]. (b) XPS spectrum of GO. (c) Raman spectrum of GO. (d) FT-IR spectrum of GO.

2.1.2 Gelation of graphene oxide by reduction

High solubility and stability of GO in water are attributed to oxygen functional groups bounded to the edges and basal plane of GO sheets. Reduced graphene oxide (rGO) sheets in water are unstable and aggregate themselves above the critical concentration of 0.5 mg mL^{-1} because of their hydrophobic basal plane [58]. Therefore, the reduction of GO dispersed in water would be a strategy to induce gelation of GO sheets to form a rGO hydrogel. The reduction results in hydrophobic and π-π interactions between GO sheets, hydrogen bonding interactions between functional groups.

Hydrothermal process is a powerful technique for fabricating a rGO hydrogel through thermal reduction [7, 21, 60]. 1 mg mL^{-1} (or higher) GO aqueous solution in a Teflon-lined autoclave is heated at 180 ^{o}C for 1-12 hours. During the process, oxygen functional groups are eliminated, thereby causing π-π stacking interactions between rGO sheets. rGO hydrogel has interconnected 3-D porous network where the sheets are partially overlapped and coalesced as shown in Figure 2-4(a). Dimension of rGO hydrogel varies depending on the concentration of GO aqueous solution and process time. Hydrothermal process with low concentration produces a powdery material rather than 3-D structure.

Chemical reduction has been also utilized to make a rGO hydrogel [8, 61, 62] (Figure 2-4(b)). In contrast to hydrothermal process, chemical reduction-induced gelation is commonly performed at relatively low temperature below 100 ^{o}C at atmosphere condition. Various reducing agents, including HI, Na_2S, Vitamin C, and $NaHSO_3$, can be used to induce gelation of GO which takes only 10-30 min.

Furthermore, chemical reduction make a graphene structure having high carbon-to-oxygen ratio and electrical conductivity compared to hydrothermal process. Dimension and density of rGO hydrogel varies depending on the concentration of reducing agents. High concentration of reducing agent causes a large degree of shrinkage of rGO hydrogel, thereby yielding high density.

Spontaneous electrochemical reduction method uses spontaneous reaction of GO with active metals (Cu, Fe, and Al) [63, 64]. The reaction between GO and rGO has the relatively high redox potential of 0.4-0.6 V which is higher than that of active metals. Therefore, GO which encounters an active metal is spontaneously reduced to rGO, oxidizing the active metal (Figure 2-4(c)). The thickness of hydrogel increases with the immersion time of an active metal substrate in GO solution, however, the growth rate gradually decreases with time due to the screening effect of hydrogel formed earlier.

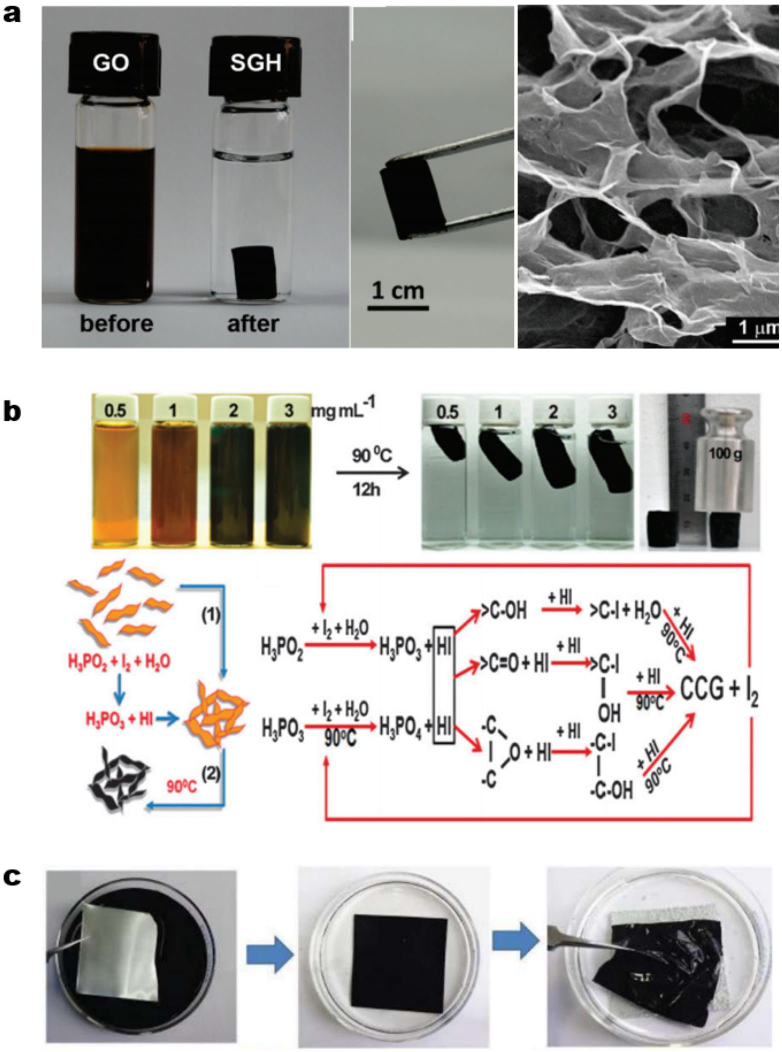

Figure 2-4. (a) Optical and scanning electron microscope (SEM) images of rGO hydrogel fabricated by hydrothermal process [7]. (b) Synthesis of rGO hydrogel through chemical reduction [61]. (c) Procedure of spontaneous electrochemical reduction for fabricating rGO hydrogel [64].

2.1.3 Gelation of graphene oxide by cross-linker

Abundant oxygen functional groups on GO act as cross-linking sites for gelation of GO. Poly(vinyl alcohol) (PVA), a typical water-soluble polymer, was first used as a cross-linker to induce gelation of GO [65]. Shaking and sonication of GO/PVA mixed aqueous solution result in the hydrogen bonding interaction between hydroxyl groups in PVA and oxygen functional groups on GO. GO/PVA hybrid hydrogel is formed as PVA plays the role of a cross-linker interconnecting GO sheets. Because cross-linking by the hydrogen bonding interaction competes with electrostatic repulsion between negative functional groups on GO sheets, pH modulates gelation of GO/PVA solution through the adsorption and dissociation of hydrogen ions from oxygen functional groups (Figure 2-5(a)). For example, with the addition of NaOH aqueous solution to GO/PVA hydrogel, the hydrogel promptly decomposes to GO/PVA aqueous solution due to the dissociation of hydrogen and corresponding increase of electrostatic repulsion force. Besides PVA, a variety of polymer including Poly(vinyl pyrrolidone) (PVP), poly(ethylene oxide) (PEO), polydimethyldiallylammonium chloride (PDDA), polyethylenimine (PEI), cetyltrimethyl ammonium bromide (CTAB), tetramethylammonium chloride (TMAC), and glutaraldehyde (GAD) can be used to promote the gelation of GO [66, 67]. Biomolecules such as DNA, amino acid, hemoglobin, and peptide are also known to be cross-linkers for the gelation.

Metal ions are also efficient cross-linker (Figure 2-5(b)). Divalent ions of Ca^{2+}, Ni^{2+}, and Co^{2+} were first reported as cross-linkers to form graphene hydrogel with the aid of low temperature hydrothermal method (at 120 °C) [68]. Trivalent ions (Cr^{3+}, Fe^{3+}, and La^{3+}) can also act as cross-linker [66, 69, 70]. In contrast to divalent and trivalent ions, univalent metal ions of Li^+, K^+, and Ag^+ cannot fabricate GO hydrogel due to their low coordination stability constant. The gelation of GO induced by metal ions is also controlled like GO/PVA hybrid hydrogel [66, 70]. As shown in Figure 2-5(c), the addition of ethylenediaminetetraacetic acid (EDTA) solution makes GO hydrogel decompose because metal ion is favorable to coordinate with EDTA rather than GO sheets.

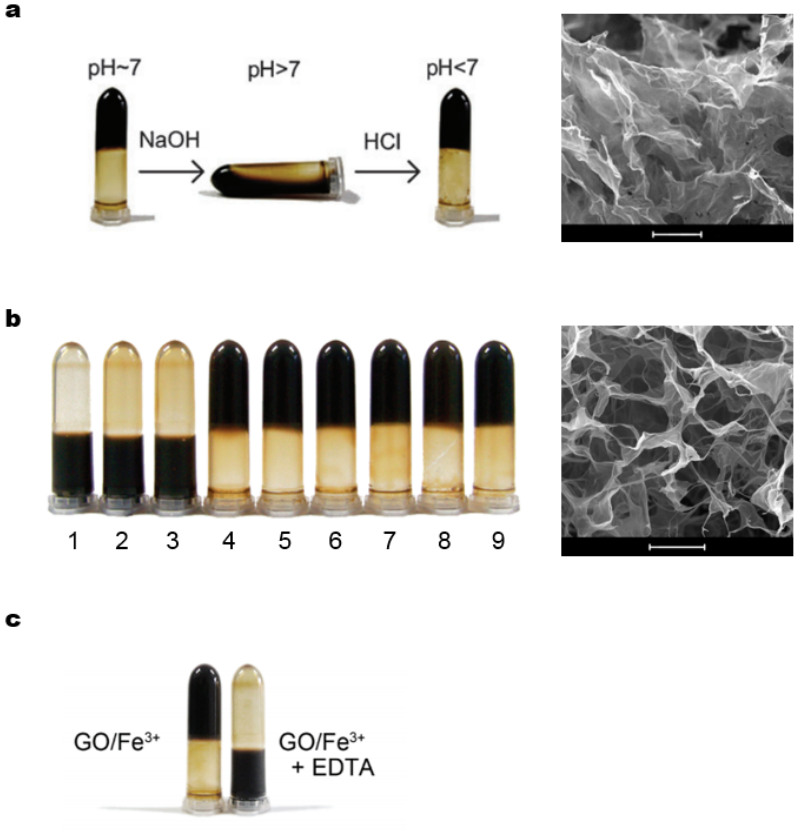

Figure 2-5. (a) Left: Optical image of the pH-induced gel–sol transition. Right: SEM image of GO/PVA hybrid structure [65]. The scale bar is 5 μm. (b) Left: Optical image of GO hydrogel assembled by 1) Li^+, 2) K^+, 3) Ag^+, 4) Mg^{2+}, 5) Ca^{2+}, 6) Cu^{2+}, 7) Pb^{2+}, 8) Cr^{3+}, and 9) Fe^{3+}. Right: SEM image of GO structure assembled by Ca^{2+} [66]. The scale bar is 10 μm. (c) Optical image of gel–sol transition through the addition of EDTA solution [66].

2.2 Fabrication of 3-D metal-graphene oxide network

2.2.1 Fabrication and characterization of graphene oxide

A solution mixture of 0.6 g of graphite powder (Bay Carbon, SP-1), 80 mL of sulfuric acid, and 3.6 g of potassium permanganate in a beaker was stirred for 3-6 hours at 45 ^{o}C. The solution was neutralized by deionized water and hydrogen peroxide. This brown solution was subjected to dialysis to completely remove any residual acid and salt in the solution. GO powders in the form of paper were prepared via a filtration process. This involved vacuum filtering a GO suspension in deionized water onto a membrane filter (Millipore PTFE filter, 0.45 μm pore size, 47 mm diameter), drying in a vacuum chamber, and removal of the formed sheet from the filter. Afterwards, the GO powder was re-dispersed in deionized water with a controlled concentration of 1-5 mg mL^{-1} by sonication. The resulting suspension yields stable colloidal suspensions of individual GO platelets due to the presence of oxygen functional groups [58].

The lateral dimensions of GO range from several hundred nanometers to several micrometers, which was measured from atomic force microscopy (AFM) images (Figure 2-6(a)). The distribution of lateral dimensions was investigated by using controlled centrifugation. 2-3 μm, 1-2 μm, and 0-1 μm long GO sheets were 43 wt%, 35 wt%, and 22 wt%, respectively. The thickness of GO is about 0.8 nm much larger than that of graphene (0.34 nm) due to its deformed layer structure and oxygen functional groups (Figure 2-6(b)). X-ray diffraction (XRD) pattern shown in Figure 2-6(c) shows that the distance between GO sheets is ~0.83 nm.

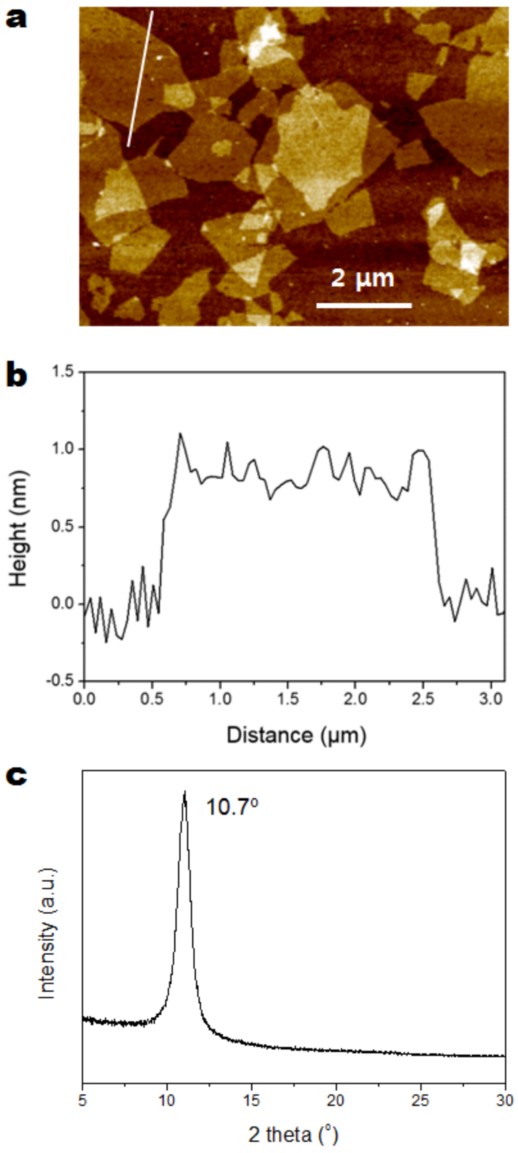

Figure 2-6. (a) AFM image of GO. (b) Height versus distance graph obtained along the white line in the AFM image of (a). (c) XRD pattern of GO.

Figure 2-7 (a) shows X-ray photoelectron spectroscopy (XPS) spectrum of GO. In the core-level C1s XPS spectrum, sp^2 C=C bond at 284.6 eV and epoxy C-O bond at 286.5 eV are predominant with hydroxyl C-O bond at 285.6 eV, carbonyl C=O bond at 287.9 eV, and carboxyl O=C-O bond at 289.0 eV [71-73]. Fourier transform infrared spectroscopy (FT-IR) spectrum also shows that GO has aromatic C=C (1610 cm^{-1}), epoxy C-O (1230 cm^{-1}), alkoxy C-O (1050 cm^{-1}), and carboxyl C=O (1730 cm^{-1}) groups as shown in Figure 2-7(b) [74].

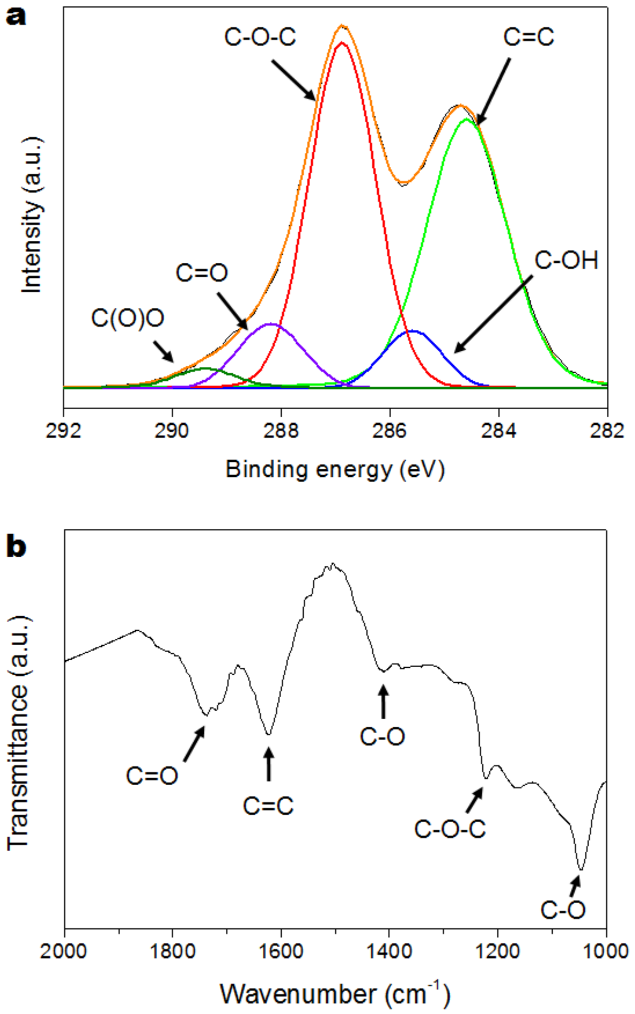

Figure 2-7. (a) XPS spectrum of GO. (b) FT-IR spectrum of GO.

2.2.2 Ion-mediated assembly

A newly developed method to assemble GO, called ion-mediated assembly (IMA), uses metal ion as a cross-linker. Previous cross-linker induced assembly used divalent and trivalent metal ions dissolved from metal salts (section 2.1.3) to link GO sheets. In contrast, IMA utilizes the anodic dissolution of metal, an electrochemical reaction in which metal ions dissolve from metal lattice to solution, to get metal ions. Metal ions dissolved from an anode interconnect GO sheets to form 3-D metal-graphene oxide coordination network on the anode as shown in Figure 2-8(a).

Representative experiment procedures are as in the following: GO powder was synthesized from graphite via the modified Hummers method [75] and dispersed in deionized water using ultra-sonication to get a homogeneous GO colloidal solution. Two identical copper electrodes were immersed into the solution as a cathode and an anode to supply copper ions to the GO solution. A constant dc voltage of 1-10 V was applied between the electrodes for short time (10-60 sec). GO sheets were attracted to the positive electrode (anode) by electrostatic force. More importantly, the voltage applied between the electrodes made copper ions (*i.e.* cuprous and cupric ion) dissolve from the positive electrode (anode). As copper ions interconnect GO sheets, metal-GO coordination network (MGCN) was formed on the surface of anode. Figure 2-8(b) shows the optical image of MGCN hydrogel uniformly formed on the anode.

After IMA process, the hydrogel was immediately dried using a vacuum freeze dryer (Ilshin, FDS-5508) or a vacuum furnace (custom made furnace). The obtained GO aerogel was annealed in vacuum (under 10^{-2} Torr, vacuum furnace) at

200 ^{o}C for several hours to eliminate remaining water molecules and oxygen functional groups.

Figure 2-9 shows a proposed structure model of MGCN based on the spectroscopy results (in section 2.3.2). Divalent metal ions are bound to oxygen functional groups on GO sheets, resulting in cross-linking of neighboring sheets. Lewis acidic metal ions induce ring-opening reaction of epoxy groups to make hydroxyl groups [71, 76]. Carbonyl and carboxyl groups are also coordinated with metal ions, which weakens C=O bond character [77, 78]. In particular, it was identified from infrared spectroscopy study (See section 2.3.2) that the bonds between carboxyl groups and metal ions are bidentate and bridging coordination. Although considerable oxygen functional groups take part in the interactions with the metal ions, some groups remain intact. Most GO sheets are connected via metal ions without the direct interconnection between GO sheets, thereby forming metal-GO coordination network.

Cross-linking degree can be estimated from the content of metal ions in MGCN. The content of metal ions ranges from 3.7 to 5.3 at% (metal: Cu) influenced by process variables such as applied voltage and GO concentration. The relationship between the content and process variables is shown in Figure 2-27.

Electrochemical reduction occurs during IMA process. Carbon to oxygen atomic ratio increases from 1.1 (GO) to 1.4 (MGCN) by reduction of GO. The most likely explanations for the reduction are spontaneous electrochemical reduction of GO [63, 79] and Kolbe reaction [76, 80]. The reduction potential of GO/rGO (~0.78 V vs. normal hydrogen electrode (NHE)) is much higher than those of Cu/Cu^{2+} (0.34 V vs. NHE), Fe/Fe^{2+} (-0.45 V vs. NHE), and Zn/Zn^{2+} (-0.76 V vs. NHE) as shown in Figure 2-10. Therefore GO is spontaneously reduced to rGO when copper electrodes are immersed in GO solution. This spontaneous reduction is only valid when no voltage is applied. Kolbe reaction can be occurred at anode electrode during IMA process, which eliminates carboxyl groups and releases CO_2. However, the degree of reduction (27% increase of C/O ratio) is too small to induce the gelation of GO. To clarify this point, MGCN was immersed in 2 wt% EDTA solution. EDTA strongly coordinates with metal ion forming a metal-EDTA complex, which breaks the coordination between metal ions and GO [66]. Figure 2-11 shows that MGCN was completely dispersed in EDTA solution with gentle shaking, implying that cross-linking between GO in MGCN arises from the coordination between metal ions and GO not hydrophobic interaction between rGO.

Measurement of reduction potential

A platinum wire was used as the cathode to measure the reduction potential of GO sheets. Copper plate with 1 mol L^{-1} cuprous sulfate solution or Ag/AgCl electrode with 3.5 mol L^{-1} KCl solution were used as the anode. The cathode and anode compartments were connected by a salt bridge composed of agar and potassium nitrate electrolyte. The potential difference between the cathode and anode was measured by a multimeter (Keithley 2000).

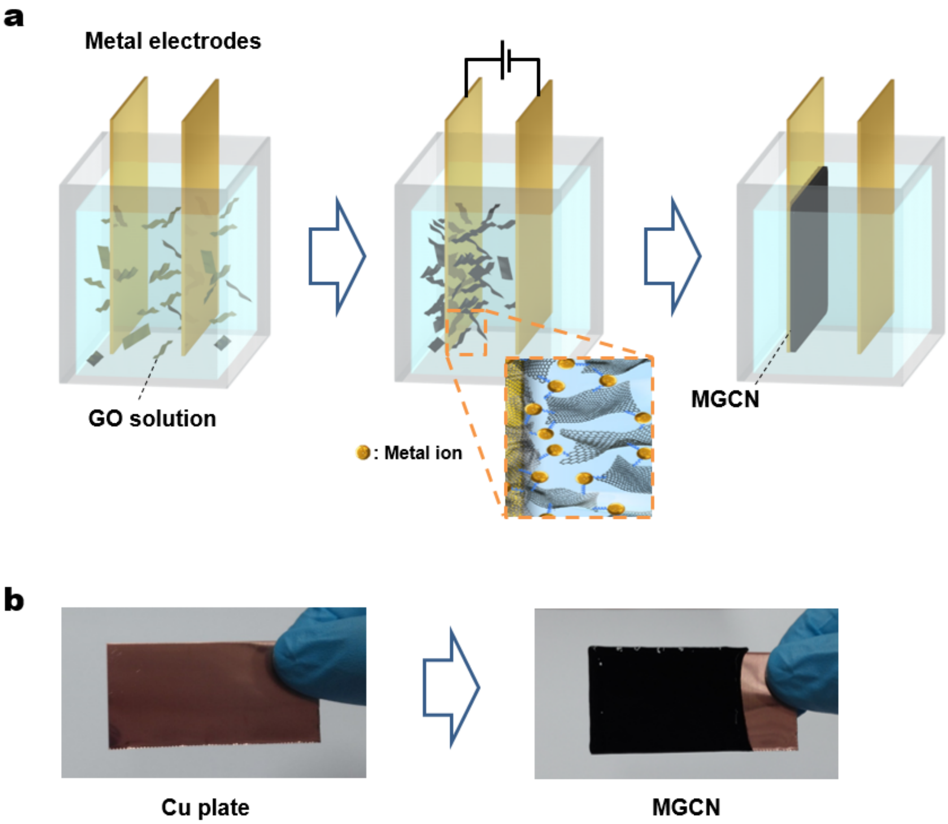

Figure 2-8. (a) Schematic of ion-mediated assembly. (b) Optical images of pristine copper plate and MGCN formed on the plate.

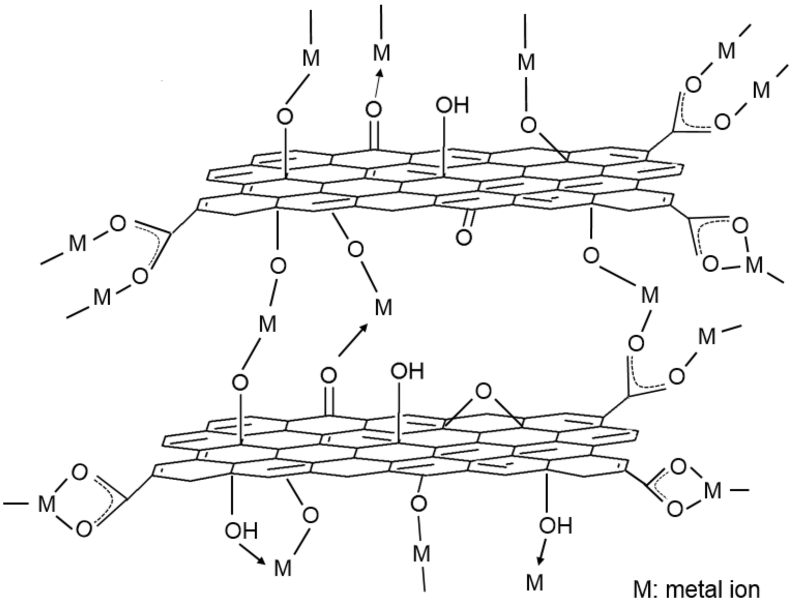

Figure 2-9. Structure model of metal-graphene oxide coordination network (MGCN).

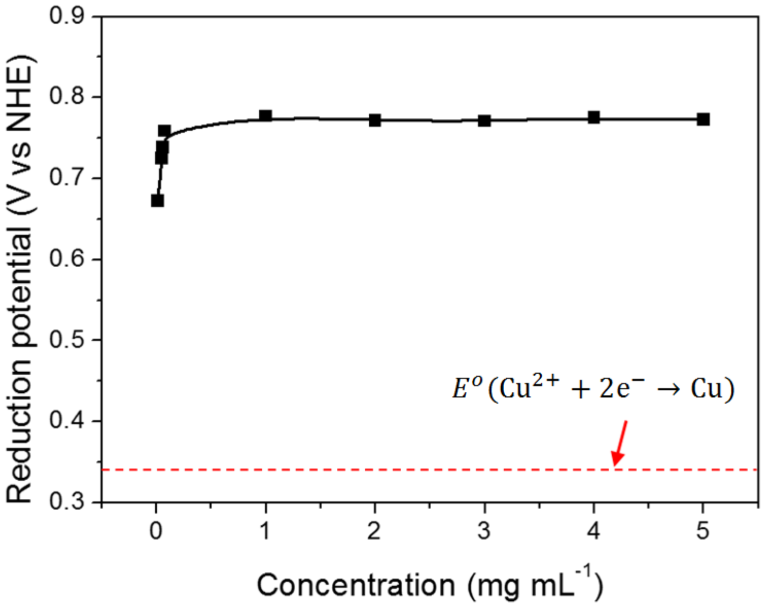

Figure 2-10. Dependence of reduction potential of GO/rGO redox reaction on GO concentration.

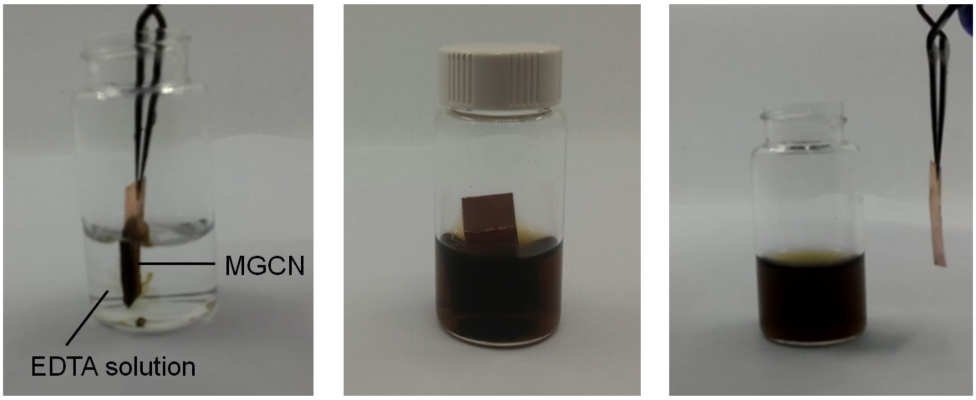

Figure 2-11. Behavior of MGCN immersed in EDTA solution.

2.2.3 Anodic dissolution

Anodic dissolution depends on metal, pH of solution, and applied voltage. Various metals, including Cu, Fe, Zn, Ni, Cr, Ti, V, Al, and stainless steel which can dissolve divalent or trivalent ions, were used as electrodes for IMA. Thick and uniform MGCNs were formed on Cu, Fe, and Zn with 2 mg mL^{-1} GO solution, applied voltage of 10 V, and process time of 1 min. However, Ni, Cr, Ti, Al, and stainless steel formed thin and irregular MGCNs due to their corrosion resistance that hindered anodic dissolution. The formation of MGCN on these metal may be attributed to the effect of electrophoretic deposition rather than IMA.

It has been known that the anodic dissolution and accompanying cathodic hydrogen gas evolution increases with decreasing pH of solution [81]. During the anodic dissolution of a divalent metal in water, the anodic and cathodic reactions are expressed by the following equations:

$$M \rightarrow M^{2+} + 2e^{-} \qquad (2\text{-}1)$$

$$2H^{+} + 2e^{-} \rightarrow H_2 \qquad (2\text{-}2)$$

Dissolution of metal ions, reaction in the anode (Equation 2-1), depends on pH of solution. Most metal can dissolve their ions in acidic solution. Pourbaix diagram for each metal can be referred to find proper pH region for dissolution. Furthermore, reaction in the cathode (Equation 2-2) in acidic solution permits the continued dissolution of metal ions into solution, leading to the continuous formation of MGCN. Therefore, acidic solution would be proper for anodic dissolution and IMA process. Figure 2-12 shows the pH of GO solution with respect to the concentration of GO. The pH decreases logarithmically with respect to the concentration, indicating the concentration of hydrogen ion is directly proportional to that of GO. The ionized oxygen groups density of GO was estimated at 3.43 mmol g^{-1} which is similar to the surface site densities of GO for metal ion absorption [82]. GO solutions with concentration above 1 mg mL^{-1} show low pH enough for metal dissolution reaction.

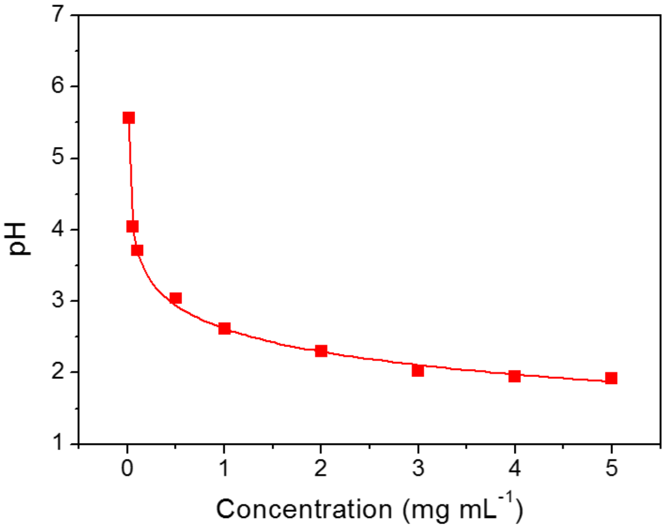

Figure 2-12. Dependence of the pH of GO solution on the concentration of GO.

2.2.4 Thickness and pore controllability

The thickness and pore size of MGCN were successfully controlled by changing process parameters including applied voltage, GO concentration, and process time.

Applied voltage

Figure 2-13(a) shows the dependence of current density on the applied voltage during IMA process with 1 mg mL^{-1} GO solution. High applied voltage induced fast dissolution of metal ions from metal. The thickness of MGCN linearly increased with increasing voltage as shown in Figure 2-13(b), implying that the number of GO sheets assembled to MGCN depends on that of dissolved metal ions. The pore size of MGCN increased with increasing voltage as shown in Figure 2-14, which is mainly attributed to the content of cross-linker (copper ion) in MGCN. As the applied voltage increased, the content decreased from 5.3 to 3.9 at% (Figure 2-27(a)). Lower content of cross-linker brought about larger pore size of MGCN.

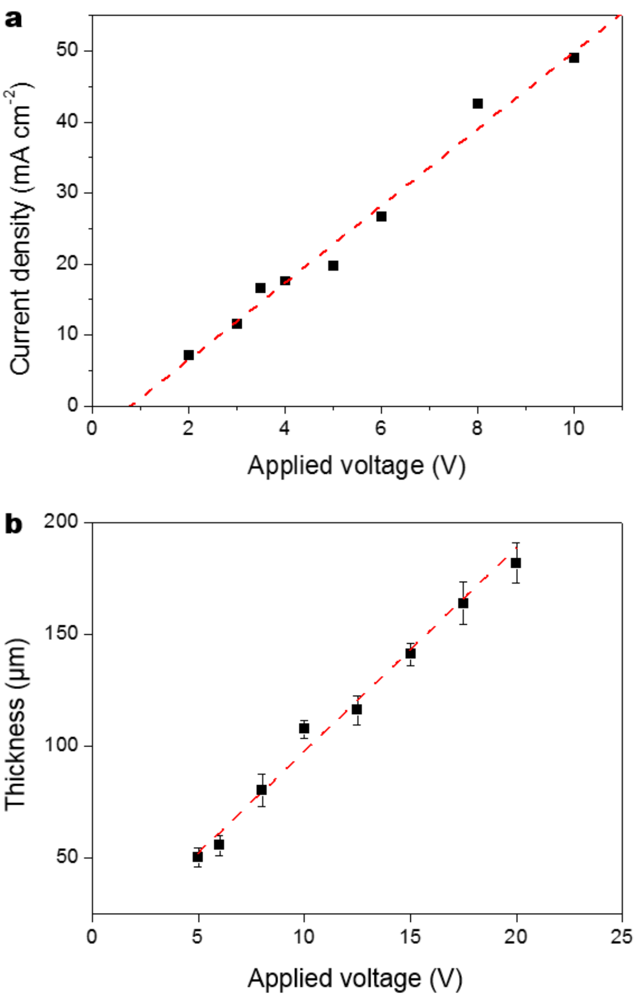

Figure 2-13. (a) Dependence of current density on applied voltage. (b) Dependence of MGCN thickness on applied voltage.

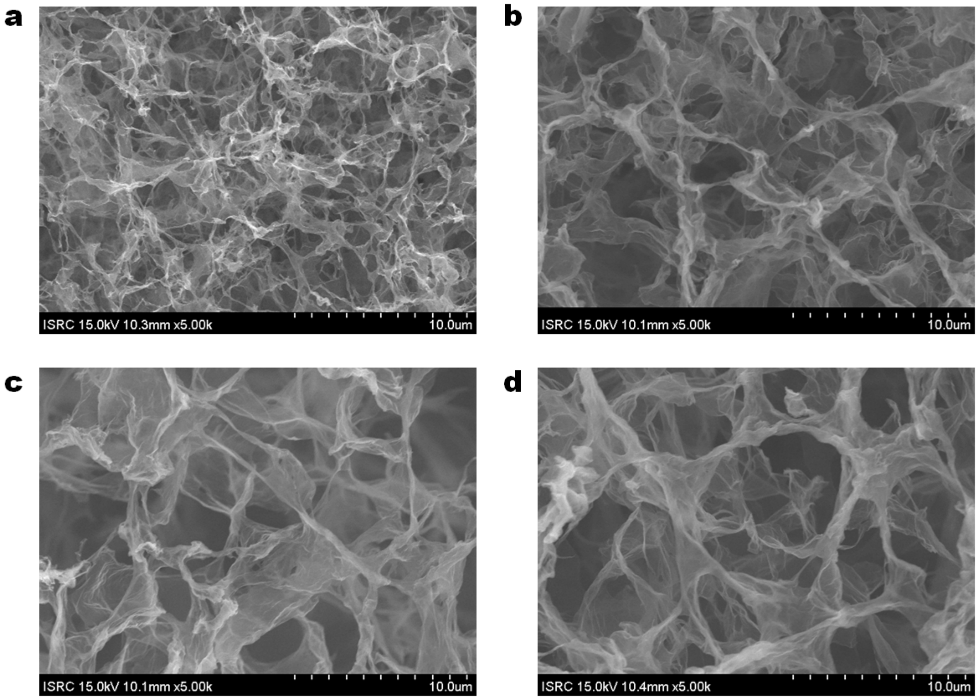

Figure 2-14. SEM images of MGCN fabricated by the applied voltage of (a) 5 V, (b) 10 V, (c) 15 V, and (d) 20 V. GO concentration is 1 mg mL^{-1} and process time is 10 sec for all samples.

GO concentration

High concentration of GO solution also increased the thickness of MGCN for the same voltage and process time (Figure 2-15(a)) with increased current density (Figure 2-15(b)). Current density increases with increasing ionic conductivity and hydrogen ion concentration of GO solution, decreasing metal ion concentration. Ionic conductivity of GO solution is proportional to GO concentration as shown in Figure 2-15(c). Moreover, oxygen functional groups on GO sheets release hydrogen ions into the solution (Figure 2-15(d)). In IMA process, GO sheets absorb metal ions, thereby maintaining low concentration of metal ions in the solution. Therefore, the thickness of MGCN increased as GO concentration increases. The pore size of MGCN increased with increasing GO concentration as shown in Figure 2-16. Dependence of the pore size on GO concentration is also attributed to the content of cross-linker (copper ion) in MGCN in the same manner as that on applied voltage. As the concentration increased, the content decreased from 5.3 to 3.7 at% (Figure 2-27(b)) resulting in large pore of MGCN.

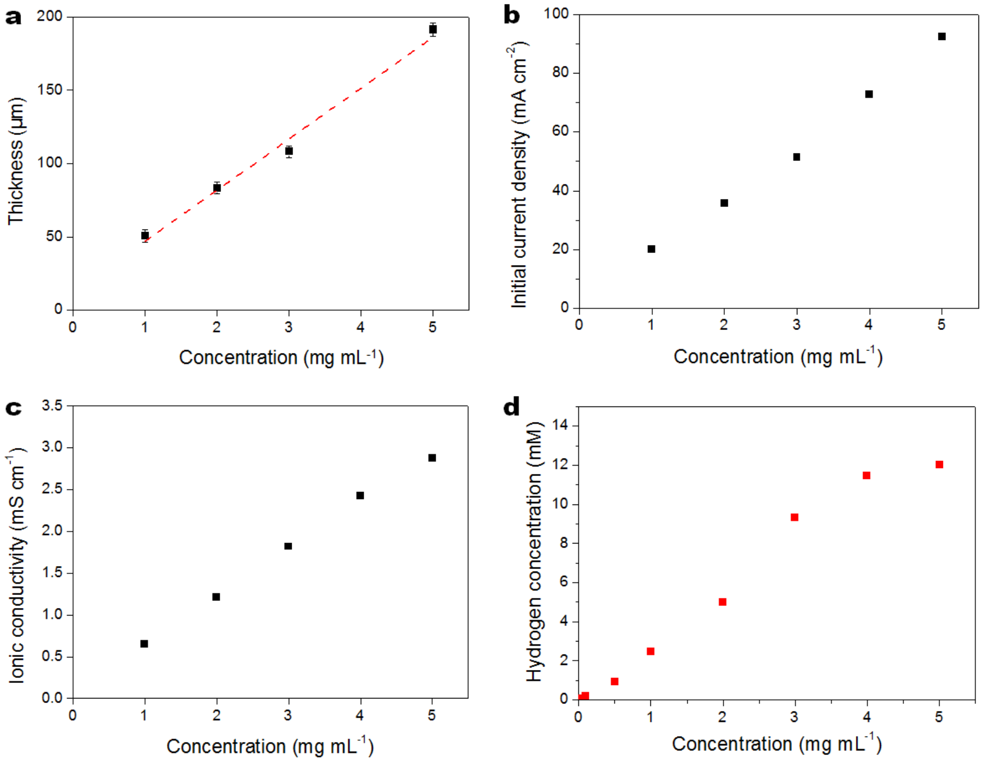

Figure 2-15. (a) Dependence of MGCN thickness on GO concentration. (b) Dependence of initial current density on GO concentration. (c) Dependence of ionic conductivity on GO concentration. (d) Dependence of hydrogen ion concentration on GO concentration.

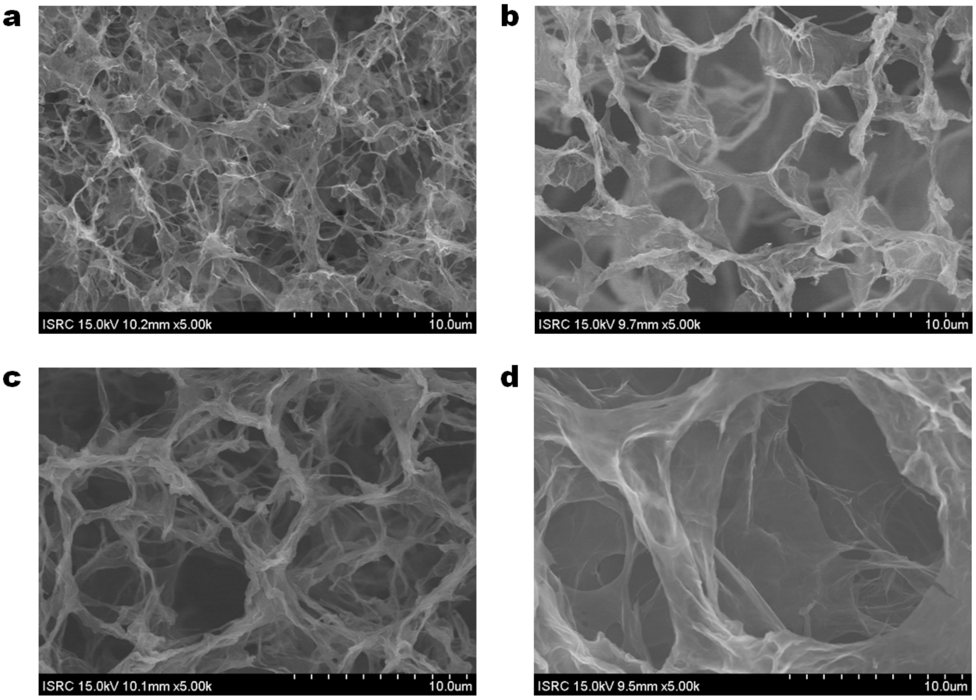

Figure 2-16. SEM images of MGCN fabricated by GO solutions of which concentrations are (a) 1 mg mL^{-1}, (b) 2 mg mL^{-1}, (c) 3 mg mL^{-1}, and (d) 5 mg mL^{-1}. Applied voltage is 5 V and process time is 10 sec for all samples.

Process time

MGCN showed non-linear thickness increase with time as shown in Figure 2-17(a), which is attributed to the decrease of GO concentration during IMA process. Current density also showed a non-linear behavior as shown in Figure 2-17(b), which is closely related to the change of ionic conductivity and hydrogen ion concentration of GO solution. Figure 2-17(c) and (d) show ionic conductivities and hydrogen concentrations of GO solutions after IMA process with different time. Both of them decreased with process time, which brought about non-linear current decrease and corresponding thickness increase. Another reason for the non-linear thickness increase is prolonged path of metal ions. As MGCN becomes thicker, metal ions have to move longer path, which decreases their dissolution rate. Figure 2-18 shows the dependence of the pore size of MGCN on process time. The pore size showed negligible change with process time, arising from small change of the content of cross-linker (from 5.3 to 4.7 at%, Figure 2-27(c)).

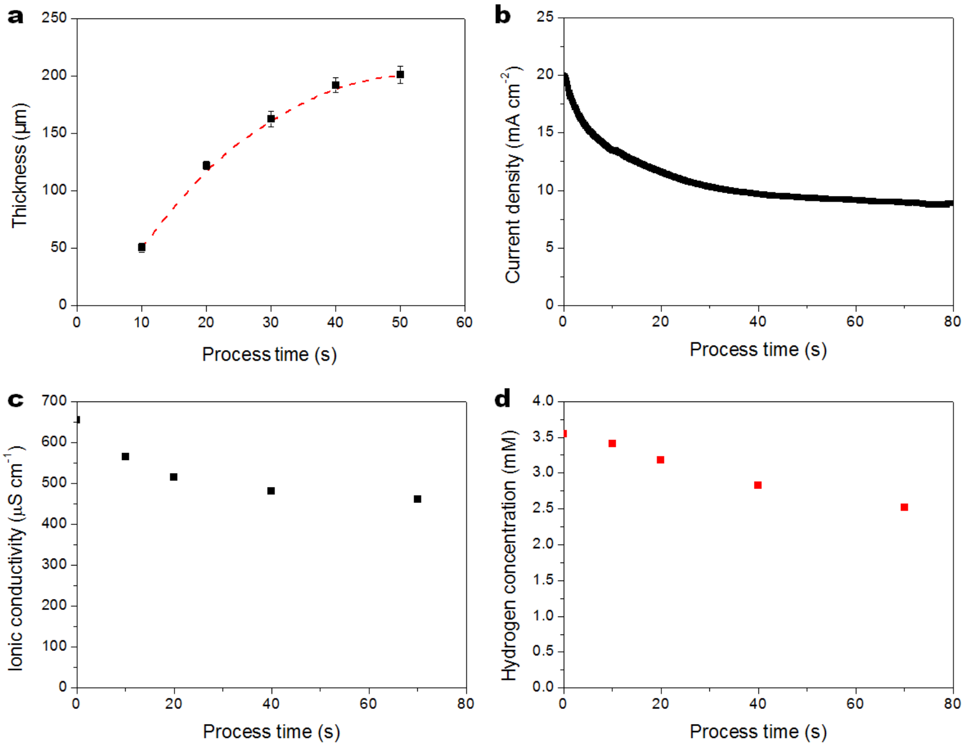

Figure 2-17. (a) Dependence of MGCN thickness on process time. (b) Dependence of current density on process time. (c) Dependence of ionic conductivity on process time. (d) Dependence of hydrogen ion concentration on process time.

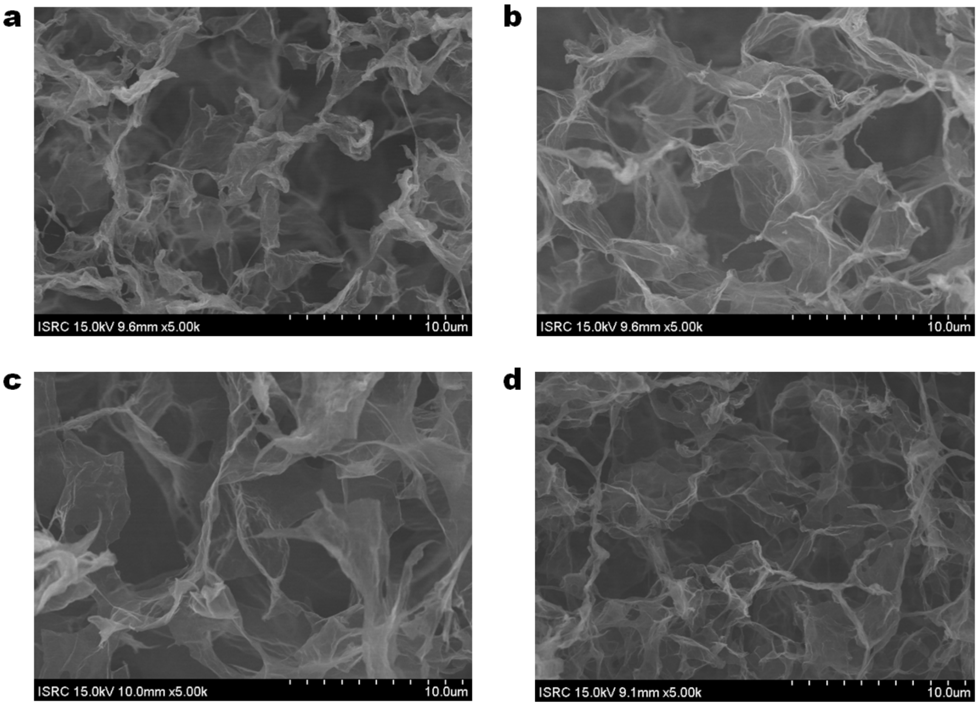

Figure 2-18. SEM images of MGCN fabricated for different process time. (a) 20 sec, (b) 30 sec, (c) 40 sec, and (d) 50 sec. Applied voltage is 5 V and GO concentration is 1 mg mL^{-1} for all samples.

2.2.5 Functional guests decorated MGCN

Functional guests, including metal, metal oxide, and ceramic particles, can give MGCN new functionality for energy storage, sensor, and energy harvesting [83]. MnO_2, SnO_2, and TiO_2 nanoparticles were decorated on MGCN by simply dispersing them in GO solution in advance of IMA process. MnO_2, SnO_2, and TiO_2 were dispersed in 1 mg mL^{-1} GO solution with concentrations of 1, 0.2, and 0.1 mg mL^{-1}, respectively.

As shown in Figure 2-19, a large number of nanoparticles were attached on basal plane of GO sheets. Interestingly, considerable nanoparticles were sandwiched between GO sheets. Nanoparticles wrapped by GO sheets can possess excellent cycle performance for capacitor and Li-battery as GO sheets prevents loss of nanoparticles during charging/discharging processes [84-86].

Meanwhile, MGCN has abundant metal ions between GO sheets. These ions also can be used as sources of nanoparticles. Thermal annealing of MGCN at 800-1000 ^{o}C in H_2 and Ar atmosphere induced thermal aggregation and reduction of metal ions to form metal nanoparticles. Figure 2-20 shows copper nanoparticles uniformly formed on basal plane of GO sheets. The diameters of copper nanoparticles are in the range of several tens to hundreds of nanometers.

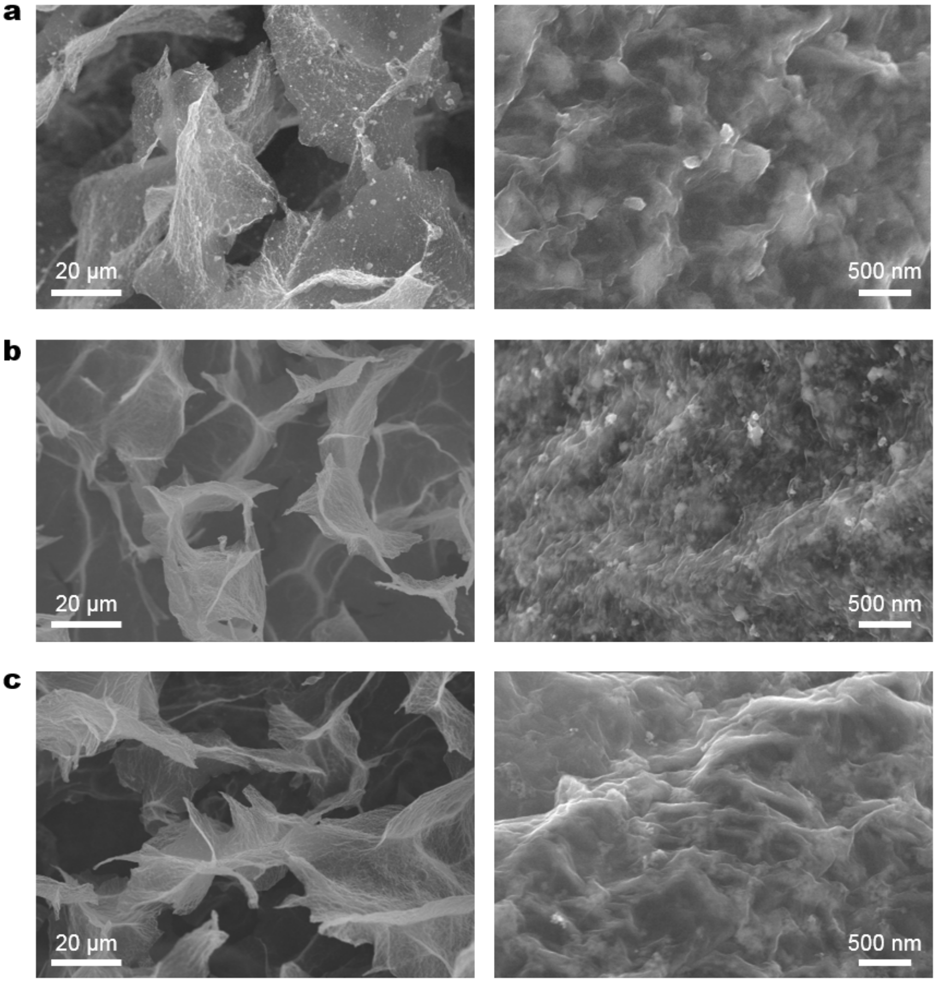

Figure 2-19. SEM images of (a) MnO_2, (b) SnO_2, and (c) TiO_2 decorated MGCN.

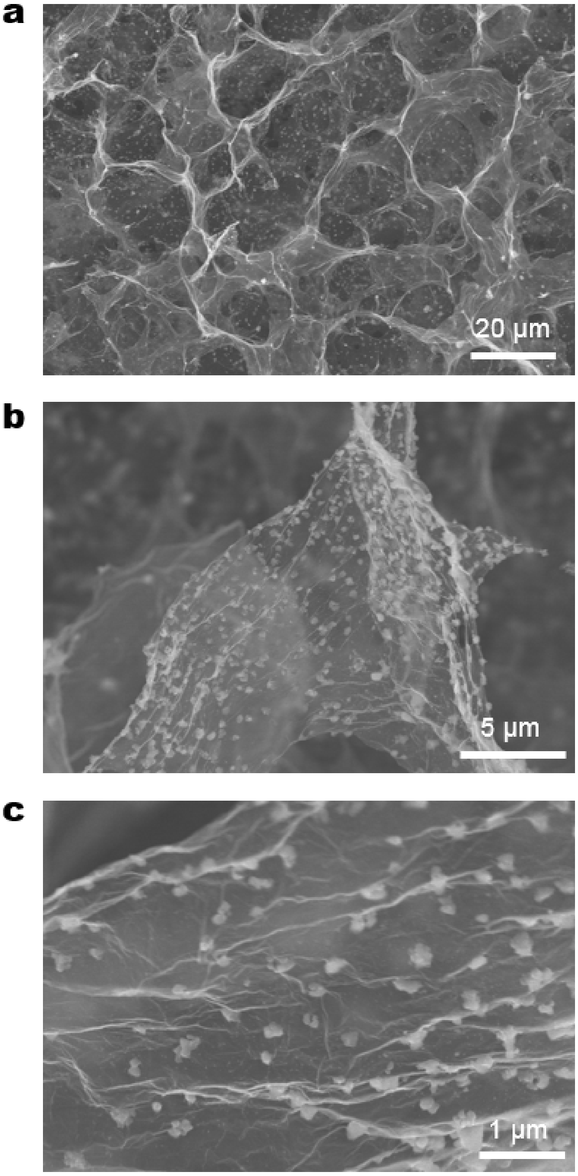

Figure 2-20. SEM images of Cu nanoparticles decorated MGCN.

2.3 Basic properties of MGCN

2.3.1 Morphology

MGCN can be formed on plate, mesh, rod, and wire as shown in Figure 2-21. Shape and dimension of MGCN also can be easily controlled because MGCN continuously grows with the same configuration of metal substrate. Optical images in Figure 2-22(a) show various shapes of MGCN including triangle, circle, and heart shape. The insets of the figure are the shape of metal substrate. MGCNs in the figure are aerogels that were dried under vacuum to maintain porous structure. The aerogels retained its macroscopic shape without any collapse and crack during drying process. Figure 2-22(b) shows large area MGCN with the thickness of 7 mm. This MGCN was fabricated on 25 μm thick copper foil that was simply peeled off after drying.

The interior microstructure of MGCN aerogel was investigated by scanning electron microscope (SEM). The aerogel has well interconnected 3-D porous network as shown in cross-sectional SEM images (Figure 2-23). Pore walls in the network are continuously cross-linked by the partial overlapping and coalescing of GO sheets. The pore sizes are in the range of several micrometers to tens of micrometers.

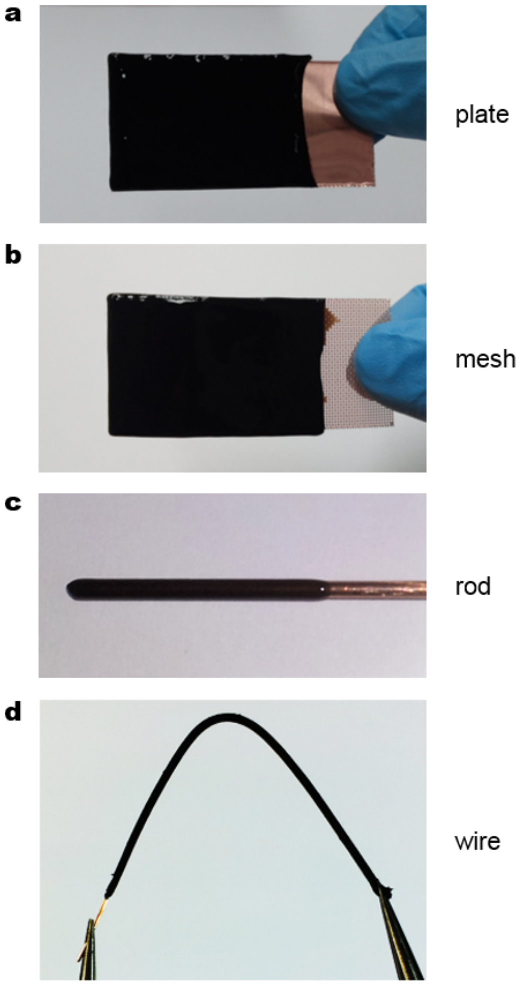

Figure 2-21. Optical images of MGCNs formed on copper (a) plate, (b) mesh, (c) 3 mm diameter rod, and (d) 300 μm diameter wire.

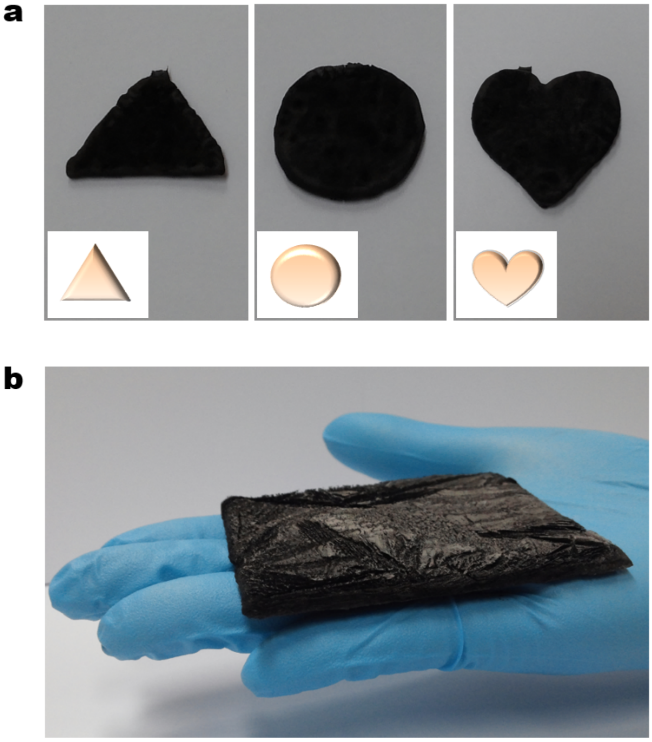

Figure 2-22. Optical images of (a) MGCNs formed on triangle, circle, and heart-shaped metal foils that were peeled off after IMA process. (b) Optical image of a large area MGCN.

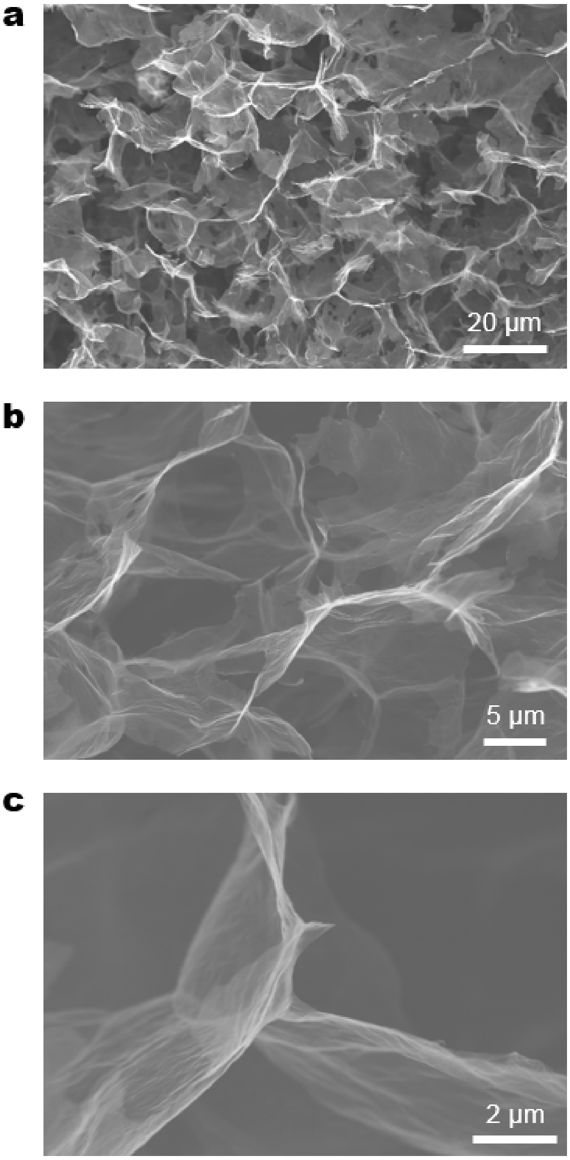

Figure 2-23. SEM images of MGCN aerogel. The aerogel was fabricated by IMA method with an applied voltage of 10 V for 10 sec, followed by vacuum drying process.

2.3.2 Chemical structure

XPS and FT-IR analysis were performed to investigate the chemical structure of MGCN. For comparison, GO film was fabricated by filtering GO solution using a polytetrafluoroethylene (PTFE) membrane filter (47 mm diameter, 0.2 μm pore size, Whatman).

In the core-level C1s XPS spectrum of GO (Figure 2-24(a)), sp^2 C=C bond at 284.6 eV and epoxy C-O bond at 286.5 eV are predominant with other oxygen containing groups (hydroxyl C-O bond at 285.6 eV, carbonyl C=O bond at 287.9 eV, and carboxyl O=C-O bond at 289.0 eV) [71-73]. Peaks of oxygen functional groups of GO, especially C-O bond in epoxy and C=O bond in carbonyl/carboxyl groups, were decreased after IMA process with copper substrate as shown in Figure 2-24(b). Hydroxyl C-O bond was rather increased after IMA process, which may arise from the opening of epoxide by metal ions. XPS spectrum of MGCN formed on iron and zinc substrate also reveals that C-O and C=O bonds were considerably removed. This phenomenon is presumably attributed to the coordination between oxygen functional groups and metal ions [71].

The results of FT-IR analysis were in good agreement with those of XPS. GO film showed aromatic C=C (1610 cm^{-1}), epoxy C-O (1230 cm^{-1}), alkoxy C-O (1050 cm^{-1}), and carboxyl C=O (1730 cm^{-1}) as shown in Figure 2-25(a) [74]. In the spectrum of MGCN formed on copper (Figure 2-25(b)), the intensities of epoxy C-O and carboxyl C=O peaks were significantly decreased by coordination with metal ions. It was also observed that carboxyl C-O peak increased and wavenumber difference between carboxyl C-O peak and carboxyl C=O peak was decreased, implying that the bonds between carboxyl groups and metal ions are bidentate and bridging coordination [77, 78]. On the other hand, FT-IR spectrum of MGCN formed on Ni (Figure 2-25(c)) was similar to that of GO, indicating that GO sheets were attached to Ni substrate by electrophoretic deposition rather than IMA.

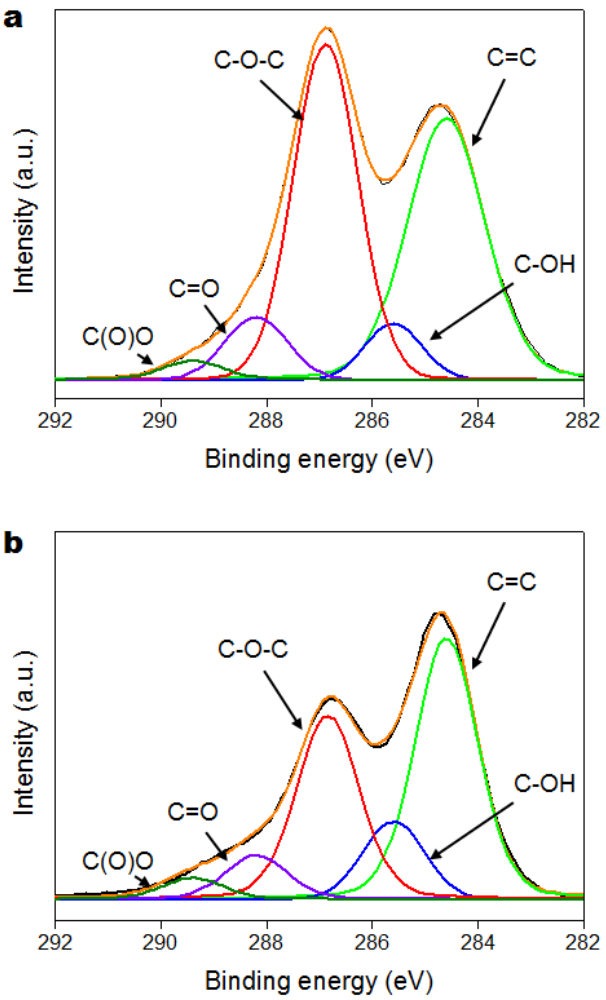

Figure 2-24. XPS spectra of C1s for (a) GO film and (b) MGCN formed on copper substrate.

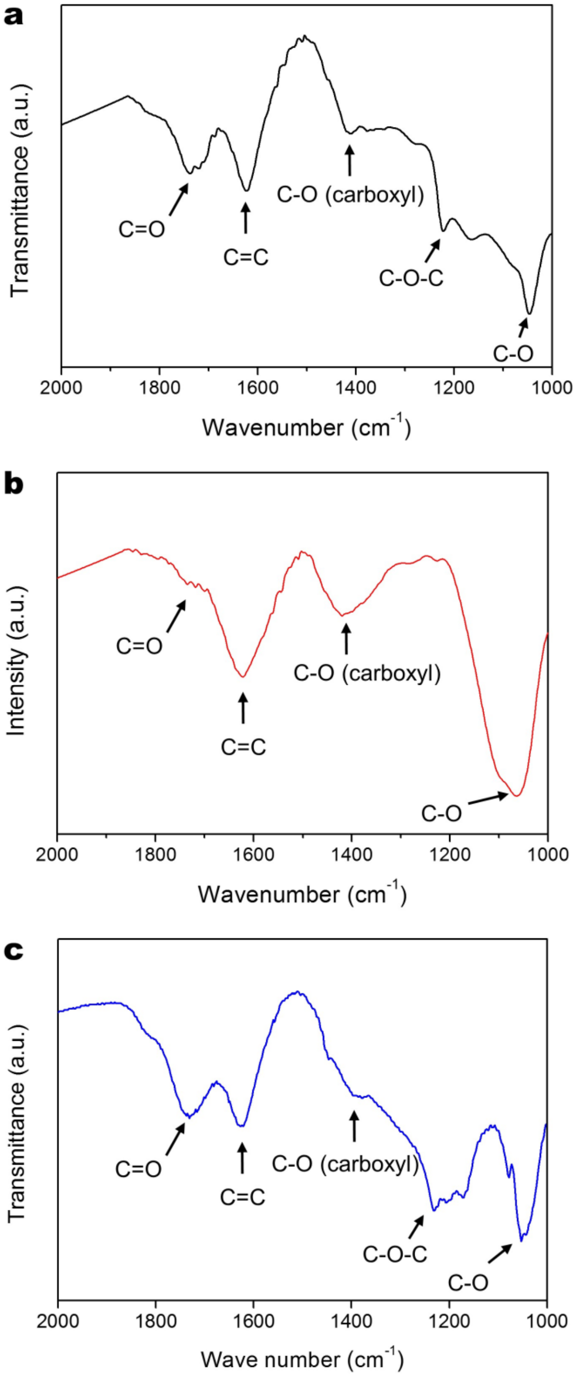

Figure 2-25. FT-IR spectra of (a) GO film, (b) MGCN formed on copper substrate, and (c) MGCN formed on Ni substrate.

Figure 2-26(a) shows XPS spectra of Cu 2p, O1s, and C1s for MGCN and GO film. The spectrum of MGCN has Cu 2p peaks which are absent in that of GO film. Figure 2-26(b), XPS spectrum of Cu 2p for MGCN, shows Cu $2p_{3/2}$ (932.5 and 934 eV), Cu $2p_{1/2}$ (952.3 and 954.2 eV) peaks assigned to Cu^{1+} and Cu^{2+} species, respectively. Shake-up satellite peaks at ~943 eV and ~962 eV are also found in the spectrum as an indication of the presence of Cu^{2+} species [87, 88].

The content of copper in MGCN and carbon to oxygen ratio of MGCN were measured by a SEM equipped with energy dispersive spectrometer (EDS) system. The atomic concentration of copper ranged from 3.7 to 5.3% depending on process parameters such as applied voltage, GO concentration, and process time as shown in Figure 2-27. The concentration of copper was nearly constant along the thickness direction of MGCN, meaning that copper ions moved in MGCN hydrogel to mitigate concentration gradient. Carbon-to-oxygen ratio of MGCN showed negligible dependence on the process parameters (Figure 2-28).

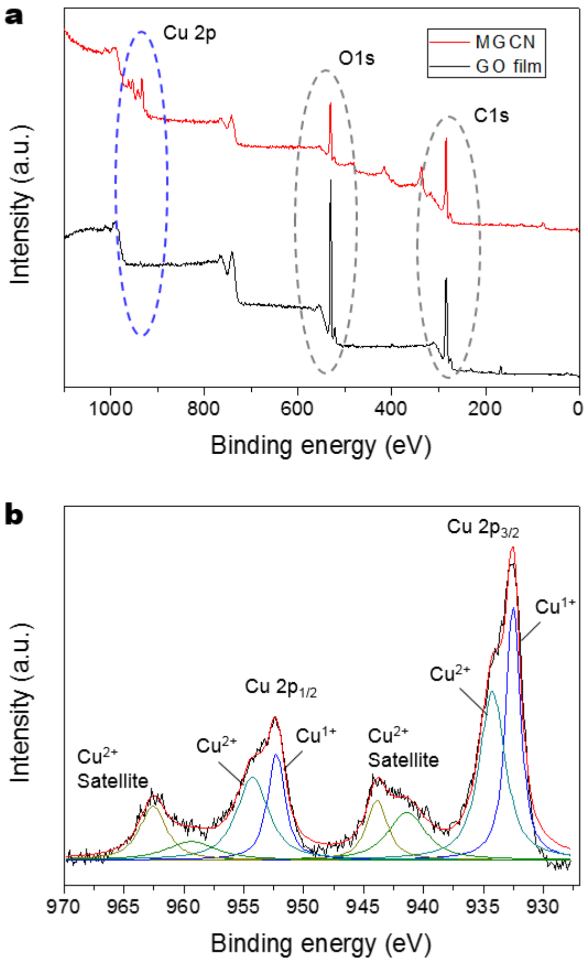

Figure 2-26. XPS spectra of (a) MGCN and GO film with a scanning range from 0 to 1100 eV. (b) XPS spectrum of Cu 2p for MGCN.

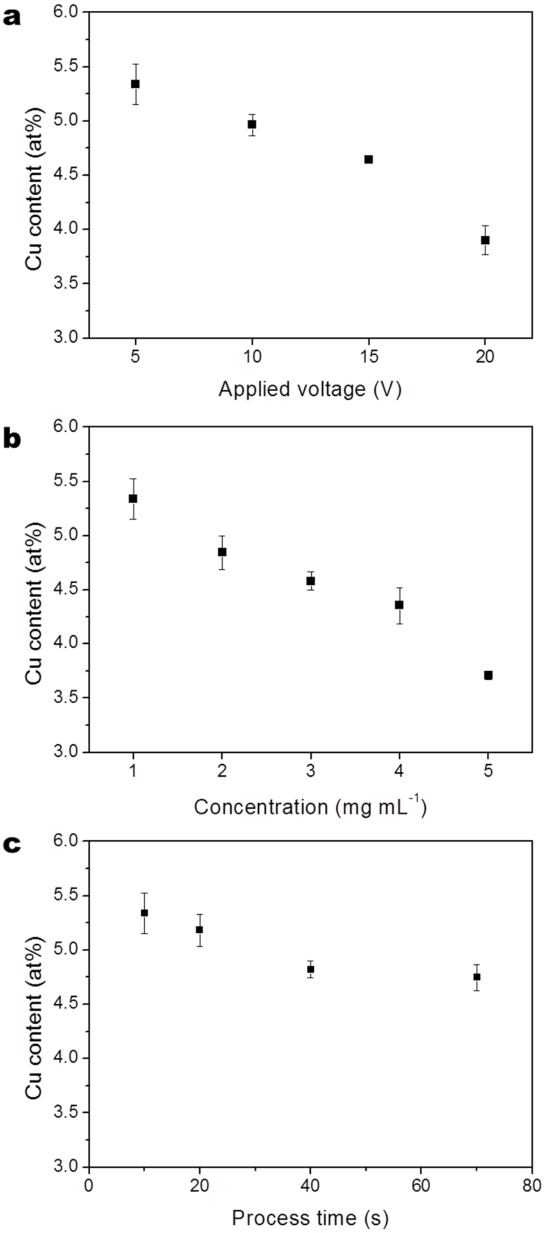

Figure 2-27. The dependence of copper concentration in MGCN on (a) applied voltage, (b) GO concentration, and (c) process time.

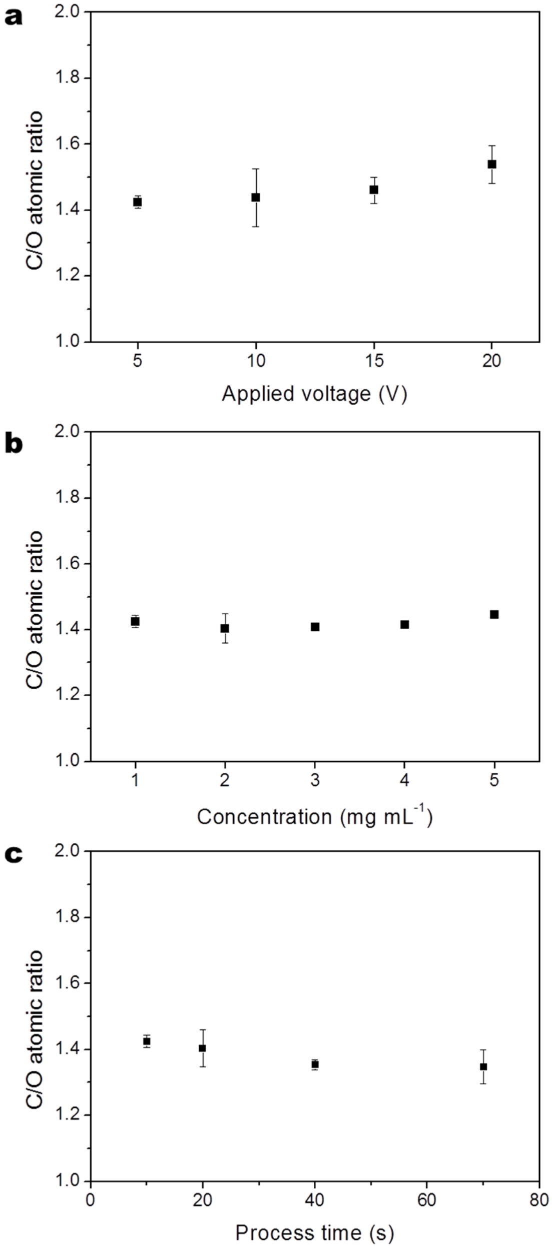

Figure 2-28. Dependence of carbon-to-oxygen (C/O) ratio of MGCN on (a) applied voltage, (b) GO concentration, and (c) process time. C/O ratio of GO was ~1.1.

2.3.3 Physical properties

The density of MGCN aerogel was estimated to be 12.3±0.8 mg cm^{-3}, which is comparable to that of carbon fiber aerogel and graphene sponge [13, 89].

The porosity and pore diameter of MGCN annealed at 200 °C were measured using a mercury porosimetry (AutoPore IV 9500) as shown in Figure 2-29. Porosity was estimated to be 90.8% implying that considerable space of MGCN remained empty. Average pore diameter was 12.1 μm which is consistent with that measured from SEM images.

The surface area of MGCN was measured using methylene blue adsorption [90] . It has been well known that each methylene blue molecule adsorbed on graphitic materials represents 1.35 nm^2 of surface area [6]. After immersing a known mass of MGCN in methylene blue aqueous solution, the solution was stirred at a rate of 500 rpm for a day to reach maximum adsorption of methylene blue molecules. The solution was centrifuged to completely settle MGCN, thereby leaving unadsorbed methylene blue molecules in supernatant. The methylene blue concentration was determined through UV-vis spectroscopy analysis as shown in Figure 2-30. Star mark indicates the concentration of methylene blue in supernatant. Considering initial methylene blue concentration, the mass of MGCN and initial solution, the surface area for MGCN was calculated to be 144.5 m^2 g^{-1}. Surface area measured by the mercury porosimetry was 7.8 m^2 g^{-1} much lower compared to methylene blue adsorption method, which may be attributed to overlapped rGO sheets.

Electrical conductivity of MGCN is too high to be measured using an ordinary ohmmeter, meaning that MGCN is electrical insulating material. The conductivity of MGCN annealed at 1000 °C in H_2 and Ar atmosphere was 3.87 S cm^{-1}.

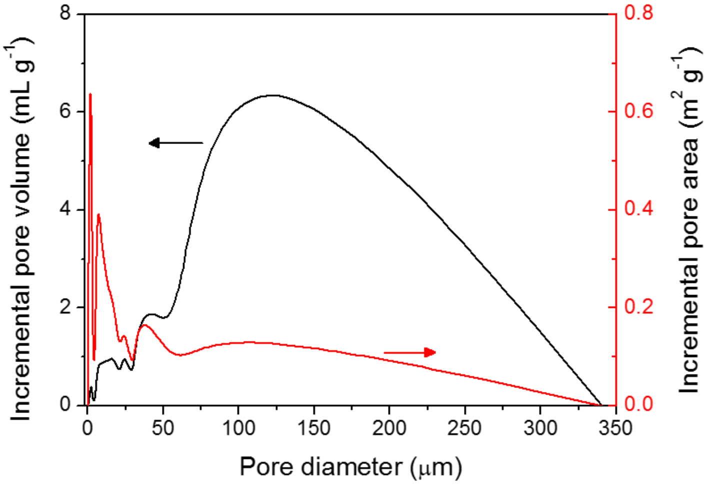

Figure 2-29. Dependence of pore volume and pore area of MGCN on pore diameter.

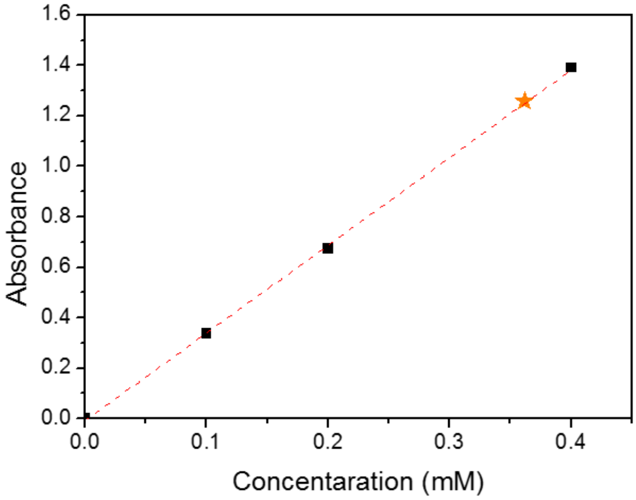

Figure 2-30. Dependence of absorbance of methylene blue solution on its concentration.

Chapter 3. Selective capillarity

In this chapter, the selective capillarity of MGCN is investigated and utilized to suction and store liquid body of spilled oil. The graphene vessel devised here using MGCN can bring about an important yet basic change in the strategy for spilled oil collection. When it is placed on the oil-covered seawater, the graphene vessel selectively separates the oil, then collects and stores the collected oil in the vessel all by itself without any external power inputs.

3.1 The strategy for removal of oil spill

3.1.1 Conventional oil collection strategy

Oil spills have caused sea and river pollution resulting in severe environmental and ecological problems [91-93]. The Gulf of Mexico oil spill (deepwater horizon drilling rig explosion) in 2010 and Exxon Valdes oil spill (grounding of oil tanker) in 1989 spilled 4,900,000 and 750,000 barrels of crude oil, respectively. Since 1963, approximately 28,000,000 barrels of oil were spilled by accidents and the possibility of large oil spill accidents has increased with industrial development and deepwater oil drilling.

It is striking in this light that the oil collection strategy used for recent Gulf of Mexico spill was much the same as for Santa Barbara's 1969 oil spill, despite remarkable advances made in science and technology since 1969. Containment boom was used to block oil spreading, and skimmer was used to collect the oil gathered in the boom (Figure 3-1(a), (b)) [94, 95]. Workers mopped up oil on the beach using sorbents. The best way to cope with oil spill is to collect entire oil on the sea surface before the oil reaches a shore. The current approach suffers from oil spreading on water. Concentrating oil in the boom is in direct opposition to the natural tendency of the oil to spread, therefore, oil easily disperses by wind, waves, and currents (Figure 3-2). The thin layer of oil on water hinders effective collection of spilled oil with traditional macro-scale skimmer. Containment and collection at sea result in removal of a relatively small proportion of a large oil spill, at best only 10-15% [96].

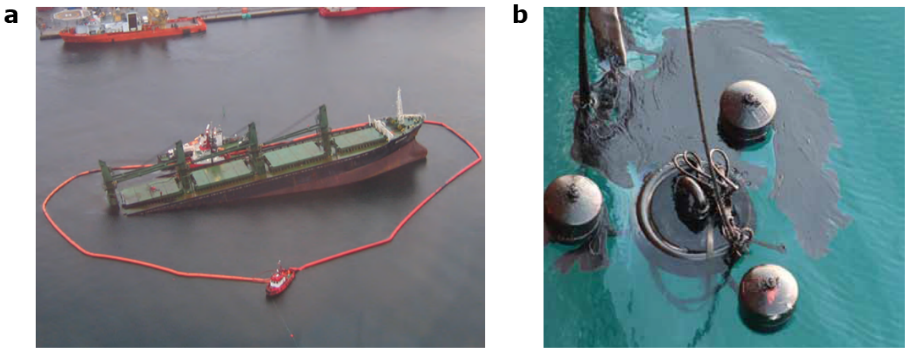

Figure 3-1. Photographs of (a) oil containment boom and (b) weir skimmer [94, 95].

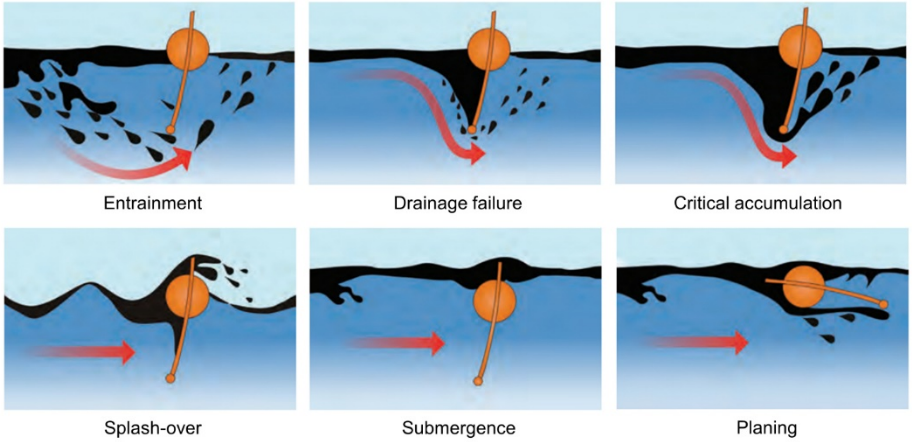

Figure 3-2. Containment boom failure modes. The arrows indicate current direction [94].

3.1.2 Recent research on oil removal

There have been a large number of studies on oil removal, either for oil absorption or oil/water separation. For oil absorption, nanomaterial sponges have extensively been used due to their low density and superhydrophobicity (Figure 3-3). Reduced graphene oxide [13-15, 97-99], carbon nanotube (CNT) [100-102], carbon fiber [89], and polymer [103, 104] were mainly utilized as a raw material for sponge fabrication, showing outstanding oil absorption capacity, efficiency, and reusability. For oil/water separation, superhydrophobic or superhydrophilic membrane and mesh, made by CNT [105-107], polymer [108-110], metal hydroxide [111], or silicate [112, 113], were used to selectively pass oil or water for oil/water separation (Figure 3-4). In particular, membrane type [105, 106, 108, 109] was efficient for separating emulsion of oil and water due to its small pore size while mesh type [110-113] yielded high flux with large pores. An oxidized copper mesh box was recently proposed for in-situ separation and collection of spilled oil [114], and subsequently the mesh box was coated with palmitic acid to improve the performance [115].

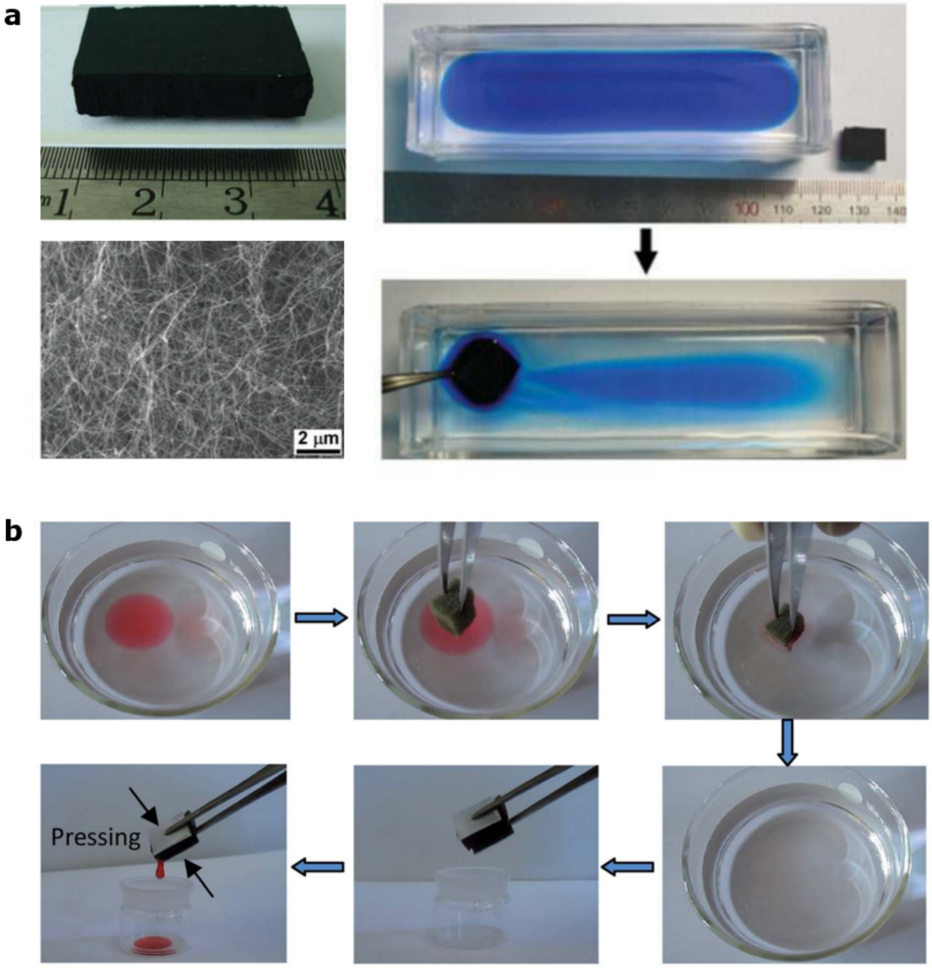

Figure 3-3. Oil absorption by using (a) CNT sponge [101] and (b) polyurethane sponge [104]. Both sponges can be reused after squeezing them to remove oil inside.

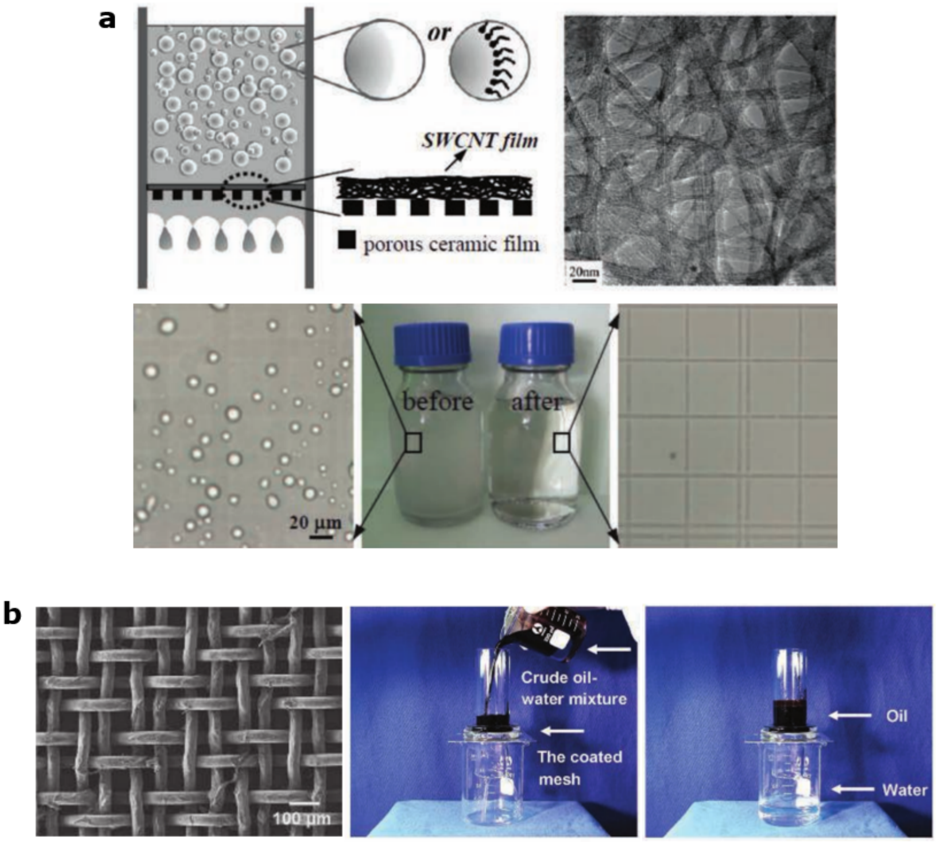

Figure 3-4. (a) Separation of water-in-oil emulsion where oil selectively permeates through CNT film [105]. Optical microscopy images of water-in-oil emulsion before and after filtration. (b) Oil/water separation by using hydrophilic and underwater oleophobic polyacrylamide hydrogel-coated mesh [110].

3.1.3 Oil collection by a graphene vessel having selective capillarity

For any scheme to be useful for collecting spilled oil on seawater, a number of conditions have to be met. A floating device, when put into the seawater for the collection, has to be sturdy enough to withstand sloshing seawater and be effective even when it is tumbled over. The material used has to be chemically stable since crude oil contains organic solvents such as toluene and other hydrocarbons, which may dissolve the material. To selectively separate the oil and keep the collected oil in the device from remixing with surrounding seawater, the device walls must withstand the seawater pressure when it is submerged by the weight of collected oil and splashed by sloshing seawater.

In this chapter, an autonomous graphene vessel that satisfies the conditions is presented. The vessel separates spilled oil from seawater, collects, and stores the collected oil in the vessel without any external power inputs. To construct the vessel, IMA process followed by annealing is utilized to deposit rGO from a solution of GO nanoplatelets on copper mesh. This graphene vessel is essentially an enclosed empty container, the hull of which is made of copper mesh that is, in turn, coated with MGCN foam covering the whole surface, inside and out. Countless pores in MGCN foam quickly suction spilled oil by capillary force like sponge, and the suctioned oil flows into the vessel by gravity while the pores repel water, showing selective capillarity.

3.2 Fabrication of graphene vessel

3.2.1 MGCN formed on copper mesh

To construct the graphene vessel, IMA process was utilized because there was no suitable process available by which the copper mesh can be coated thick, to mm range, and uniformly all over the vessel with graphene. For the purpose, a container made of copper mesh was immersed into a tank filled with a deionized water solution of well-dispersed GO (Figure 3-5). A constant dc voltage was applied between the anode of copper mesh container and a copper plate placed in the solution acting as the cathode, which makes cupric ions dissolve from the anode. Furthermore, the GO platelets were attracted to the anode by electrostatic force. They were connected by cupric ions at the anode of copper mesh container, forming a MGCN hydrogel [71]. This simple procedure is all it takes to construct a GO vessel. Only a larger copper mesh plate is needed for a larger graphene vessel, making the scaling-up rather simple.

Detail experimental conditions

A copper mesh (Nilaco Corp., CU-118050) with 300 μm openings was utilized to form the MGCN hydrogel by IMA. The mesh was cut and folded to make a mesh container. This copper mesh container was immersed into a tank filled with a deionized water solution of well-dispersed GO. The homogeneous colloidal solution was obtained by preparing GO powders via a modified Hummers method

[116] and dispersing them in deionized water with sonication. A constant dc voltage of 10 V was applied between the anode of copper mesh container and the cathode of copper plate for 1 min by a DC power supply (ITECH, IT6720). The MGCN hydrogel formed on the mesh was immediately dried using a vacuum freeze dryer (Ilshin, FDS-5508) or a vacuum furnace (custom made furnace). This MGCN aerogel was annealed in vacuum (under 10^{-2} Torr, vacuum furnace) at 200 ^{o}C for several hours to eliminate remaining water molecules and oxygen functional groups.

Preparation of graphene oxide

GO was prepared with the same method mentioned in section 2.2.1. GO sheet was re-dispersed in deionized water with a controlled concentration of 1-5 mg mL^{-1} by sonication.

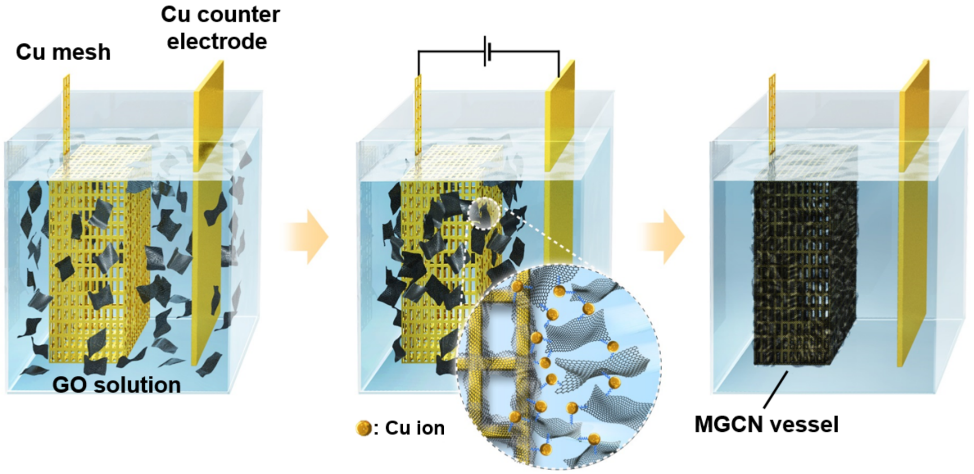

Figure 3-5. Schematic of ion mediated assembly (IMA) process for fabricating graphene vessel. Copper mesh container (vessel) and counter electrode are immersed in GO solution. When a dc voltage is applied between the electrodes, GO nanoplatelets are attracted to anode and an ion-mediated assembly takes place.

3.2.2 Morphology of MGCN on copper mesh

The GO (MGCN) hydrogel was dried by freeze-drying or vacuum drying to maintain its porous structure. This aerogel was annealed in vacuum at 200 ^{o}C to reduce the GO aerogel to the rGO aerogel (Figure 3-6). The aerogel (foam) formed at the copper mesh edge was magnified to examine the interface between the copper mesh and the aerogel by SEM (Figure 3-7(a)). No cracks or fractures could be observed (Figure 3-7(b)). The aerogel has a well interconnected 3-D porous network as revealed in the cross-sectional SEM image of Figure 3-7(c). The pore size is in the range of several micrometers to tens of micrometers.

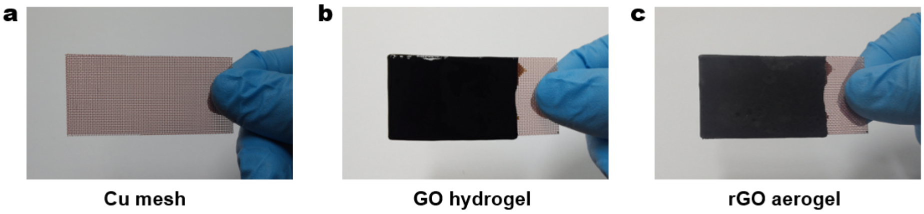

Figure 3-6. Optical images of (a) copper mesh, (b) copper mesh coated with GO hydrogel, and (c) copper mesh coated with rGO aerogel. The GO (MGCN) hydrogel was formed by the IMA process. The hydrogel was dried in vacuum to turn it into an aerogel and then annealed at 200 °C to convert it to rGO aerogel. The mesh was observed to be well coated with the aerogel without macroscopic holes.

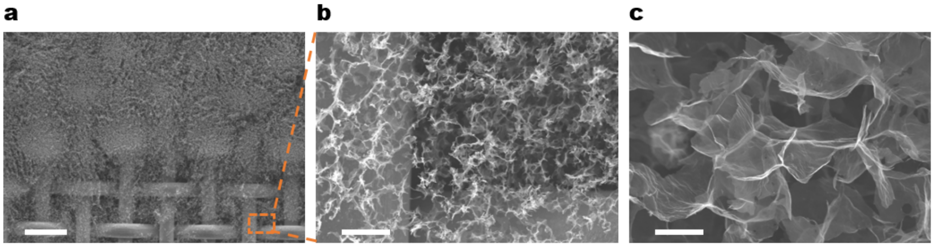

Figure 3-7. SEM images of MGCN aerogel (foam): (a) Image of MGCN foam at the edge of copper mesh. The foam formed uniformly on the mesh without macroscopic holes. Scale bar is 500 μm. (b) Magnified SEM image of the rectangular part in the image of (a). (c) Cross-sectional SEM image of the foam. The rGO nanoplatelets are interconnected to form a three-dimensional porous structure with pores in the range of several micrometers to tens of micrometers. Scale bars are 50 μm and 10 μm, respectively, in (b) and (c).

3.3 Oil collection demonstration

3.3.1 Autonomous oil collection

The scheme of oil collection by the graphene vessel is illustrated in Figure 3-8(a). The graphene vessel is an enclosed empty container, the hull of which is made of copper mesh that is, in turn, coated with MGCN foam covering the whole surface, inside and out. When the vessel is put into the seawater covered with a thin layer of spilled oil, the oil is selectively suctioned into the MGCN foam by capillary force at the interface between the thin layer of oil and the foam, suctioning oil but repelling water at the interface because of the hydrophobicity and superoleophilicity [117, 118] of the foam (refer to section 3.4.1 and Figure 3-12). As the foam gets soaked with the collected oil, gravity forces the oil to flow into and fill the vessel, enabling continuous oil collection even without an external power. Because of hydrophobicity and small pores in the foam, the vessel could bear a water pressure up to 0.5 meter of water column (refer to section 3.4.2 and Figure 3-13).

An experimental graphene vessel, which is illustrated schematically in Figure 3-8(a), is shown in Figure 3-8(b). The second frame of the figure gives the picture that was taken after the vessel was put into a container of water covered with crude oil (Kuwait crude oil), showing that the suctioned spilled oil is held in the vessel as a liquid body. Although all sides are rendered transparent with the use of acrylic plates for observation of oil flow except for the two sides of copper mesh plates coated with MGCN, no clear visualization was possible because of the blackness of the crude oil. Therefore, kerosene that was stained blue with Oil Blue N (Sigma Aldrich 391557) was used instead of crude oil, which is shown in Figure 3-9. Because of the clarity offered, demonstrations from here on are made with the stained kerosene for clear visualization.

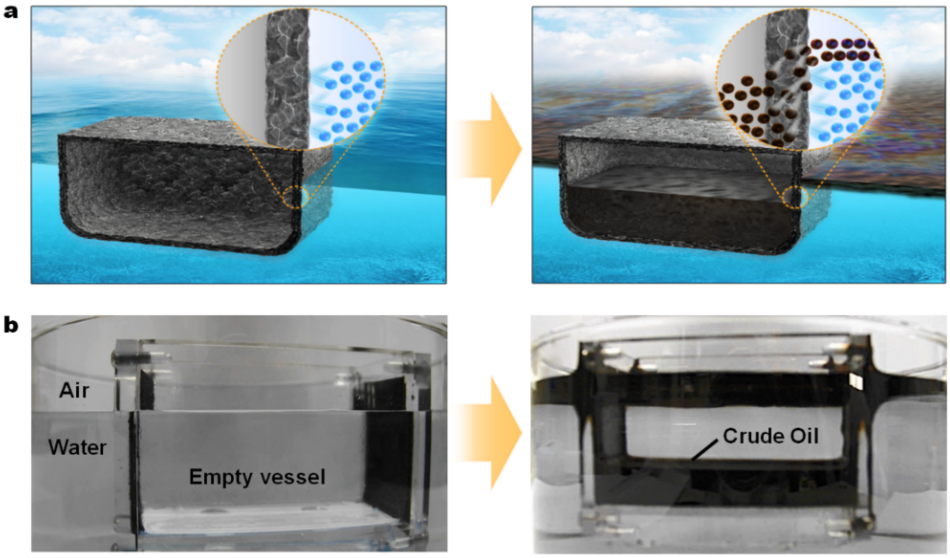

Figure 3-8. (a) Schematic illustration of oil collection by graphene vessel. Graphene vessel floats on the surface of water due to its hydrophobic surface and buoyancy. Water (blue spheres) is repelled by the vessel. When the vessel gets in contact with the oil layer, it quickly absorbs oil (black spheres) by capillary force and oleophilicity of graphene foam. After the oil is fully absorbed in the foam walls of the vessel, the oil is collected into the vessel by gravity through the entire area of the vessel. (b) Optical images of an experimental graphene vessel collecting crude oil. Front, rear, and bottom sides of the vessel except for the two opposing sides were made of acrylic plate for observation. The vessel suctioned the crude oil floating on the water, and held the liquid body of the collected oil in the vessel.

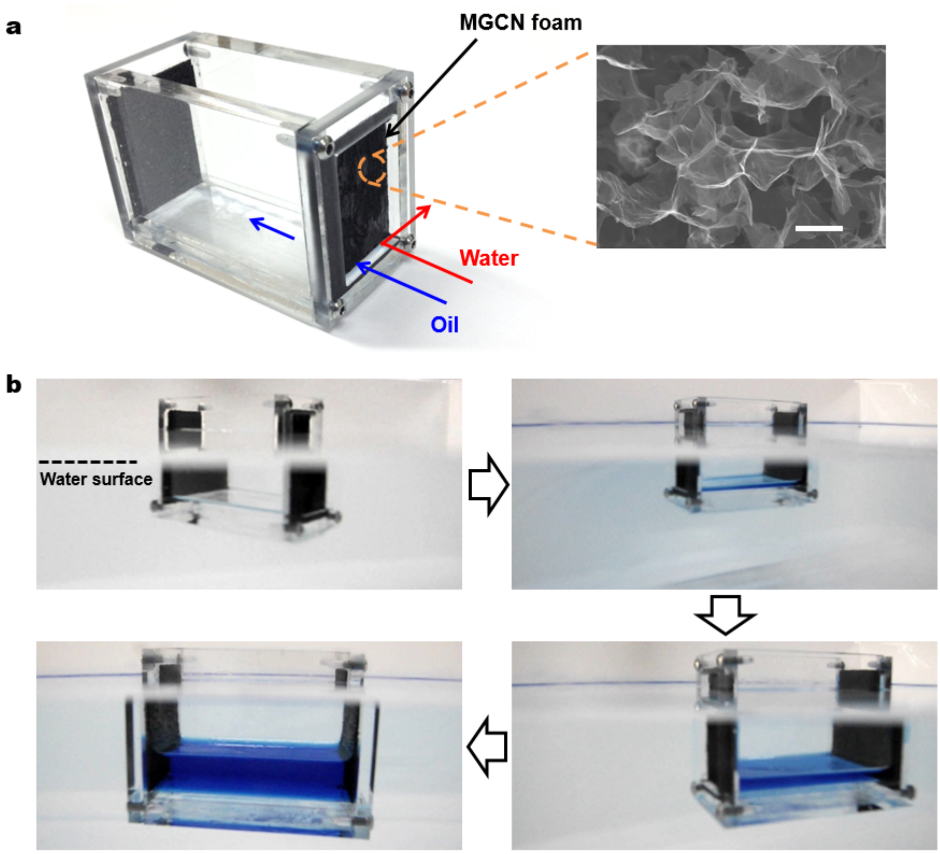

Figure 3-9. (a) Prototype graphene vessel fabricated with acrylic plates that were used for clear observation of oil flow. Only two sides of the vessel are the plates of copper mesh coated with MGCN. Oil was suctioned through the two sides coated with MGCN foam while water was perfectly repelled. The inset is the SEM image of MGCN foam, showing porous three-dimensional structure of the foam. Scale bar is 10 μm. (b) Optical images of graphene vessel floating on oil-covered water. Digital camera was installed in the boundary between water and air to observe the whole vessel. Kerosene stained with Oil Blue N was used for clear observation. The vessel freely floating in water suctioned oil and held the liquid body of the collected oil in the vessel.

3.3.2 Practical demonstration in wavy water

For a practical demonstration in wavy sea, a cubic vessel was fabricated to collect and hold oil under wavy condition (Figure 3-10(a)). The copper mesh plates with MGCN foams were used for all the walls of the vessel to prevent water from entering the vessel when it is tumbled over by heavy wave, with a bit of acrylic panel clearance on all sides for viewing. Even when the vessel was overturned by wave, the collected oil (kerosene) was retained in the vessel due to oil-selective permeable foam and the closed structure of the vessel (Figure 3-10(b)). An additional amount of kerosene was collected as the choppy water gets in contact with the foam on the closed top side. In fact, wavy water condition helps gather more oil for the graphene vessel. Therefore, when oil spill occurs in nasty weather and rough sea, to which the conventional oil containment boom and skimmer are inapplicable, the graphene vessels can be left to float on the sea to collect oil and then picked up later in nice weather.

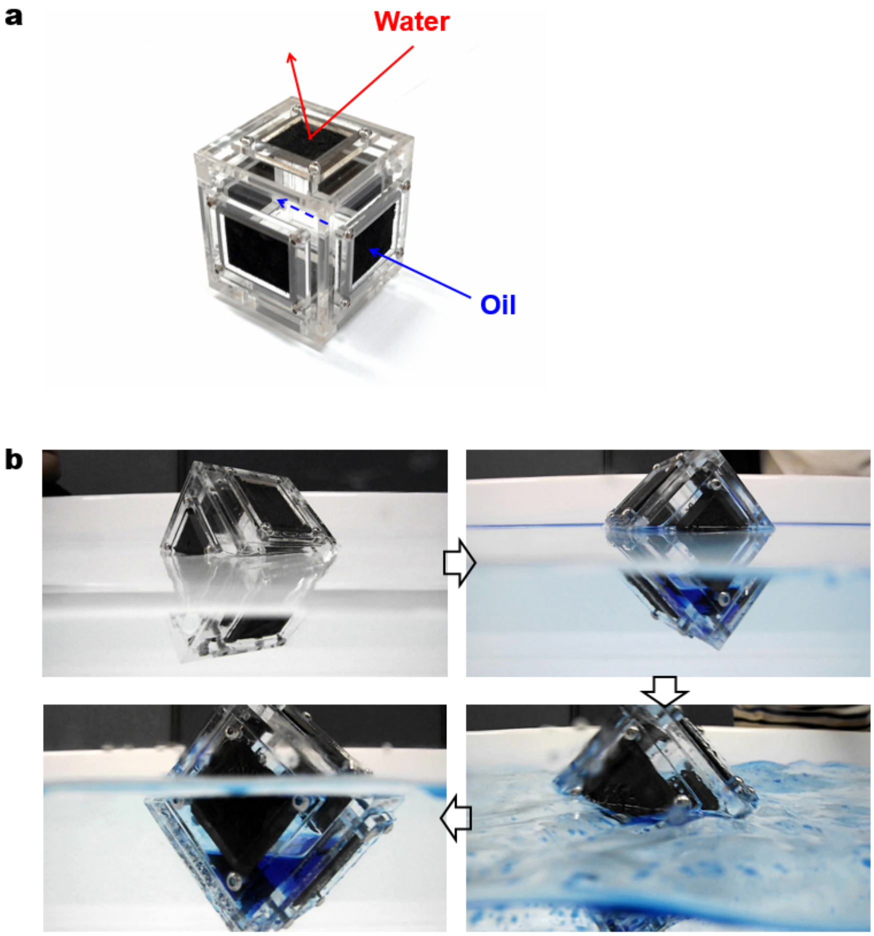

Figure 3-10. (a) Optical image of cube type vessel, all facets of which are coated with rGO foam with a bit of acrylic panel clearance on all sides for viewing. (b) The vessel was able to collect and store kerosene under high wave. Tumbling due to the wave resulted in more kerosene collected as the tumbling led to a better and more contact between kerosene/water mixture and rGO foam.

3.3.3 Practical demonstration using conventional vessel

For another demonstration, MGCN foams were installed in an ordinary vessel and an end of the foam was submerged to continuously collect kerosene (Figure 3-11(a)). Kerosene on the surface of water was suctioned into the vessel through the porous structure due to its high capillary force (refer to section 3.4.4). The height difference between kerosene layer and bottom of vessel enables to continuously collect kerosene by gravity without an external power (Figure 3-11(b)). High capillary rise of MGCN foam can be exploited in a conventional ship by using the foam like a fishnet. It can play a role in pumping oil from graphene vessels to a mother ship like as a non-power pumping hose.

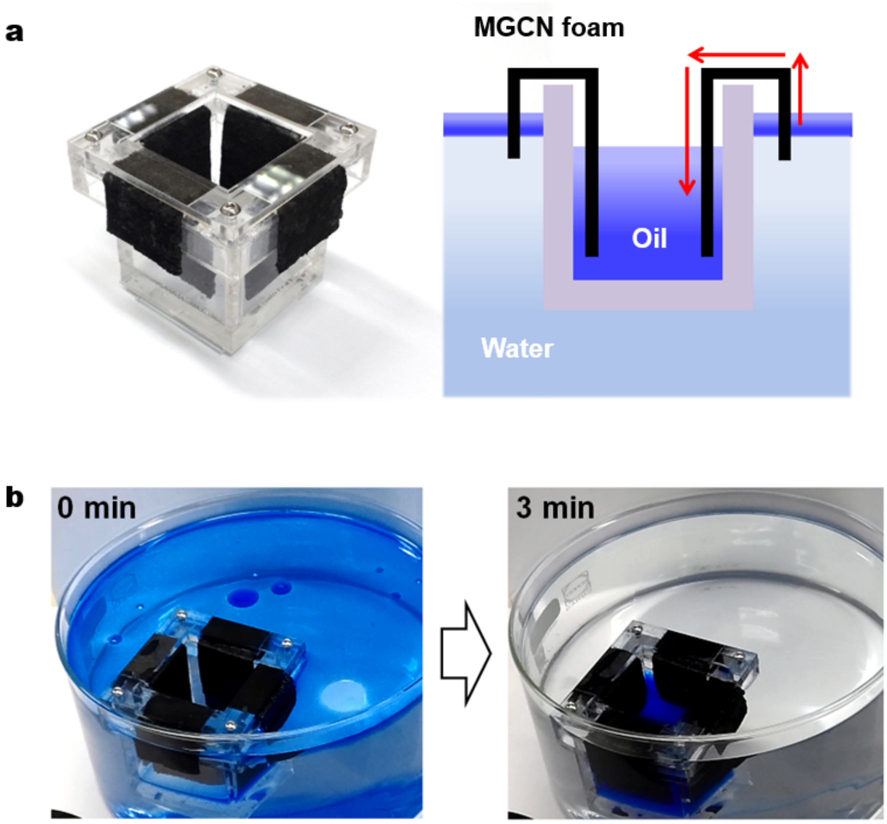

Figure 3-11. (a) Optical image and schematic of MGCN foams installed in an ordinary vessel. Oil is suctioned by capillary force and gravity without an external power. (b) Optical images of the vessel before and after oil collection. Oil was completely collected in the vessel within 3 min.

3.4 Characterization of MGCN foam

3.4.1 Hydrophobicity and oleophilicity

To ascertain hydrophobicity and oleophilicity of the foam, which is needed for the selective separation and suctioning of oil from water, its wetting behavior was examined. The contact angles (CAs) of oil (kerosene) and water were measured on the foam, as shown in Figure 3-12(a) and (b), respectively. A nearly zero CA for oil and a CA of 121° for water clearly reveal its oleophilic and hydrophobic nature of the foam. A kerosene droplet (10 μL), upon contacting the foam surface, was quickly absorbed by the foam (Figure 3-12(c)). The whole process took less than 40 ms, which is the shortest time the camera in the CA analyzer (KRÜSS, DSA100) can handle, suggesting excellent absorption rate and superoleophilicity of the foam. In contrast, a water droplet (4 μL) placed on the foam surface clung to the needle even when pressed onto the surface, implying low adhesion between the foam and water (Figure 3-12(d)). When a large water droplet (10 μL) was dropped on the surface, it bounced several times due to the hydrophobicity of the foam, showing superior water-repellent property (Figure 3-12(e)).

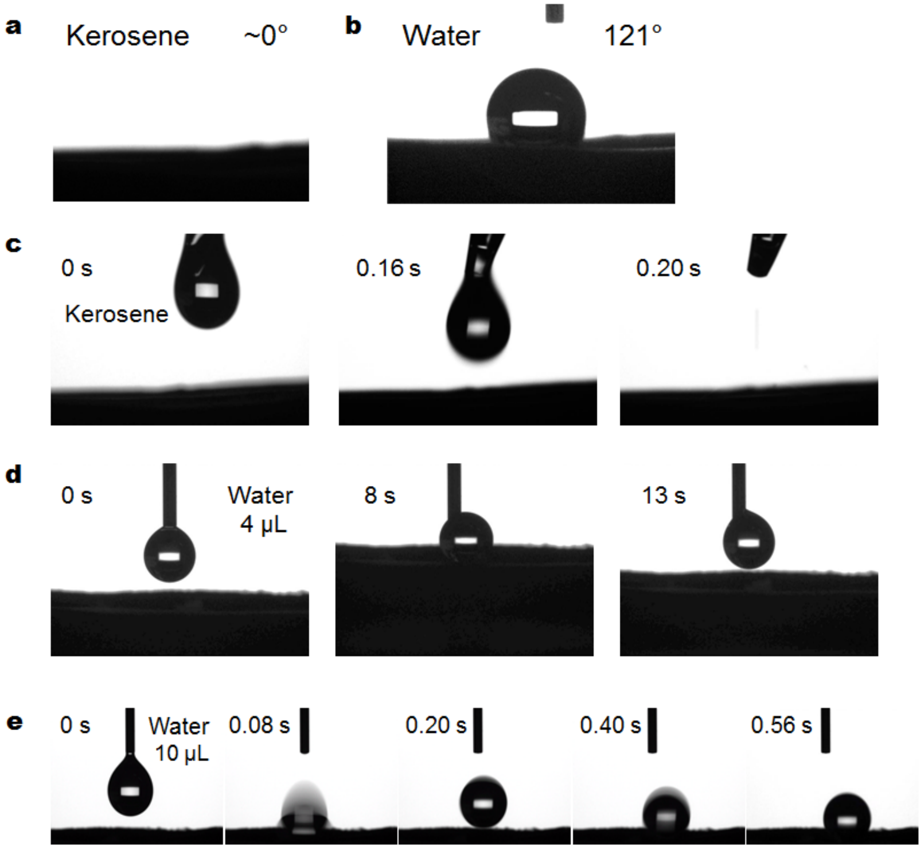

Figure 3-12. Images from a video contact angle (CA) device. (a) CA of oil. Oil (kerosene) was completely absorbed by MGCN foam, showing almost zero CA. (b) CA of water. Water showed a CA of 121° revealing hydrophobic nature of the foam. 10 μL of water droplet was used to determine CA because a droplet smaller than the amount did not stick to the surface of the foam due to low adhesion force between water and foam. (c) Time-lapsed images of kerosene CA measurement. When a kerosene droplet contacted the foam surface, it was quickly absorbed by the foam due to the capillary force and olelophilicity of the foam. (d) Time-lapsed images of water (4 μL) CA measurement. (e) Time-lapsed images of water (10 μL) CA measurement.

3.4.2 Water pressure resistance

The water pressure resistance of the foam was measured to determine the maximum water depth the foam can withstand. Salty water having 3.5 wt% NaCl (Sigma Aldrich S9888) was used to mimic sea water. Water stained by methylene blue (Sigma Aldrich M9140) was poured into a graduated cylinder, the bottom of which is in contact with a copper mesh coated with the foam. The MGCN coated copper mesh was placed on a stopper without any screen or support (Figure 3-13). The foam endured the water pressure exerted by 0.5 m long water column.

The water pressure resistance of a porous media can be obtained by the following equation:

$$h = \frac{2\gamma \cos\theta}{\rho g R} \tag{3-1}$$

where γ, θ, ρ, g, R, and h are the surface tension, the contact angle, the density of water, the gravitational acceleration, the effective pore radius, and the water head, respectively. With the properties of water, the effective pore radius for h of 0.5 m was calculated to be 15.1 μm.

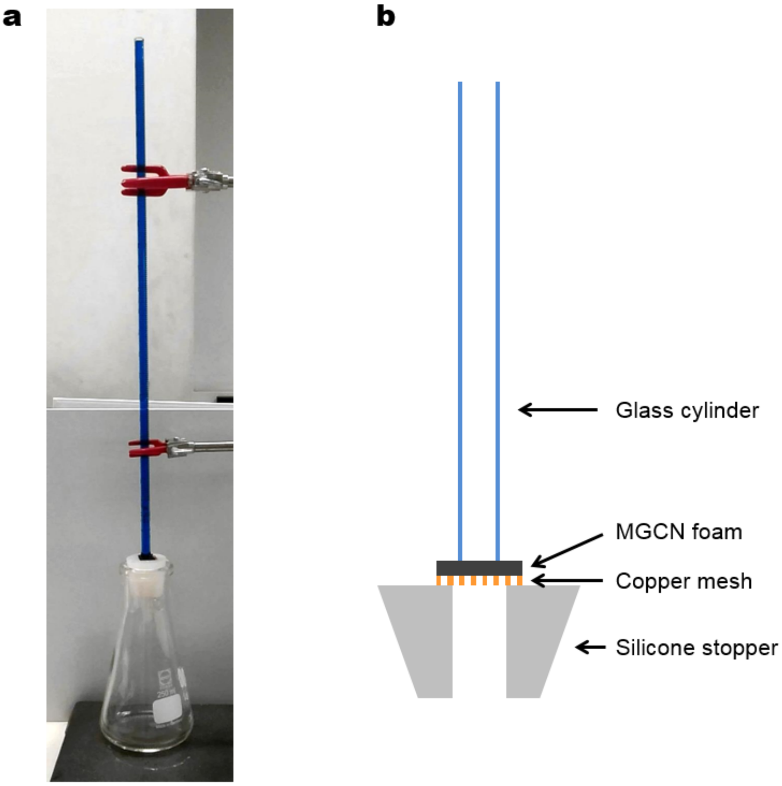

Figure 3-13. Measuring the pressure tolerance of MGCN foam. (a) Optical image of water column (graduated cylinder) loaded above MGCN foam. (b) Schematic diagram of the experimental setup.

3.4.3 Selective permeability

Oil and water permeability of the foam was investigated in a gravity driven filtration system in which kerosene and water were stained by oil red O and methylene blue, respectively, for a clear observation (Figure 3-14). Salty water in which 3.5 wt% NaCl dissolved was used to mimic sea water. Kerosene and water were poured above a copper mesh coated with the foam. The mesh was directly placed above a hole without any support. Kerosene quickly passed through the foam with high permeability due to its oleophilic property (Figure 3-14(a)). In contrast, water stayed above the foam without a leakage for a day, indicating that the foam could act as a selectively permeable membrane (Figure 3-14(b)).

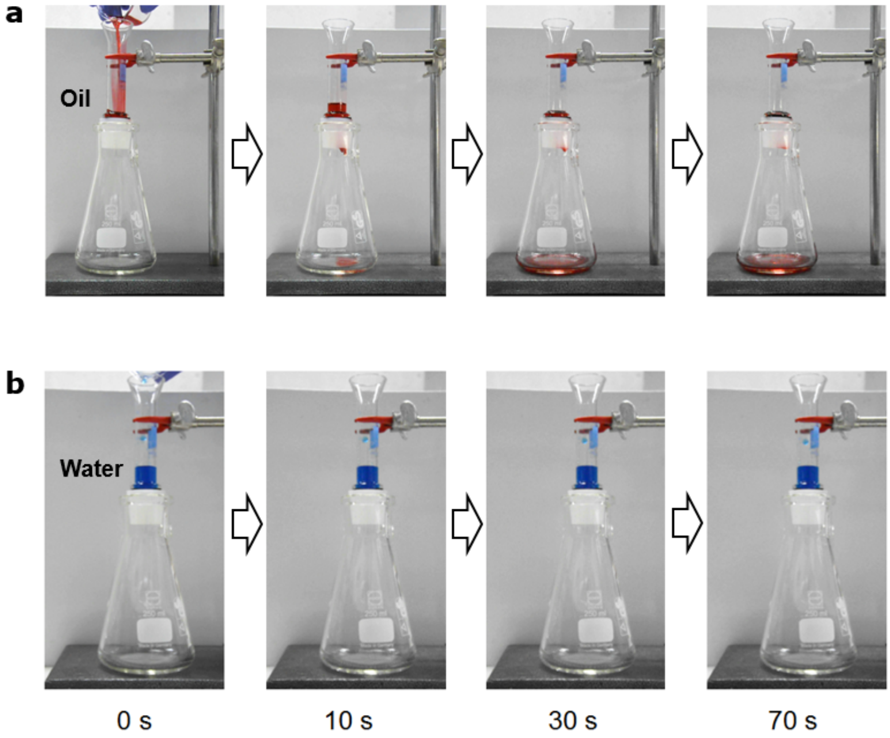

Figure 3-14. Selective permeability of MGCN foam. MGCN foam with copper mesh was directly clamped in a filtration system without an additional supporting material. (a) Optical images of kerosene on MGCN foam. Kerosene was stained by Oil Red O for clear observation. Oil poured on MGCN foam promptly passed, showing oil permeable nature of the foam. (b) Optical images of water on MGCN foam. Deionized water was stained by methylene blue for clear observation.

3.4.4 Capillary rise in MGCN foam

The oil capillary rise in MGCN foam was measured to study the capillary related properties such as effective pore radius. A long MGCN foam, formed on copper plate, was fixed at a plastic substrate (Figure 3-15(a)). To clearly observe the capillary rise, thin paper pieces were attached at regular intervals, and kerosene was sustained by oil red O. As soon as the end of foam contacted kerosene surface, kerosene was rapidly absorbed and raised by capillary force.

Figure 3-15(b) represents the graph of capillary height versus time. The rate of capillary rise decreased with increasing advancing front (height) due to the weight of kerosene. Assuming that the foam was comprised of many vertical capillary tube of radius R, the advancing front h can be determined by following equation with the consideration of capillary force, friction force, and gravity [119].

$$2\pi R\gamma\cos\theta = 8\pi\eta h\frac{dh}{dt} + \rho g\pi R^2 h \tag{3-2}$$

where γ, θ, η, ρ, and g are the surface tension, the contact angle, the viscosity, the density of kerosene, and gravitational acceleration, respectively. In particular, kinetics of flows for a short experimental time can be given by the Washburn equation because the gravity term is negligible [120].

$$h^2 = \frac{R\gamma\cos\theta}{2\eta}t \tag{3-3}$$

The graph shown in Figure 3-15(c) shows the relation between height squared and time (black line) and the fitted line of data for the early stage (red line). The discrepancy between the lines is related to the effect of gravity. From the slope of red line, $\frac{R\gamma\cos\theta}{\eta}$ was turned out to be 1.35×10^{-4} m^2 s^{-1}. By substituting the surface tension, contact angle, and viscosity of kerosene as 0.028 N m^{-1}, 0°, and 0.00164 N s m^{-2}, respectively, the effective pore radius for capillary action was calculated to be 7.91 μm which is of the same order of magnitude as that observed in SEM images.

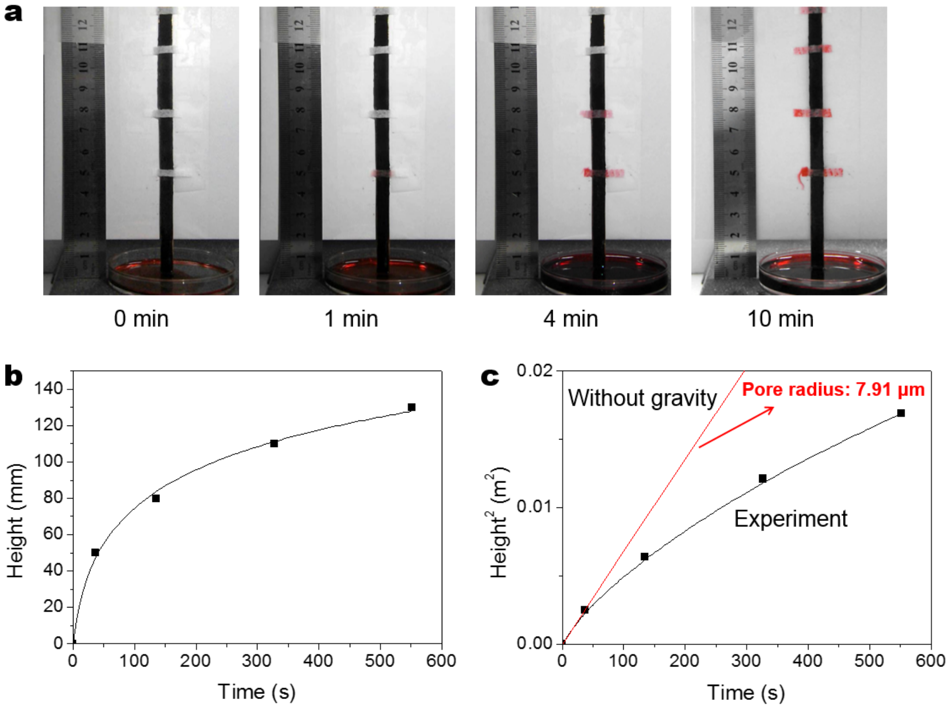

Figure 3-15. (a) Optical images of capillary rise experiment. (b) Capillary height versus time. (c) The graph shows the relation between height squared and time (black line) with the fitted line of data for the early stage (red line).

3.4.5 Oil suction rate of graphene vessel

With the hydrophobicity and oleophilicity of the MGCN foam established, the performance of the graphene vessel was evaluated with the vessel in Figure 3-9(a). It is a rectangular vessel (8 cm × 4.2 cm with depth of 5.4 cm). Typically, a known amount of kerosene was poured into a container filled with water. Salty water having 3.5 wt% NaCl was used to mimic seawater. Figure 3-16(a) gives the suction rate or the amount of oil suctioned into and collected in the vessel in liters per square meter per hour (LMH) (see Figure 3-17 for time series data). The rate is higher than 20,000 LMH. This rate based on the nominal oil thickness increases with decreasing kerosene layer thickness. The calculated nominal oil thickness for the thickness less than 0.5 mm does not represent the real oil thickness. Although the nominal oil thickness that is calculated from the vessel cross-sectional area and the amount of oil collected is 0.5 mm in the figure at the end of oil collection, no oil layer could be detected by naked eyes. This discrepancy is due to some oil adhering onto the container wall as the oil level recedes. Therefore, the suction rate around 0.5 mm does not represent the actual rate.

The oil layer thickness at the oil-foam interface was found to be considerably greater than the actual oil thickness, as shown in Figure 3-16(b), because of the hydrophobicity and oleophilicity of the foam. This extended contact length decreases only slightly with decreasing oil layer thickness and the ratio of the contact length to the oil layer thickness increases (Figure 3-18). The contact length is extended due to the meniscus that forms at the oil-air-foam interface as well as the one at the oil-water-foam interface.

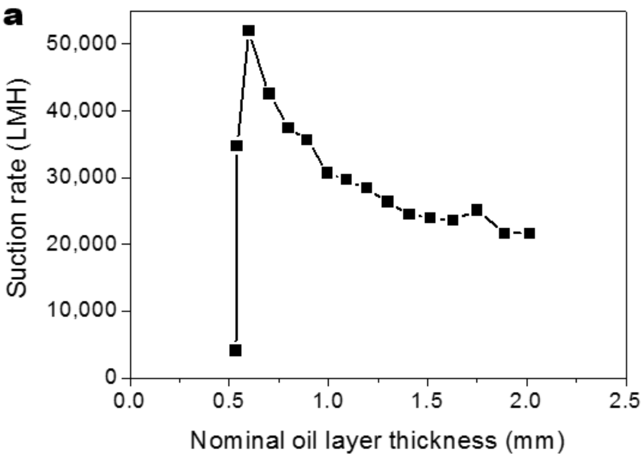

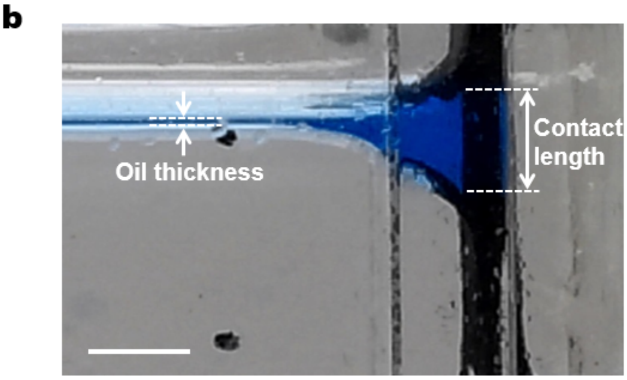

Figure 3-16. (a) Dependence of oil suction rate on the thickness of oil (kerosene) layer. (b) Optical image of oil-water-MGCN foam interface. A contact length much larger than the oil layer thickness exists at the interface because of the hydrophobicity and oleophilicity of the foam. Scale bar is 5 mm.

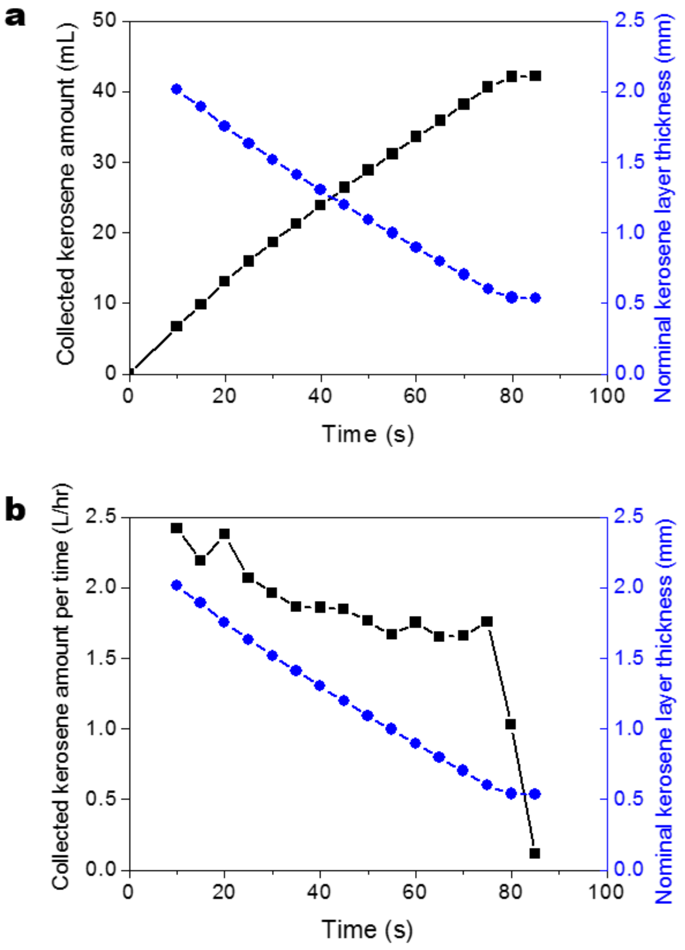

Figure 3-17. (a) Total amount of kerosene collected in the vessel (black rectangles) and nominal kerosene layer thickness (blue circles) versus time. The amount increased linearly with time. The thickness decreased linearly with time due to the decrease in remaining kerosene on water as the oil is removed. (b) Collected kerosene amount per time (black rectangles) and nominal kerosene layer thickness (blue circles) versus time. Note that the collected kerosene amount per time remained at approximately 2 L hr^{-1}, decreasing only slightly with time despite the sharp decrease in kerosene layer thickness.

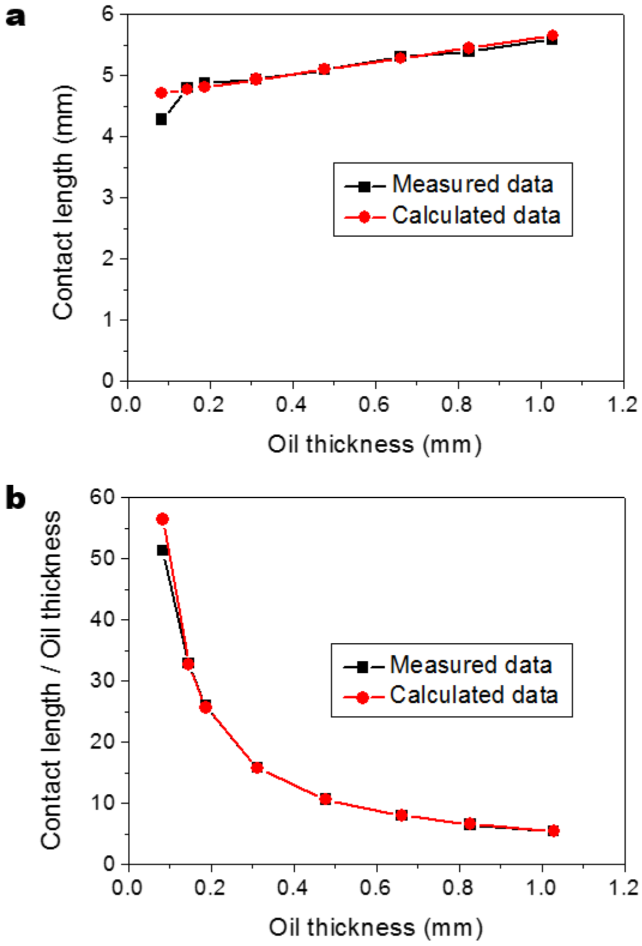

Figure 3-18. (a) Dependence of contact length on thickness of oil (kerosene) layer. (b) Dependence of the ratio of contact length to oil thickness on the oil thickness.

The meniscus height of oil-water-foam interface was 3 times higher than that of oil-air-foam interface due to the larger oil-water interfacial tension compared to the surface tension of oil. Furthermore, a lower contact angle of oil-water-foam interface caused by the hydrophobic and olelophilic nature of the foam resulted in a larger meniscus at oil-water-foam interface.

The contact lengths calculated by Young-Laplace equation with oil properties are in good agreement with experimental results as shown in Figure 3-18(a). Calculated data were obtained by summing the heights of menisci at oil-air interface and oil-water interface, and the oil thickness as follows:

$$\left(\frac{\gamma_{oil}}{\rho g}\right)^{1/2} cot\,\theta_{oil/air/foam} + t_{oil} + \left(\frac{\gamma_{oil/water}}{\rho g}\right)^{1/2} cot\,\theta_{oil/water/foam} \qquad (3\text{-}4)$$

where γ_{oil}, $\gamma_{\mathrm{oil/water}}$, $\theta_{\mathrm{oil/air/foam}}$, $\theta_{\mathrm{oil/water/foam}}$, ρ, g, and t_{oil} are the surface tension of kerosene (~28 mN m^{-1}), the kerosene-water interfacial tension (~48 mN m^{-1}), the contact angle at oil-air-foam interface, the contact angle at oil-water-foam interface, the density of kerosene, the gravitational acceleration, and the oil thickness, respectively. Contact angles were directly measured from optical images as in Figure 3-16(b). The angles were constant in the whole range of oil thickness. The angle at the oil-air-foam interface was 56.6°±1.2° while the angle at the oil-water-foam interface was 36.2°±0.4°.

Because of almost constant contact length, the amount of oil collected per time remains relatively constant. Thus, the graphene vessel, when put into oil-spilled seawater, maintains its high oil collection rate even as the oil thins out. Maintaining a high suction rate until the oil is fully recovered is essential for oil spill accidents, which is difficult for the conventional skimmers and filtering systems to accomplish. Presence of a continuous oil film would be sufficient for ensuring the capillary action and oil collection since then the contact length would be larger than 4.6 mm which is much larger than the effective pore diameter of the foam.

3.4.6 Oil flow path

An interesting aspect of the graphene vessel is that the foam coating the whole vessel provides in effect an expanded area for oil flow. As illustrated in Figure 3-19, oil flows in not only from the oil-foam contact area but more importantly throughout the whole circumference of the coated foam, which enables quick collection of spilled oil.

This aspect was confirmed through a designed experiment. For visualization of oil flow, the vessel surrounded by water was initially filled only with clear kerosene (Figure 3-20(a)). Kerosene stained with Oil Blue N was then introduced to the surface of water surrounding the vessel. The experiment showed that in the initial stage, kerosene flowed in equally throughout the whole area of foam (Figure 3-20(b)). With time, the inflow from the bottom of the vessel gradually increased due to the higher pressure difference at the lower part of the vessel (Figure 3-20(c) and (d)).

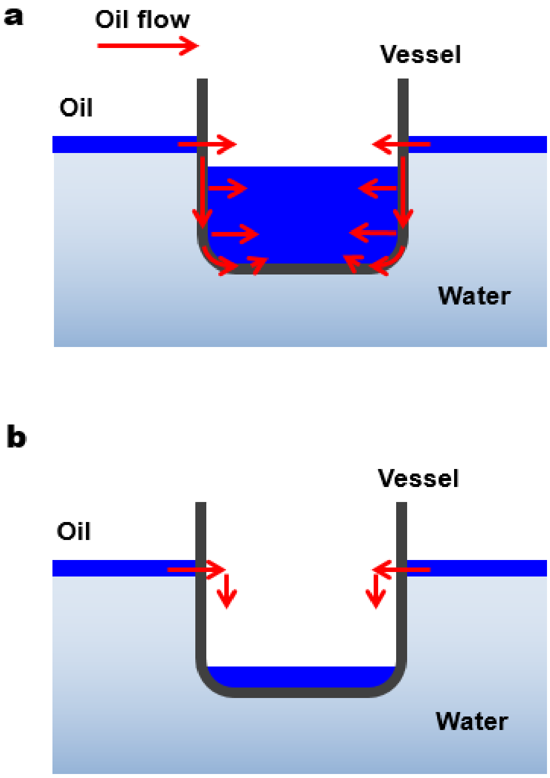

Figure 3-19. Schematics of oil flow when oil flows in (a) through entire area of MGCN foam, (b) only through circumference of vessel that is in direct contact with oil.

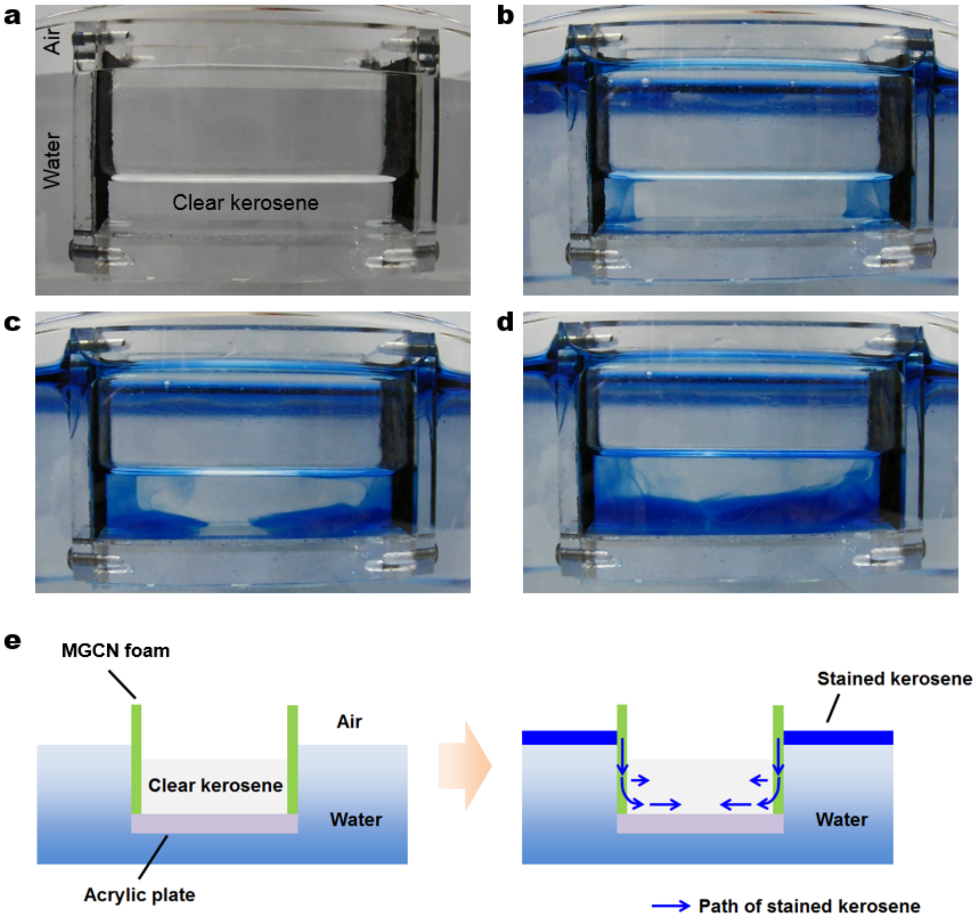

Figure 3-20. Visualization of oil flow during oil collection. (a) Image of the vessel initially filled only with clear kerosene. (b) Optical image of kerosene flow after 7 sec from the time of oil introduction to the water. In the initial stage, kerosene flowed in equally throughout the whole area of foam. Optical images of kerosene flow after (c) 10 sec, (d) 30 sec following the initial flow. The inflow at the bottom of vessel gradually increased, and most of kerosene flowed in through the lower part of vessel. (e) Schematic diagrams of the experiment.

3.4.7 Hydrostatic force

Two forces are at work for the graphene vessel: capillary force and hydrostatic pressure. The capillary force works as a driving force for oil to be suctioned into the foam. For water, on the other hand, it works as a force barring water from entering the foam, thereby enabling selective suction of oil. The hydrostatic pressure forces the oil in the foam to be permeated out of the foam and flow into the vessel (refer to Figure 3-21). Pressure difference between inside and outside the vessel increases with increasing water depth with the slope of $\rho_w g$ in the oil-free region and $(\rho_w - \rho_o)g$ in the oil-filled region where ρ_w and ρ_o are the density of water and oil, respectively. g is the gravitational acceleration.

The hydrostatic pressure acting on the foam integrated over the area is given in Figure 3-22 as a function of collection time. The submerged depth and height of collected kerosene were measured from optical images and the pressure difference was calculated from the depth and height. The integral of pressure difference increased about 30% with time, indicating that the increase in pressure difference due to submerged vessel was larger than the decrease in pressure difference the collected kerosene made.

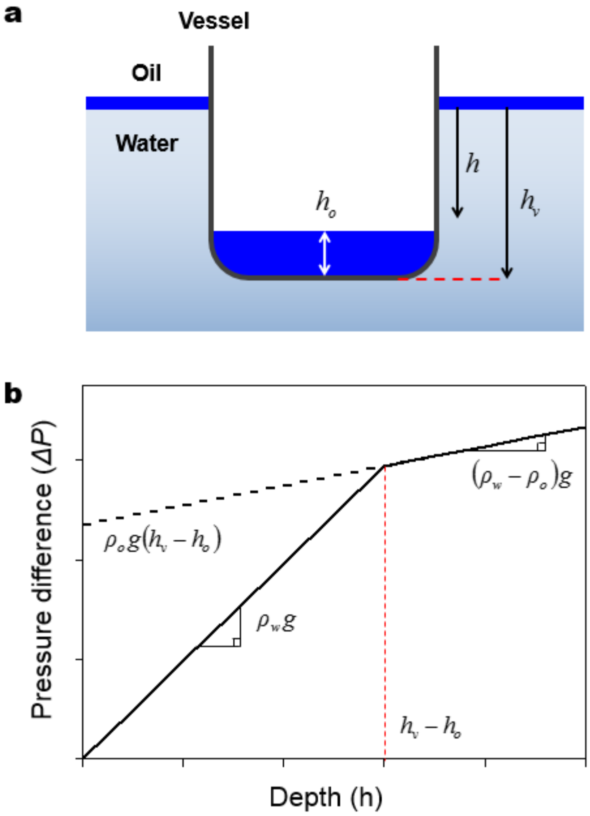

Figure 3-21. (a) Schematic of graphene vessel collecting oil. The symbols, h, h_v, and h_o, denote the depth of water, the depth of vessel, and the height of collected oil, respectively. (b) Pressure difference between inside and outside the vessel as a function of water depth.

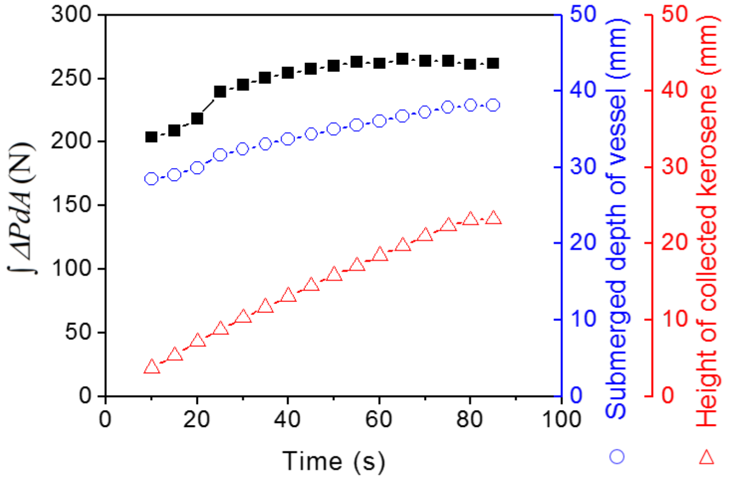

Figure 3-22. Integral of pressure difference, submerged depth of vessel, and height of collected kerosene as a function of time.

3.4.8 The effect of foam thickness on flow rate

The effect of foam thickness on oil flow rate was investigated to find an optimized thickness for oil collection. Two kinds of experimental setups were used to determine the flow rate of oil without water (Figure 3-23(a)) and the flow rate of oil floating in water (Figure 3-23(b)). The thickness of foam was controlled from 0.6 mm to 2.4 mm by changing the process time of IMA. Without water, the flow rate oil (kerosene) decreased with increasing thickness as predicted by Darcy's law, showing flow characteristics in a porous medium (Figure 3-23(d)). On the contrary, kerosene floating in water showed similar flow rate for the whole range of thickness (Figure 3-23(e)). It might be attributed to an indirect flow through a part of foam one side of which contacts with water. Because the indirect flow depends on vertical kerosene flow through foam, the flow rate of thick foam can be higher than that of thin one. Flow rate ratio of kerosene above water to kerosene itself showed a certain tendency to increase according to the thickness of foam. Because graphene vessel suctions oil floating above water and a part of vessel is submerged, foam thickness has a weak influence on suction rate. Generally, a thick membrane improves its separation efficiency but decreases flux, showing trade-off relationship [121, 122]. However, the novel relationship between flux and foam thickness enables us to achieve both high flux and efficiency.

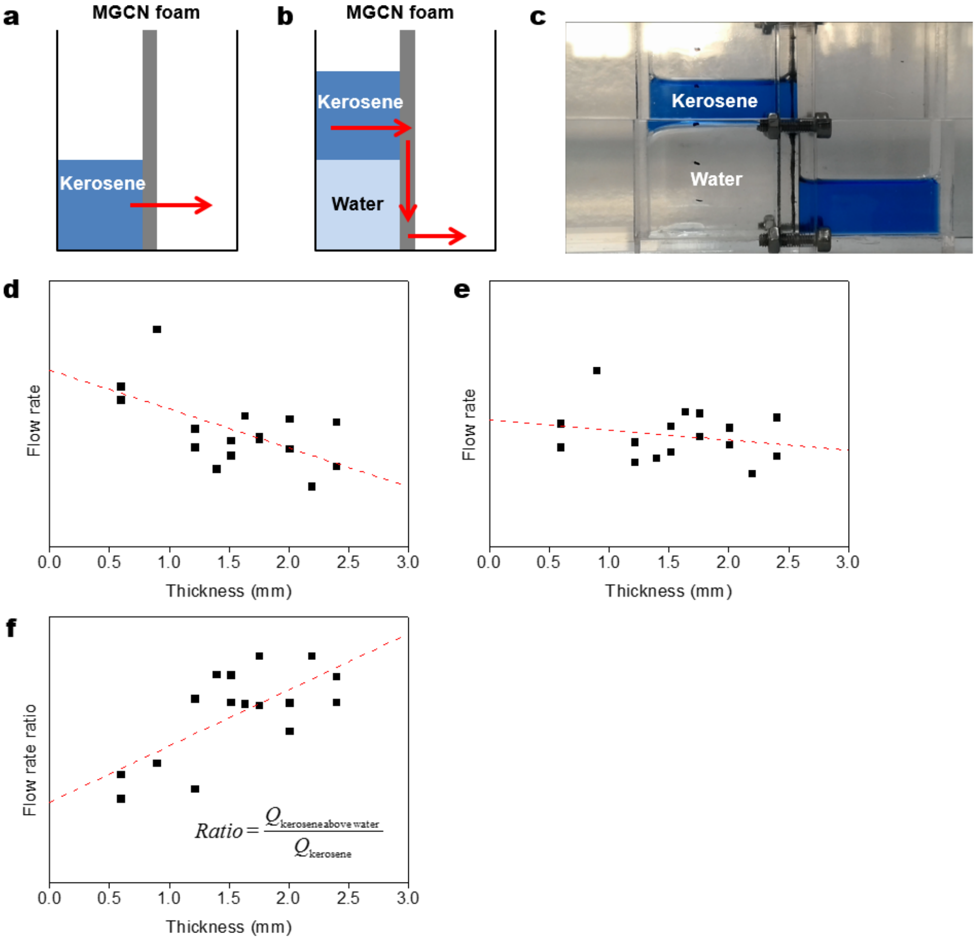

Figure. 3-23. Experimental setups for measuring the flow rate of (a) kerosene without water and (b) kerosene above water. (c) Optical image of the experimental setup (kerosene above water). (d) Flow rate of kerosene without water as a function of MGCN foam thickness. (e) Flow rate of kerosene floating above water as a function of the thickness. (f) Flow rate ratio versus the thickness. Flow rate ratio is defined as the ratio of flow rate of kerosene floating above water to that of kerosene without water.

3.4.9 Separation efficiency

Besides oil suction rate, another performance criterion of interest is separation efficiency. The efficiency measured using Karl Fischer coulometer (Metrohm 831 KF) was better than 99.99% in terms of oil purity. Recyclability of the vessel is of interest for prolonged use. As shown in Figure 3-24(a), there was almost no change in the oil purity, the water content being in 50 ppm range (Figure 3-24(b)), even after the vessel was used 100 times.

Crude oil contains organic solvents such as toluene that may dissolve the material of construction for the vessel. For this reason, the separation efficiency was also measured for various oils and solvents. Gasoline, diesel, n-hexane, toluene, and 1,2-dichlorobenzene were successfully collected by the vessel showing high separation efficiencies above 99.97% as shown in Figure 3-25(a). The water content of various oils and organic solvents were below 300 ppm (Figure 3-25(b)).

Crude oil was collected by a graphene vessel dipped in crude oil to check its chemical stability. The vessel retained its selectively permeable property even after it had been dipped in crude oil for one month (crude oil image in Figure 3-25(c)), revealing its superb chemical stability.

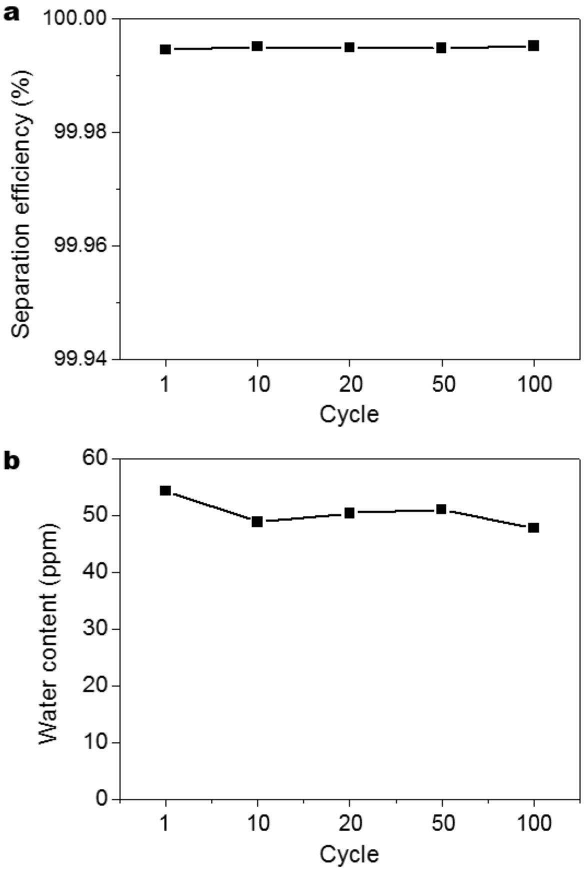

Figure 3-24. (a) Recyclability of graphene vessel in terms of separation efficiency (oil purity). The efficiency was maintained better than 99.99% even after 100 cycles of usage, showing reliable reusability of the graphene vessel. (b) Water content of oil the vessel collected as a function of cycles of usage.

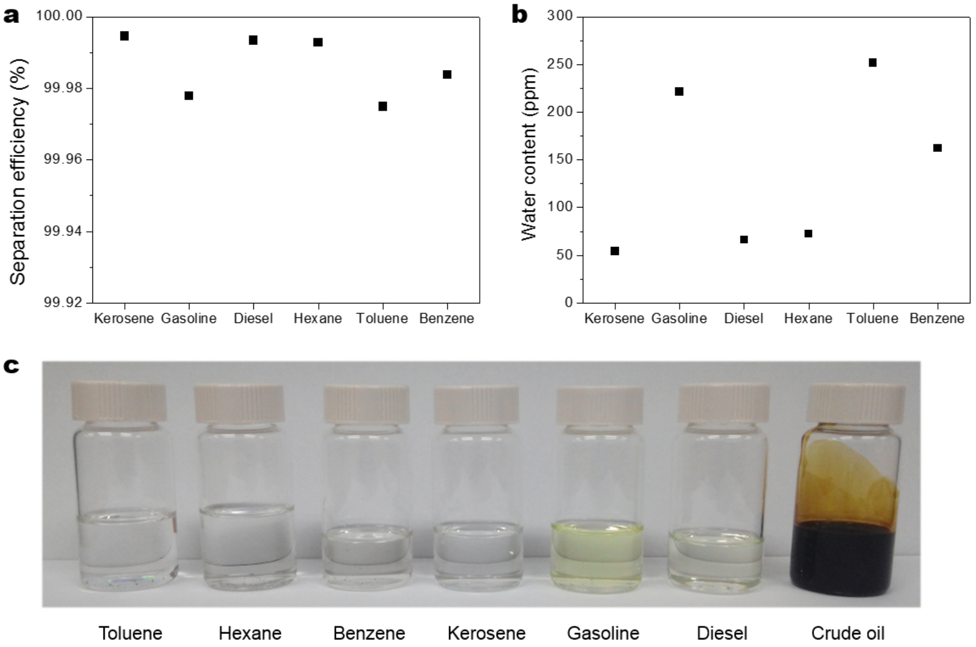

Figure 3-25. (a) Separation efficiency of various oils and organic solvents. (b) Water content of various oils and organic solvents. (c) Optical image of various organic solvents and oils collected by graphene vessel.

Chapter 4. Physical nature of countless sharp edges

In this chapter, a MGCN foam was utilized as high performance emitter by taking advantage of physical nature of countless sharp edges in the foam. A rapid vacuum drying process is used after IMA process, which enables to fabricate highly porous structure by vigorous escape of water molecules in an instant. With numerous countless sharp graphene edges, the MGCN foam emitter shows outstanding field emission properties, such as a low turn-on electric field of 1.06 V μm^{-1}, threshold field of 1.42 V μm^{-1}, and long-term emission stability, which are superior to those of graphene emitters previously reported.

4.1 Background of field emission

4.1.1 Field emission theory

Field emission also known as field electron emission means emission of electrons from the surface of a condensed phase into another phase by an external electrostatic field. The most common phenomenon is emission of electrons from metal surface to vacuum, discovered independently from 1880s and explained by quantum tunneling of electrons in 1920s. In contrast to thermionic emission or photoemission where heat or light is supplied to electrons in an emitter to overcome the potential barrier at the metal-vacuum boundary, field emission is a phenomenon of the tunneling of electrons through the deformed potential barrier at the surface of metal. As shown in Figure 4-1, the potential barrier is strongly deformed by an external field to make thin barrier, thereby, electrons in metal can be emitted by tunneling through the barrier.

The theory of field emission from bulk metal was first developed by Ralph H. Fowler and Lothar Wolfgang Nordheim. They first derived the tunneling probability of electrons from metal surface using quantum mechanics. In the derivation, it is assumed that (1) electron tunneling occurs through a rounded triangular barrier; (2) the barrier is one-dimensional (with no lateral structure). The Fowler–Nordheim (F–N) equation, relation between current density and applied electric field, is given by

$$J = a\emptyset^{-1}E^{2}\beta^{2}\exp\left(-\frac{b\emptyset^{3/2}}{\beta E}\right) \tag{4-1}$$

where ϕ is the work function of emitting material, J is the current density, E is the local electric field, and β is the local electric field enhancement factor. a and b are constants with 1.54×10^{-6} A eV V^{-2} and 6.83×10^{9} $eV^{-3/2}$ V m^{-1}, respectively.

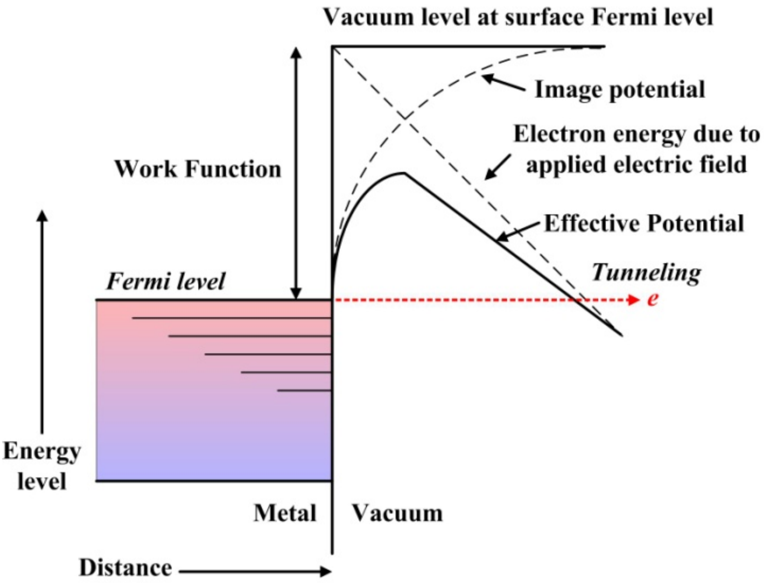

Figure 4-1. Plot of electron energy level in metal-vacuum system for field emission [123].

4.1.2 Recent research on field emission using nanomaterials

With the superior field emission performance such as low turn-on voltage, high emission current density, and long-term emission stability, electron field emissions based on sharp and tapered nanomaterials have been extensively studied as an alternative of thermionic emission. Various nanomaterials including carbon nanotube [124-127], ZnO [128], SnO_2 [129], In_2Se_3 [130], LaB_6 [131], $WO_{2.72}$ [132], and GaN [133] have been used for the fabrication of field emitters (Figure 4-2(a)).

In particular, the nature of atomically sharp edges of two-dimensional materials, such as WS_2 [134], MoS_2 [135], ZnO [136], V_2O_5 [137], black phosphorus [138], $NiCo_2O_4$ [139], and graphene [140-146] sheets, reduces greatly turn-on and applied voltages for electron emission owing to the local amplification of electric field (Figure 4-2(b)). Of these layered materials, graphene and its derivatives have received a great deal of attention with superb emission property and high enhancement factor, stemming from the unique two-dimensional atomic structure and extraordinary electrical property [140-156].

To fabricate graphene emitters with desirable configuration and orientation suitable for field emission, various methods including direct growth [140, 147-149], screen printing [150, 151], electrophoretic deposition (EPD) [141, 152, 153], filtration [154], spin coating [155], and bar coating [156] have been developed (Figure 4-3).

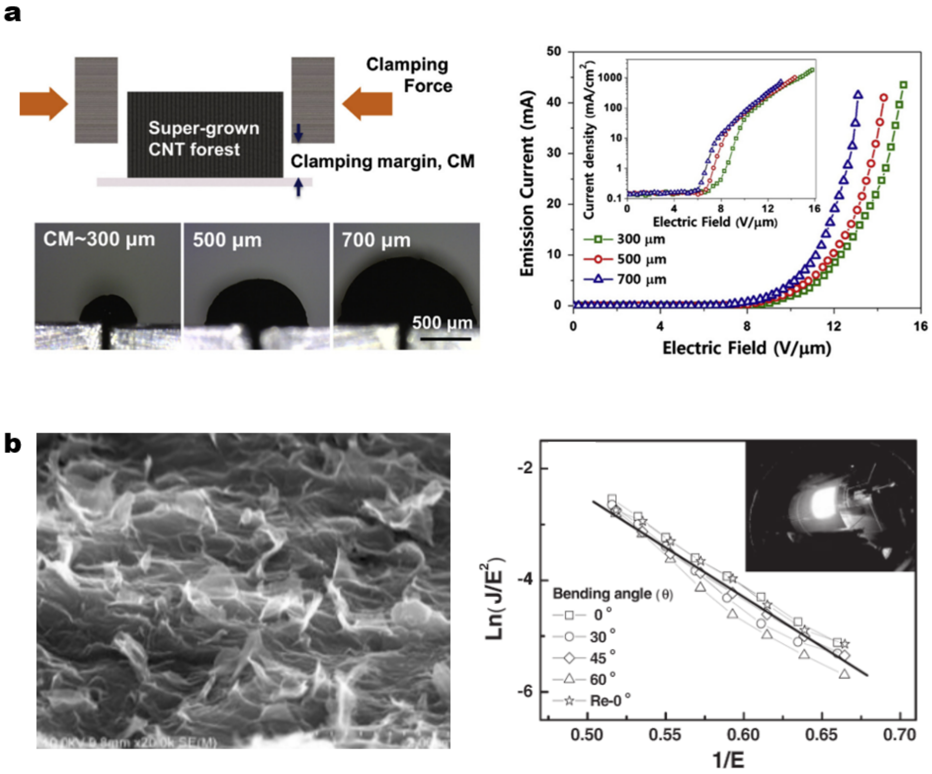

Figure 4-2. (a) Schematic, microscopy images, and performance data of carbon nanotube field emitter [127]. (b) SEM image and performance data of graphene field emitter [142].

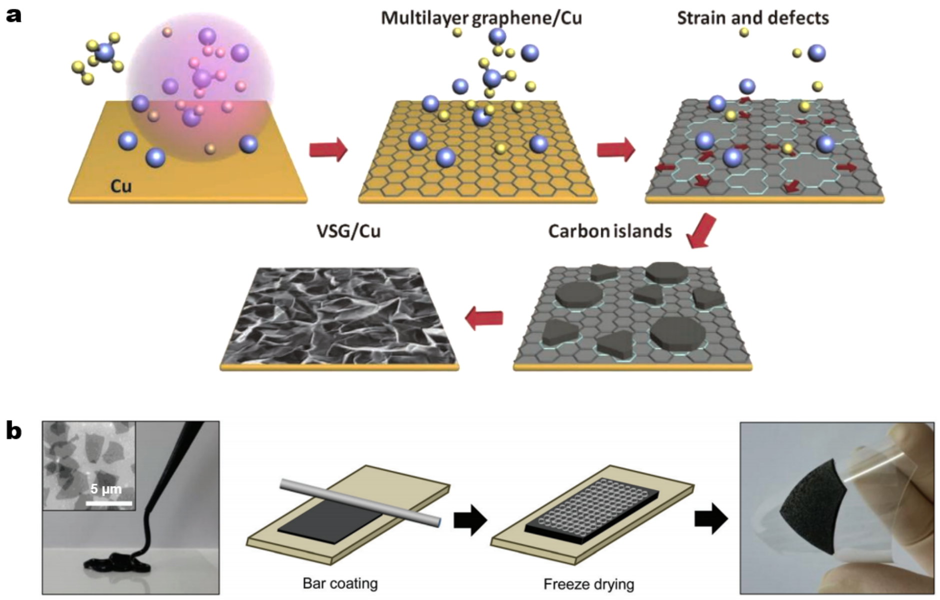

Figure 4-3. (a) Schematic growth process of graphene filed emitter on copper substrate in chemical vapor deposition system (direct growth) [140]. (b) Schematic of fabrication of the 3-D rGO structure by the bar coating of a rGO paste [156].

4.1.3 IMA process for the fabrication of field emitter

Among the methods introduced in section 4.1.2, the EPD of graphene is cost effective and a versatile processing technique to fabricate a two-dimensional graphene planar emitter. EPD has great advantages in obtaining thin films from charged colloidal suspensions, such as high throughput, precise thickness control, and simplicity of scale up.

EPD basically requires charged colloidal particles in a liquid-phase suspension, and the particles are forced to move toward the oppositely charged electrode under an electric field. When adopting negatively charged graphene oxide (GO) suspension for EPD, GO platelets will be deposited to a positive electrode in which the electrochemical reaction is biased toward the oxidation of GO. Therefore, previous EPD studies generally have used the suspension of reduced graphene oxide (rGO) modified with positive charges for deposition on a negative electrode [141, 152, 157]. To render rGO platelets positively charged, metal salts were introduced to the suspension so that positively charged metal ions are absorbed onto rGO surface. However, the solubility tolerance of metal-absorbed rGO is typically much lower than that of GO due to the lack of oxygen functional groups [58]. Low concentration of rGO solution leads to low deposition rate in EPD process even though a high electric field (~typically 100-320 V cm^{-1}) is applied [141, 152], which has hindered the use of electrophoretic deposition of graphene in scalable and productive applications.

In this chapter, IMA method was utilized to fabricate graphene field emitters. Direct fabrication of 3-D GO structure from GO colloidal solution could be possible in a single step process with high deposition rate. The process employs both Cu electrodes immersed in highly concentrated GO solution. Upon applying dc voltage between electrodes, negatively charged GO platelets are rapidly attracted to the Cu anode, and are simultaneously linked to form GO hydrogel (MGCN hydrogel). It is noteworthy that the deposition process is accomplished at a low voltage (4 V) in a short period of time (10 sec).

In the present study a rapid vacuum drying process is demonstrated to obtain the porous structure suitable for field emission by vigorous escape of water molecules from graphene hydrogel in a short time.

The fabricated MGCN foam on a Cu electrode with further annealing shows high electrical conductivity and involves numerous sharp edges of graphene. The MGCN foam emitter shows outstanding field emission properties, such as a low turn-on electric field of 1.06 V μm^{-1}, threshold field of 1.42 V μm^{-1}, and long-term emission stability with a current density of 9.2 mA cm^{-2} for 22 hours. The method used here could be available to various geometries of substrates such as rod, plate, and flexible wire. By employing the flexibility of the electrode, the emitter is applicable to luminescent lighting tube and also provides a winding structure that requires high-current electron sources [158-160].

4.2 Fabrication of field emitter

4.2.1 MGCN foam and film emitter

GO powder was prepared with the same method mentioned in section 2.2.1. GO powders in the form of sheet were prepared via a filtration process. GO sheet was re-dispersed in deionized water with a controlled concentration of 1.0 mg mL^{-1} by sonication.

After the preparation of GO suspension, two identical Cu wire electrodes were immersed in the suspension as shown in Figure 4-4. Then, dc voltage was applied between the electrodes with a range from 4 to 10 V for 10 sec. The inter-electrode spacing was fixed as 1 cm. The GO platelets in the solution migrated toward the positive electrode due to their negatively charged surface which was induced by oxygen functional groups, such as epoxy, hydroxyl, carbonyl, and carboxyl groups, existing on basal plane and edge of GO platelets. During the IMA process, GO platelets were linked by copper ions to make 3-D hydrogel structure (MGCN). After completing the deposition process, the electrode coated with MGCN hydrogel was dried in two different manners; (1) ambient air drying and (2) rapid vacuum drying at room temperature, as shown in Figure 4-5(a) and (b).

The inset SEM image of Figure 4-5(a) shows that the MGCN dried in ambient air had a neatly stacked structure similar to GO paper-like materials prepared by filtration [116]. Surface tension of water between the GO platelets might attribute to the packing morphology. On the other hand, the MGCN electrode dried in a vacuum chamber exhibited highly porous foam structure as shown in Fig. 4-5(b) and the inset of the figure. Vigorous escape of water molecules from the MGCN hydrogel during the drying process does not allow enough time to rearrange GO platelets, resulting in a porous structure with vertically aligned platelets. It is noteworthy that the rapid vacuum drying process is completed at a chamber pressure of 1.0×10^{-2} Torr in a short time (~10 sec).

Finally, the MGCN electrode was annealed at 200 ^{o}C under Ar gas flow for 5 hours for reduction of GO and removal of remaining water molecules.

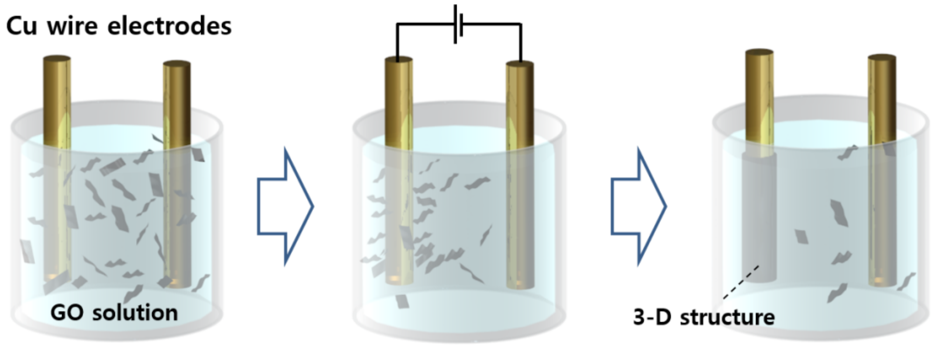

Figure 4-4. Schematic of IMA process for the fabrication of a cylindrical field emitter.

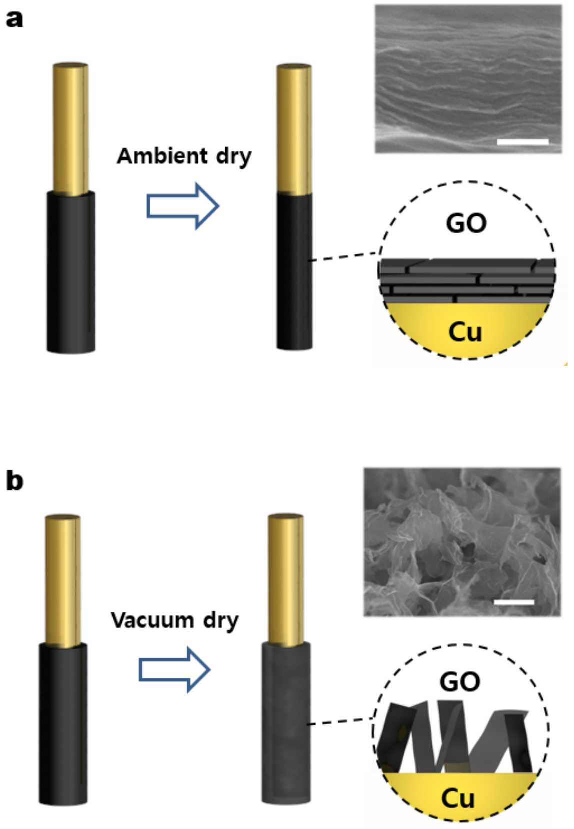

Figure 4-5. Schematics of (a) ambient drying and (b) vacuum drying processes. Scale bars in (a) and (b) are 200 nm and 10 μm, respectively.

4.2.2 Morphology of MGCN emitter

Figure 4-6 shows the optical images of the MGCN coated wires before and after drying processes at ambient air and vacuum conditions, respectively. Thickness of the MGCN structure significantly decreased during the drying process at ambient air while the MGCN structure dried at vacuum kept its shape.

Even under severe bending deformation, the foam-like MGCN layer does not show any delamination from a wire electrode and breakage into small pieces of debris (See Figure 4-7(a)). It indicates that strong linkages between rGO platelets in the foam as well as high interfacial strength between MGCN and electrode were successfully formed. As long as a substrate is electrically conductive, uniform and homogeneous MGCN foam could be fabricated regardless of its geometry because IMA process is mainly depending on the electric field around the electrode. The present method was applied to a planar Cu plate in the same manner. MGCN foam was also successfully fabricated on the plate as shown in Figure 4-7(b).

Thickness of the MGCN foam could be controlled by varying the applied voltage and processing time. As shown in Figures 4-8 and 4-9, the thickness increases almost linearly with the applied voltage ranging from 4 to 10 V at a fixed processing time of 10 sec.

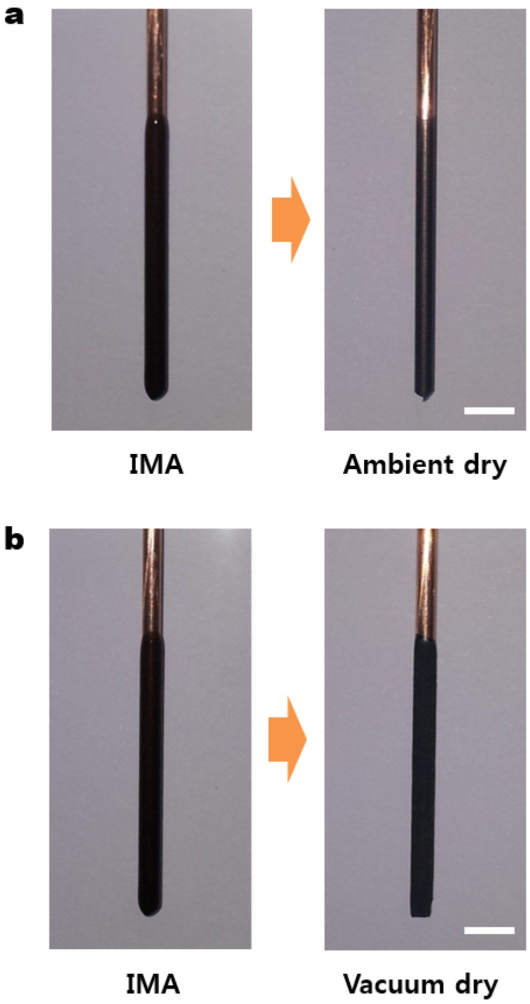

Figure 4-6. Optical images of MGCN coated copper wires dried in two different manners; (a) ambient air and (b) vacuum dryings at room temperature. Scale bar is 5 mm.

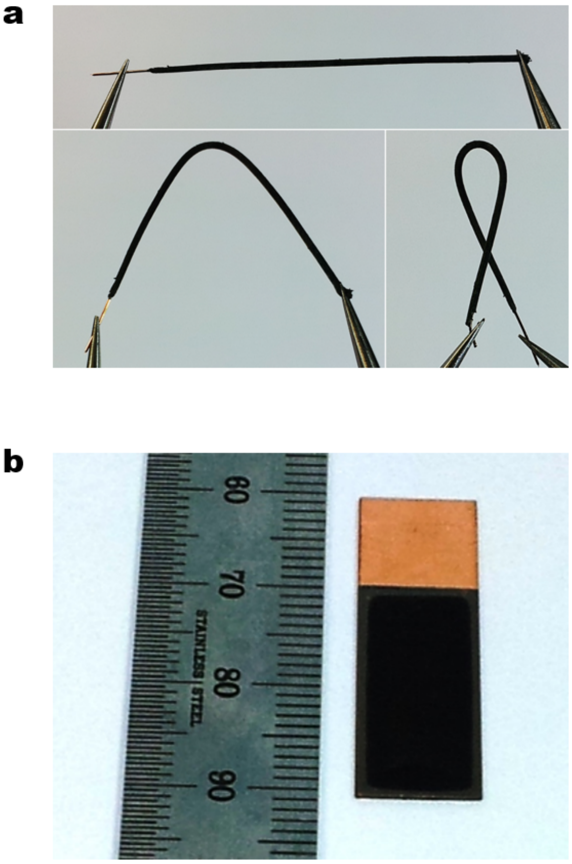

Figure 4-7. (a) Optical images of MGCN coated wire. Even under severe bending deformation, the foam-like MGCN layer does not show any delamination from a wire electrode and breakage into small pieces of debris. (b) Optical image of MGCN coated planar plate.

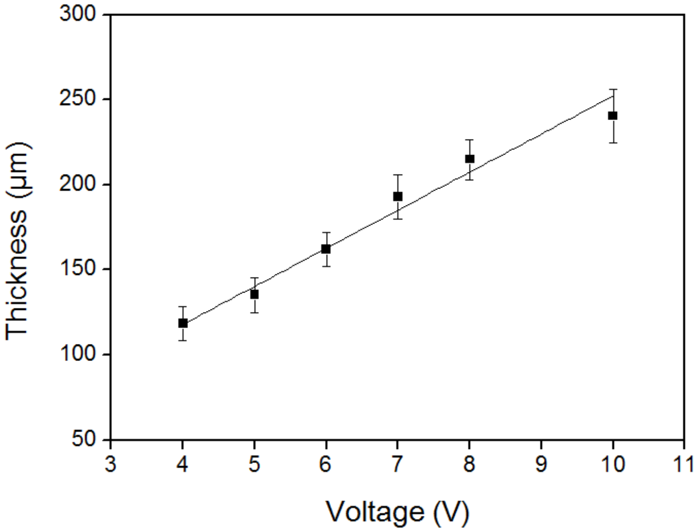

Figure 4-8. The thickness of MGCN foam could be easily controlled by varying the applied voltage. The thickness increases almost linearly with increasing the applied voltage ranging from 4 to 10 V at a given processing time of 10 sec. The diameter of a copper wire is 300 µm.

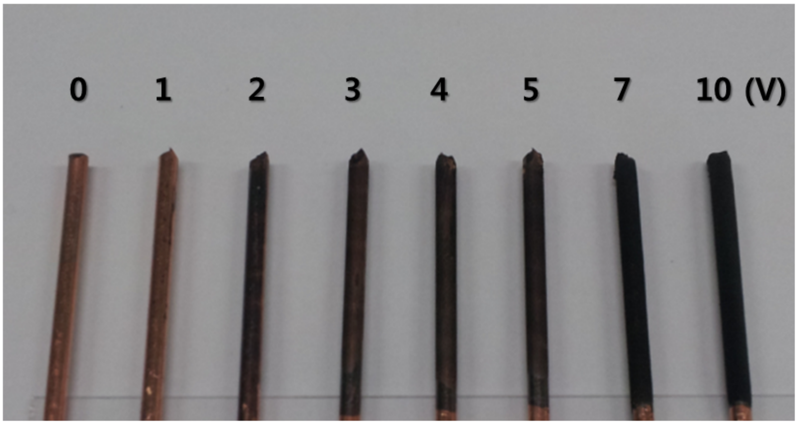

Figure 4-9. Optical image of MGCN foam emitters with various applied voltages. The diameter of a copper wire is 2 mm.

Figure 4-10(a) shows SEM image of the MGCN foam fabricated with an applied voltage of 5V for 10 sec. Individual rGO platelets were well interconnected each other by forming a highly porous 3-dimensional network. Close observation of MGCN foam at an inclined angle (Figure 4-10(b)) reveals that rGO platelets with a lateral size of several micrometers stand vertically, providing numerous sharp edges. It is also noteworthy that individual rGO platelets in the foam are spatially separated with distance of several micrometers. The sharp edges are advantageous by serving as active sites for field emission of electrons and the spatial distribution of rGO could decrease the screen effect felt by individual platelet in the emitter, resulting in lower turn-on and threshold fields.

Figure 4-10(c) shows the cross-sectional SEM image of the emitter. The MGCN foam shows a homogeneously porous morphology in the structure. Any delamination and void were not observed along the interface between rGO platelets and the electrode. It might be advantageous to robust electrical and thermal conductance at the interface, which is crucial to achieving high performance of field emitter. Figure 4-11(a) and (b) show the cross-sectional SEM images of MGCN foams fabricated on a planar Cu plate and a Cu foil (25 μm), respectively. Likewise the foam structure on the Cu wire, the MGCN foam also shows uniform morphology along thickness direction on the Cu plate. No delamination or void was observed at the interface between the foam and the plate (or foil).

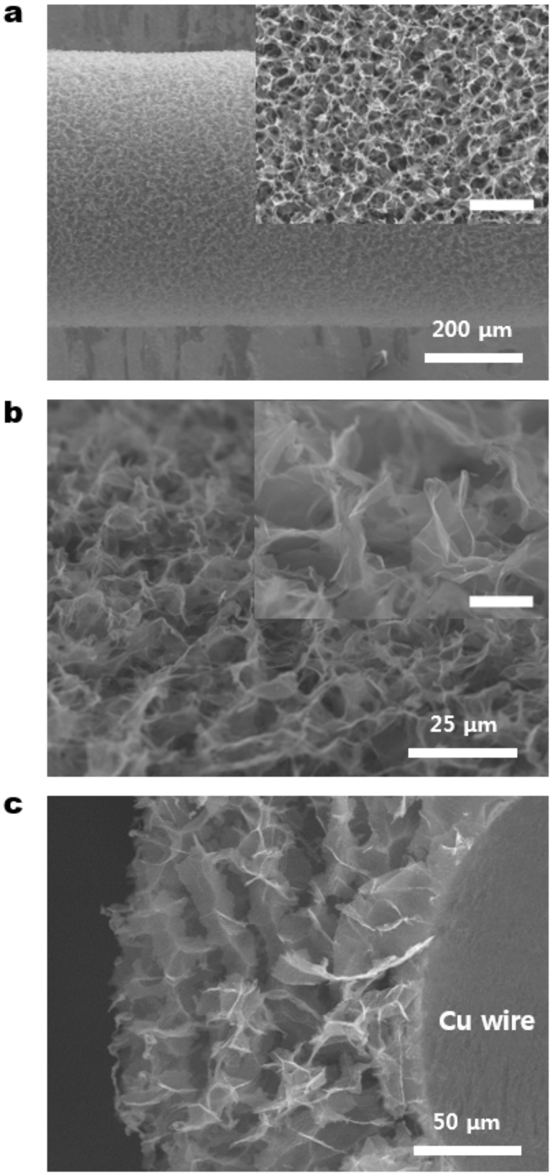

Figure 4-10. (a) SEM image of MGCN foam fabricated with an applied voltage of 5 V for 10 sec. (b) Close observation of the MGCN foam at an inclined angle. (c) Cross-sectional SEM image of the emitter. Scale bar in the inset of (a) and (b) are 50 µm and 5 µm, respectively.

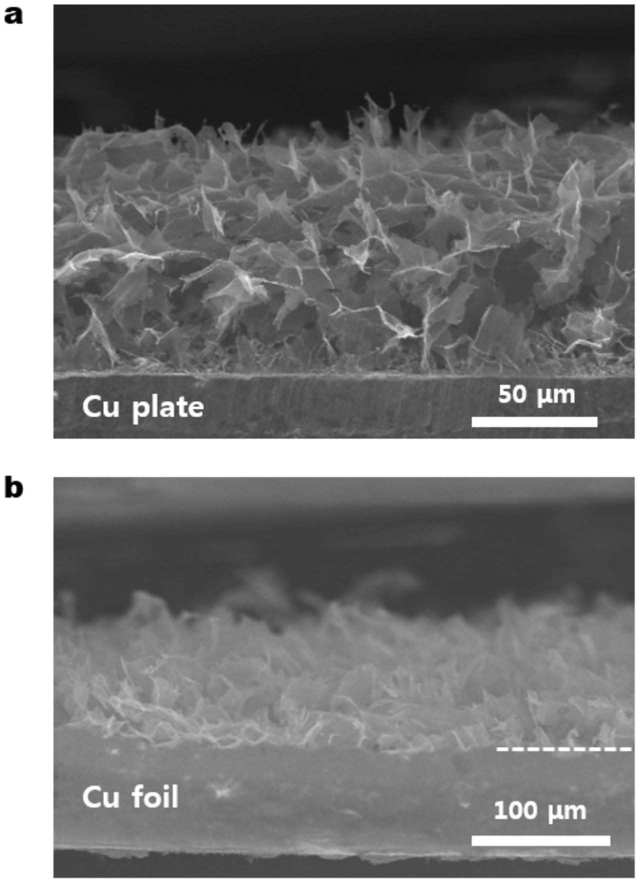

Figure 4-11. Cross-sectional SEM images of MGCN foam fabricated on (a) a copper plate and (b) a copper foil.

4.3 Field emission performance

4.3.1 Experimental setup

Investigation on field emission performance of the MGCN foam was performed using molybdenum (Mo) tube used as an anode and the experimental setup shown in Figure 4-12(a). A 50 μm-thick MGCN foam deposited on 2 mm-diameter Cu wire was used as a cathode for field emission. Ambient air-dried MGCN film was also tested under the same experimental setup. Stainless steel was used as a mechanical clamp in a cathode part. A voltage between MGCN foam cathode and Mo anode was applied using a dc power supply (Matsusada Precision Inc.). Field emission current was measured by a multimeter (Keithley, 2000).

While a planar emitter has an electric field of $E = V/d$ with an inter-electrode distance (*d*), a cylindrical emitter has a different effective distance of $r_1 \ln(r_2/r_1)$ which results in an electric field of $E = V/[r_1 \ln(r_2/r_1)]$ with radius of emitter (r_1) and inner radius of anode (r_2) (See Figure 4-12(b)) [160]. Effective distance between cathode and anode was calculated as 470 μm.

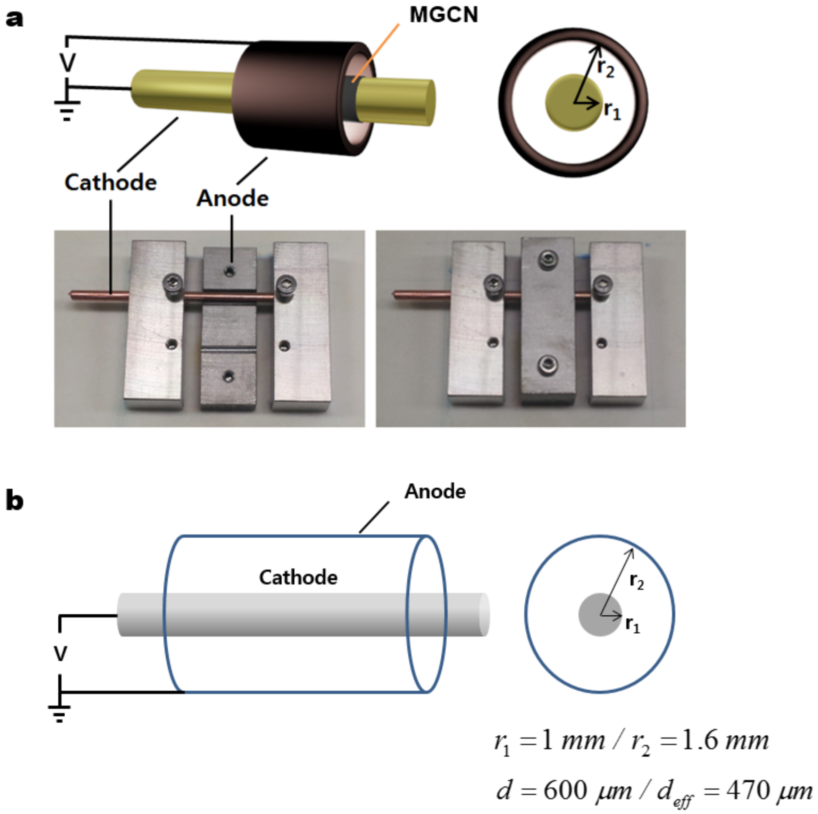

Figure 4-12. (a) Optical images and (b) schematics of the experimental setup for field emission.

4.3.2 Turn-on and threshold field

Current-voltage (*I-V*) characteristics of the emitters were investigated in a vacuum chamber at a base pressure of 3.0×10^{-7} Torr as shown in Figure 4-13(a). An optimized MGCN foam emitter was fabricated by the applied voltage of 4 V (Figure 4-13(b)) when GO concentration is 1 mg mL^{-1} and process time is 10 sec. MGCN foam emitters fabricated by higher voltage might suffer from high electrical resistance due to increased foam thickness and low emission site density due to large pore size (See section 2.2.4).

While a MGCN film emitter showed a high turn-on electric field (electric field needed to produce a current density of 10 μA cm^{-2}) of 10.8 V μm^{-1} with little current density over an applied electric field, the MGCN foam emitter showed much low turn-on field of 1.42 V μm^{-1} and threshold field of 2.18 V μm^{-1} (electric field needed to produce a current density of 1.0 mA cm^{-2}). These field emission characteristics are superior to those of graphene emitters previously reported [140, 141, 151]. The superb field emission performance of MGCN foam emitter is attributed to numerous sharp-edges of rGO platelets at which the electric field intensity is locally enhanced, and correspondingly, electrons can be readily emitted from the edges. For this reason, the MGCN foam emitter shows significantly improved field emission performance compared to the MGCN film emitter.

The MGCN foam formed on a Cu plate (*i.e.*, planar-type emitter) also exhibited excellent field emission performance with a low turn-on electric field of 1.06 V μm^{-1} and threshold field of 1.42 V μm^{-1} (Figure 4-14).

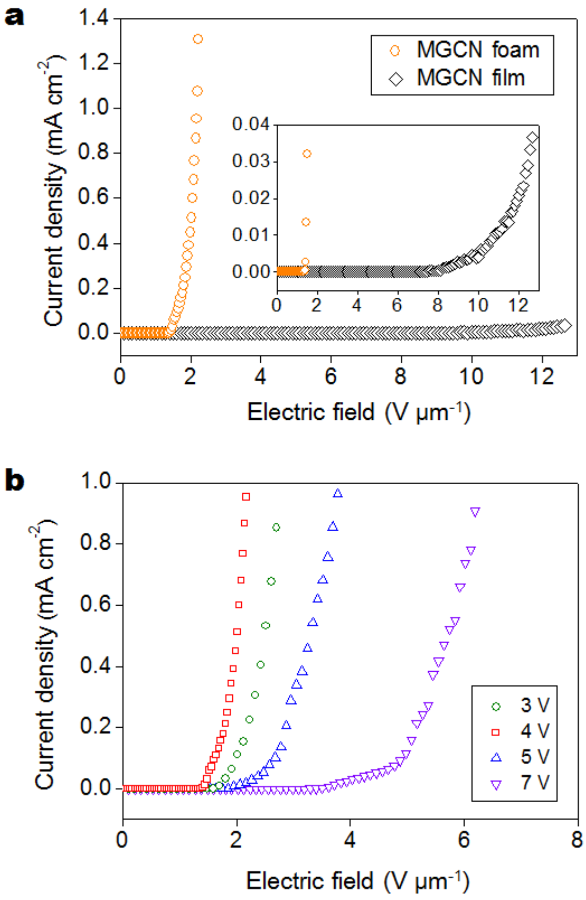

Figure 4-13. (a) Current-voltage (*I-V)* characteristics of MGCN foam and film emitters in a vacuum chamber at a base pressure of 3.0×10^{-7} Torr. (b) Current-voltage *(I-V)* characteristics of MGCN foam emitters fabricated by different applied voltages.

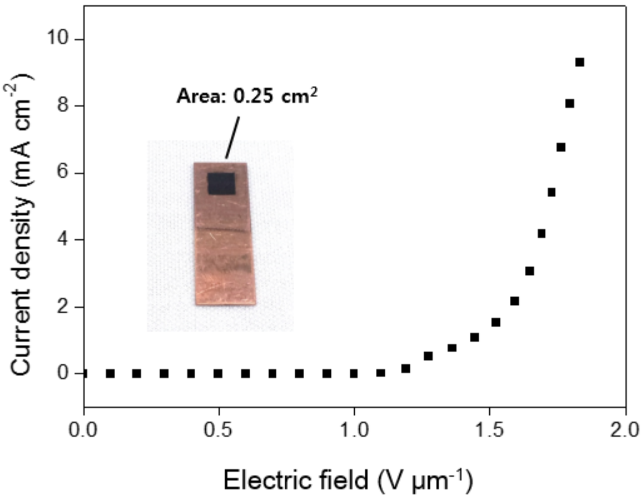

Figure 4-14. Current-voltage (*I-V)* characteristics of planar MGCN emitter in a vacuum chamber at a base pressure of 3.0×10^{-7} Torr.

4.3.3 Fowler-Nordheim curve

The Fowler–Nordheim (F–N) equation is useful to analyze field emission performance by correlating an applied electric field with the output emission current density, expressed as follows [161].

$$J = a\emptyset^{-1}E^{2}\beta^{2}\exp\left(-\frac{b\emptyset^{3/2}}{\beta E}\right) \tag{4-2}$$

where $\emptyset$ is the work function of emitting material, *J* is the current density, *E* is the local electric field, and *β* is the local electric field enhancement factor. *a* and *b* are constants with 1.54 × 10^{-6} A eV V^{-2} and 6.83 × 10^{9} $eV^{-3/2}$ V m^{-1}, respectively. The field enhancement factor (*β*) is typically used to investigate the geometric effect of field emitters, which is given by:

$$\beta = -\frac{b\emptyset^{3/2}}{m} \tag{4-3}$$

where $\emptyset$ is the work function of emitting material, *b* is constant (6.83 × 10^{9} $eV^{-3/2}$ V m^{-1}), and *m* is the slope of the F-N curve.

Figure 4-15 shows the F-N curves of the MGCN foam and film emitters, and the slope of the curve represents the field enhancement factor. The field enhancement factor of 1450 for the MGCN foam emitter is higher than that of 1220 for the MGCN film emitter. It is obvious that numerous sharp-edges of rGO in the foam are attributed to this improvement.

Interestingly, two distinct behaviors regarding the F–N curve of MGCN foam emitter were observed. The field enhancement factor of the MGCN emitter is almost linear in a low field region; however, it turns nonlinear in the region of the high electrical field, exhibiting much higher field enhancement factor of 7140. The alignment of rGO platelets in the foam toward the direction of applied electric field might be responsible for enhancing the field enhancement factor, which is caused by electric polarization of graphene [162].

The y-intercept in F-N curve is directly related to actual emission area and work function of an emitter. Actual emission area (A) is given from the F-N equation as follows [163, 164]:

$$A \propto \left(\frac{J}{E^2}\right)\left(\frac{\emptyset}{a}\right)\exp\left(\frac{b\emptyset^{3/2}}{\beta E}\right) \tag{4-4}$$

A high value of y-intercept in F-N curve of the MGCN foam indicates the foam emitter has larger actual emission area compared to the film emitter. By extrapolating the F-N curve, the actual emission area of MGCN foam was estimated as 1700 times larger, compared to the MGCN film.

The MGCN foam formed on a Cu plate also exhibited high enhancement factor of 7090 with nonlinearity in high electric field region (Figure 4-16).

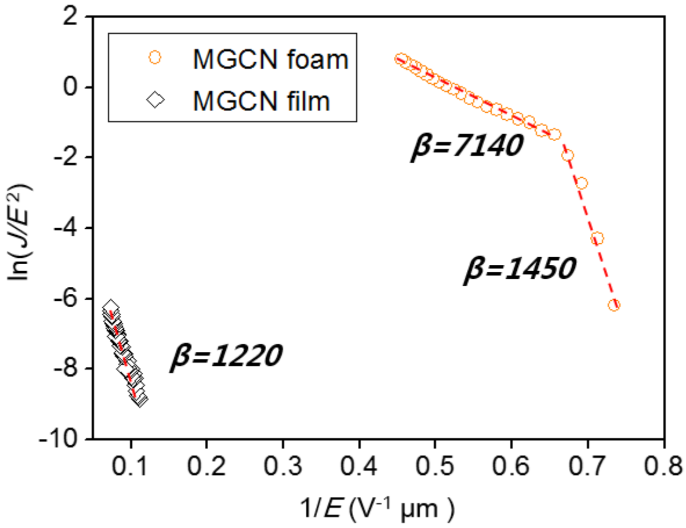

Figure 4-15. Fowler–Nordheim (F–N) curves of cylindrical MGCN foam and film emitters.

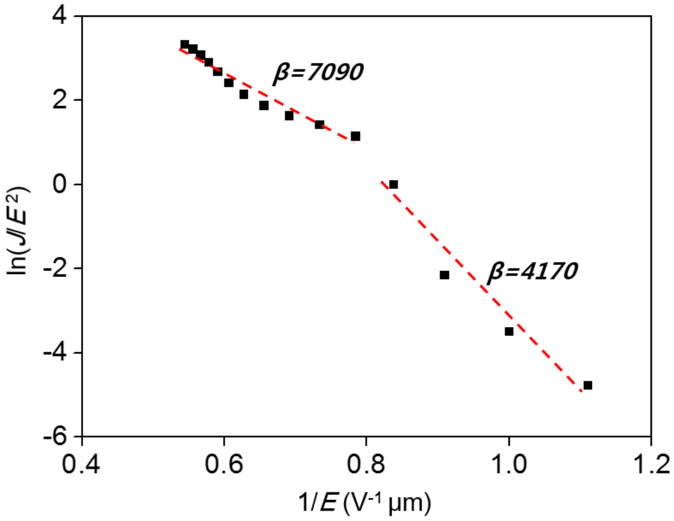

Figure 4-16. Fowler–Nordheim (F–N) curve of MGCN planar emitter.

4.3.4 Long-term stability

The stability of field emission is of practical interest at high current since the emitter can easily be damaged due to evaporation of graphene by Joule heating and ion bombardment of residual gases [165, 166]. A long-term emission stability test was conducted in which the current density of the emitter was maintained constant at the level corresponding to 1.2 and 8.1 mA cm^{-2} for 12 hours. As shown in Figure 4-17, it is apparent that the current is stably collected with little fluctuation, showing robustness of the graphene foam emitter. The planar MGCN emitter also exhibited long-term emission stability with a current density of 9.2 mA cm^{-2} for 22 hours (Figure 4-18).

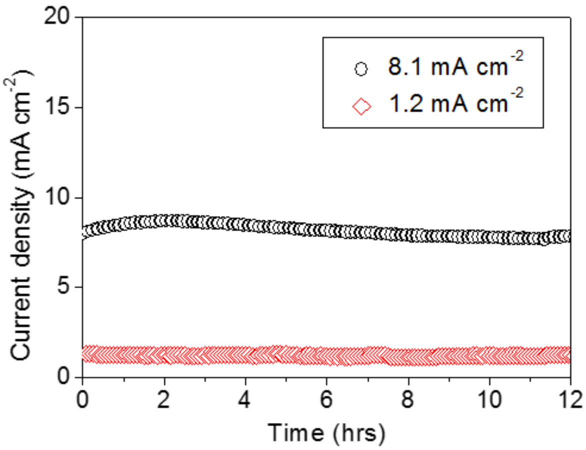

Figure 4-17. A long-term emission stability test where the current density of the cylindrical foam emitter was maintained constant at the level corresponding to 1.2 and 8.1 mA cm^{-2} for 22 hours.

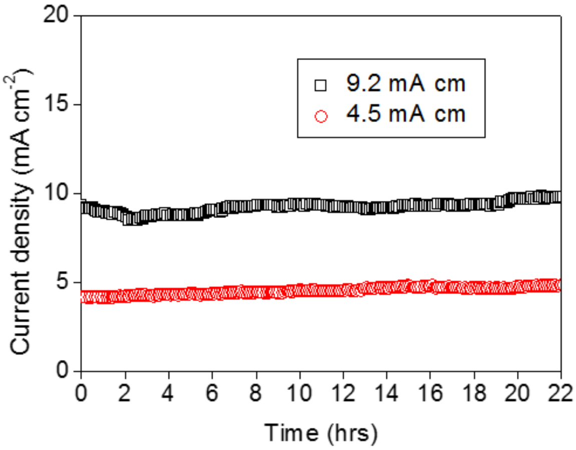

Figure 4-18. A long-term emission stability test where the current density of the planar foam emitter was maintained constant at the level corresponding to 4.5 and 9.2 mA cm^{-2} for 22 hours.

4.3.5 Comparison of field emission performance

The field emission performance of graphene emitters fabricated by various method, such as EPD [141], screen printing [150, 151], direct growth (CVD) [75, 140, 148, 167], and etc. [142, 154-156, 166, 168, 169], were compared (Figure 4-19). The emitter fabricated by IMA method shows excellent performance with a low turn-on field (1.06 V μm^{-1}) and threshold field (1.42 V μm^{-1}), which are better than those of previously reported graphene emitters.

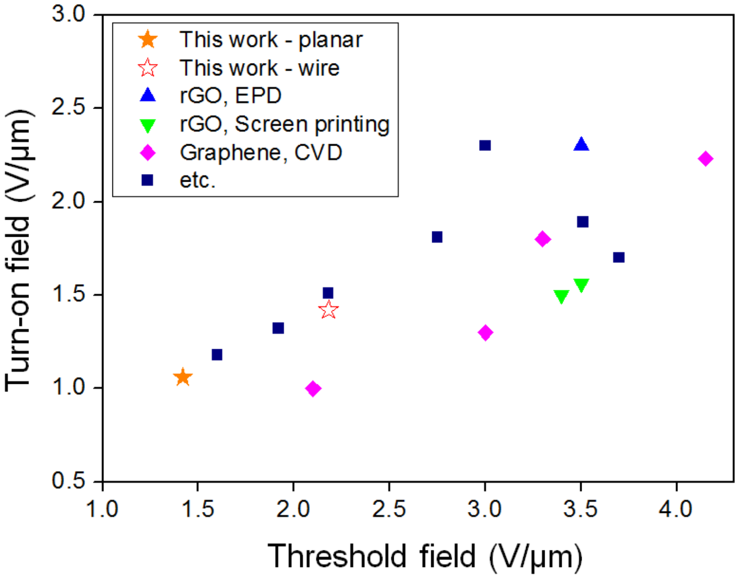

Figure 4-19. Field emission performance of graphene emitters fabricated by various methods.

Chapter 5. Expanded thermal convection

Rapid progress in electronic technology requires more efficient heat dissipation to avoid the degradation and failure of electronic devices. Effective thermal management in electronic devices is a crucial requirement for improving performance, reliability, and life expectancy of the devices. In this chapter, MGCN formed on copper block was utilized for effective heat dissipation through its expanded thermal convection. An optimized thickness of MGCN for heat dissipation was determined by modulating parameters of IMA process.

5.1 Heat dissipation

5.1.1 Heat generation in electronic devices

As the power density in electronic devices has been rapidly increasing, excess heat the devices generate is one of the major problems limiting the development of electronic industry. Figure 5-1(a) shows the number of transistors per microprocessor chip and their clock speeds for the past five decades [170]. To make the chip faster, transistors in the chip have to become smaller, thereby integrating more transistors in the chip. However, this approach began to fail in early 2000s due to excess heat the chip generates. As shown in the figure, manufacturers have stopped to increase clock speeds, which directly influence on chip performance, for the past decade to reduce heat generation.

For another example is light-emitting diode (LED) that occupies a considerable market share of light sources. Although it has the advantage over conventional light sources in terms of efficiency, waste heat still reaches to ~75% of input electrical energy. Furthermore, overheating of LED degrades its efficiency and life time as shown in Figure 5-1(b) [171, 172].

Degradation of performance by heat is also observed in most electronic devices and even rechargeable battery in portable devices. Effective thermal management in electronic devices is a crucial requirement for better performance and life expectancy of devices.

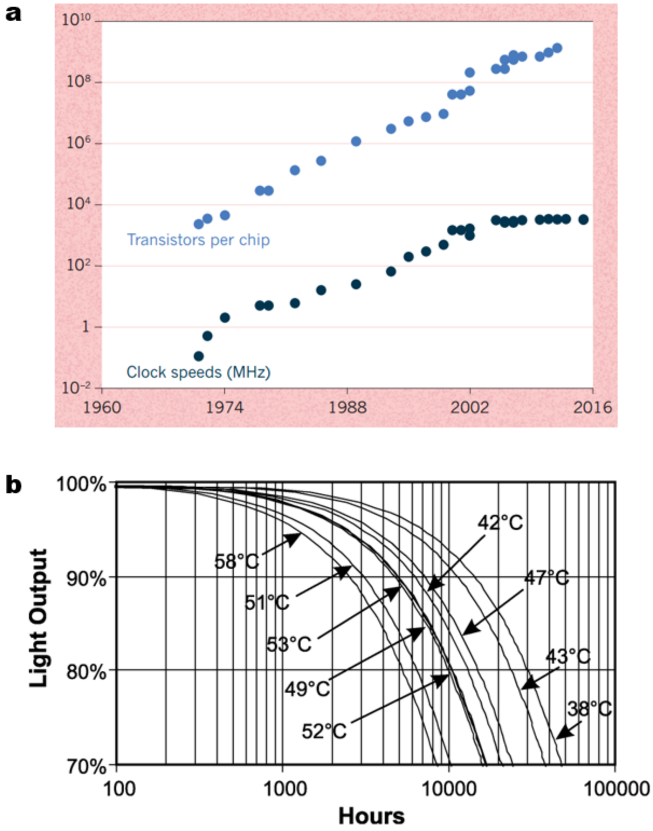

Figure 5-1. (a) The number of transistors per microprocessor chip and their clock speeds [170]. (b) Light output as a function of time for high-power LEDs operated at various ambient temperatures [172].

5.1.2 Heat transfer principle of heat sink

A heat sink transfers thermal energy from a device to a lower temperature air or fluid. Dominant heat transfers with a heat sink are occurred through conduction and convection.

Figure 5-2 shows the schematic of a heat sink. Fourier's law of heat conduction can be used for the conduction within a heat sink. This law is an empirical law based on observation, representing the relationship between temperature gradient and the rate of heat transferred by conduction. Equation 5-1 is a form simplified to a one-dimensional in the x-direction.

$$q_{cond} = -kA\frac{dT}{dx} \tag{5-1}$$

where q_{cond}, k, A, and T are heat transfer rate, thermal conductivity of heat sink materials, cross-sectional area normal to heat transfer direction, and temperature.

Thermal energy is transferred from the surface of heat sink to a low temperature fluid through convection. Thermal energy transferred by convection is proportional to the difference between surface temperature (T_{s}) and temperature of fluid (T_∞), known as Newton's law of cooling. The constant of proportionality is the heat transfer coefficient that is affected by material and shape of heat sink, flow rate of fluid. Equation 5-2 is a form simplified to a one-dimensional in the x-direction.

$$q_{conv} = hA(T_{\mathrm{s}} - T_\infty) \tag{5-2}$$

where q_{conv}, h, A, T_{s}, and T_{∞} are heat transfer rate, heat transfer coefficient, cross-sectional area normal to heat transfer direction, the surface temperature of heat sink, and the temperature of environmental fluid.

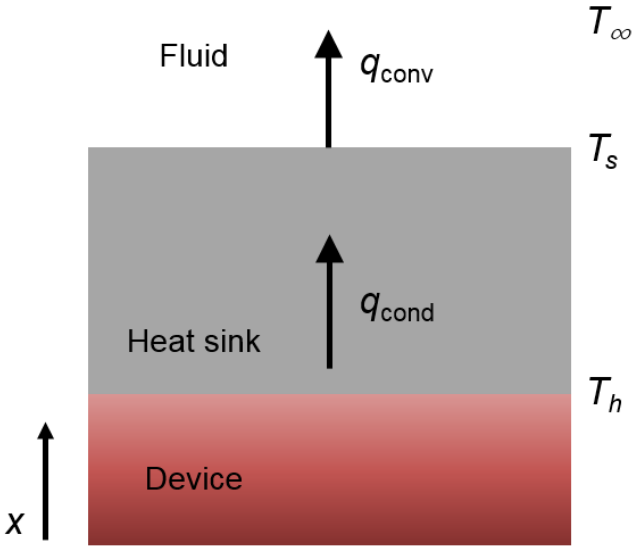

Figure 5-2. Schematic of a heat sink placed above an electronic device.

5.1.3 Recent research on heat dissipation using carbon nanomaterials

Most research on heat dissipation using carbon nanomaterials have been focused on thermal interface material (TIM) [173, 174], heat spreader [175-177], and high thermal conductive composite [178, 179]. Especially, carbon nanotube and graphene have attracted great attention due to their superior thermal conductivity and large surface area.

Thermal interface materials that use graphene as a filler showed high thermal conductivity enhancement (over 2000%) with small fraction of filler [173].

Few-layer graphene heat spreader can reduce the temperature of high-power gallium nitride transistor by ~20 ^{o}C as shown in Figure 5-3(a) [175]. Carbon nanoring/graphene hybrid paper also showed an excellent heat spreading ability, reducing the working temperature of LED device by 6.6 °C [176].

Some groups reported heat sinks made from vertically aligned carbon nanotube as shown in Figure 5-3(b) [180-183]. The large surface area and high aspect ratio of carbon nanotube led to substantial increases in heat transfer to air or liquid, thereby reducing the temperature of devices. However, a heat sink made from graphene has not been reported due to the difficulty in standing graphene sheets vertically despite its large surface area and high thermal conductivity.

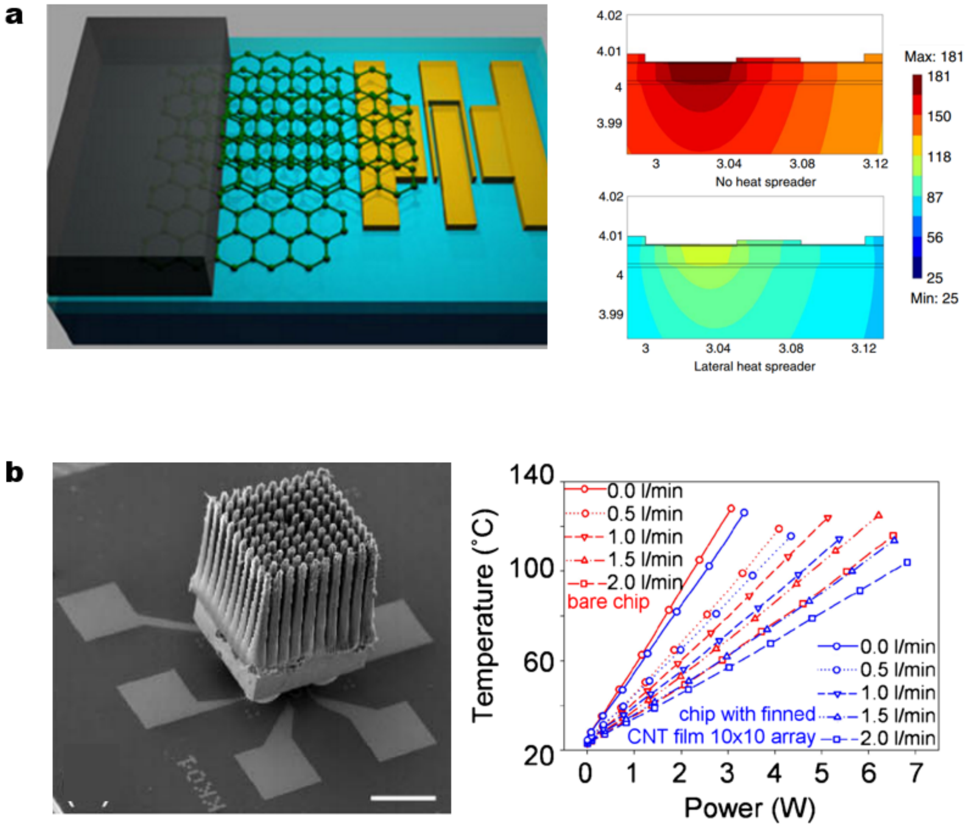

Figure 5-3. (a) Left: Schematic of a few layer graphene heat spreader attached to a gallium nitride transistor. Right: Simulated temperature distribution in the transistor [175]. (b) Left: SEM image of a carbon nanotube heat sink. Scale bar is 500 nm. Right: Chip temperatures measured for chip-on-substrate and the corresponding carbon nanotube heat sink under various heating powers and N_2 flow rates [183].

5.2 Fabrication of MGCN heat sink

5.2.1 MGCN formed on copper block

GO powder was prepared with the same method mentioned in section 2.2.1. Oxidation time was fixed at 3 hours to preserve intrinsic thermal conductivity of graphene. GO powder was dispersed in deionized water with a controlled concentration of 1-3 mg mL^{-1} by sonication. After the preparation of GO suspension, a copper block and a copper foil were immersed in the suspension as an anode and a cathode. The dimension of the block is 35 mm × 28 mm × 3 mm. The backside of the block was passivated by polyimide (Kapton) tape to retain the intact surface of the backside that will be contacted with a heat source.

A dc voltage of 5 V was applied between the anode and cathode for 5-60 sec to control the thickness of MGCN. The inter-electrode spacing was fixed as 1 cm. After completing IMA process, MGCN heat sink was dried through rapid vacuum drying process at a chamber pressure of 1.0×10^{-2} Torr. Finally, the heat sink was annealed at 200 ^{o}C under Ar gas flow for 3 hours to remove oxygen functional groups, thereby enhancing the thermal conductivity of MGCN heat sink.

MGCN was formed on the entire area of the block without any voids and cracks as shown in Figure 5-4(a). MGCN had porous 3-D graphene network providing large surface area for enhanced thermal convection (Figure 5-4(b)). Right image of Figure 5-4(b) shows a sample of which the part was detached by an adhesive tape to observe the boundary between MGCN and the block. Graphene sheets were tightly bounded to the surface of the block.

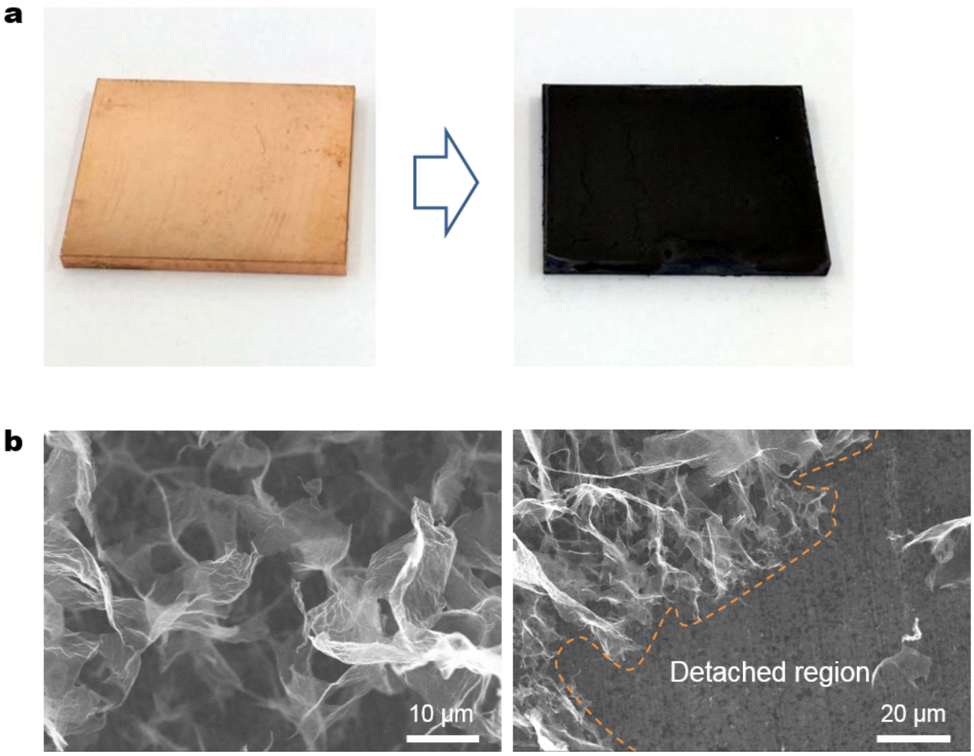

Figure 5-4. (a) Optical images of a copper block and MGCN formed on the block. (b) SEM images of MGCN formed on the block. MGCN in the region below dotted line of right image was detached by an adhesive tape for clear observation.

5.2.2 MGCN formed on aluminum block

Although copper has a superior thermal conductivity among commercial metals, aluminum is commonly used for base material of heat sinks due to its low cost. As discussed in section 2.2.3, aluminum is not appropriate for IMA process. Passivation layer of aluminum oxide on aluminum surface impedes anodic dissolution of aluminum ions.

One strategy to make MGCN on aluminum is to deposit thin copper layer on the surface of aluminum block as shown in Figure 5-5(a) and (b). A 500 nm thick copper layer was deposited on an aluminum block by thermal evaporation. This aluminum block was used as anode electrode in IMA process. As shown in Figure 5-5(c), MGCN was successfully formed on the aluminum block due to the copper layer deposited on the block. To clearly observe the effect of copper layer, the part of copper layer was detached by an adhesive tape, thereby exposing aluminum layer (Figure 5-5(d)). As shown in Figure 5-5(e), MGCN was formed on the region where copper layer was deposited. Although some graphene sheets were attached to aluminum through electrophoretic deposition, the quantity of graphene sheets attached on aluminum was too small to form a 3-D porous network.

The method introduced in this section can be applicable to other metals or non-conductive materials for various applications.

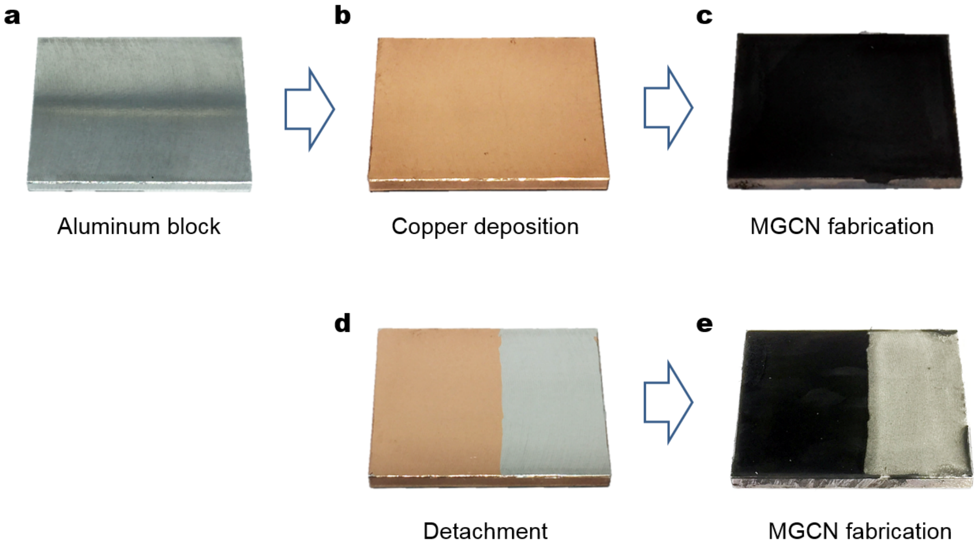

Figure 5-5. Schematic of MGCN fabrication using aluminum block. Optical images of (a) an aluminum block, (b) copper layer deposited on the block, (c) MGCN formed on copper layer/aluminum block, (d) copper layer deposited on the part of the aluminum block, (e) MGCN formed on the block in (d).

5.3 Heat dissipation performance

5.3.1 Experimental setup

Figure 5-6 shows an experimental setup for measuring heat dissipation performance of heat sinks. A constant temperature and humidity chamber was used for all experiments to maintain the temperature and humidity of air. The temperature was 25 ^{o}C and the relative humidity was 30%.

A test jig consists of a plate heater, a copper holder, and a Teflon case shown in Figure 5-7. The copper holder was adopted for its high thermal conductivity and low contact thermal resistance with a copper block. Three holes in the holder and Teflon case are for the insertion of thermocouples. The holes were made just beneath the surface of the holder to measure the surface temperature of a heat sink.

A test was performed in at least 4 hours after placing a heat sink above the holder to stabilize the temperature and humidity inside the chamber. A dc voltage of 12 V was applied to the plate heater that generated heat corresponding to 6.72 W. The temperature of a heat sink was measured for 3 hours to perform a time-transient thermal analysis.

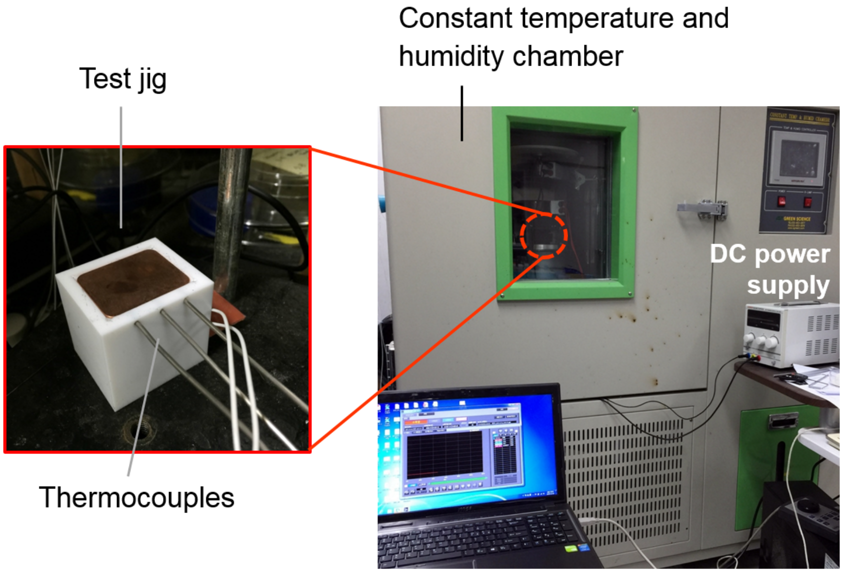

Figure 5-6. Experimental setup for measuring heat dissipation performance of heat sinks.

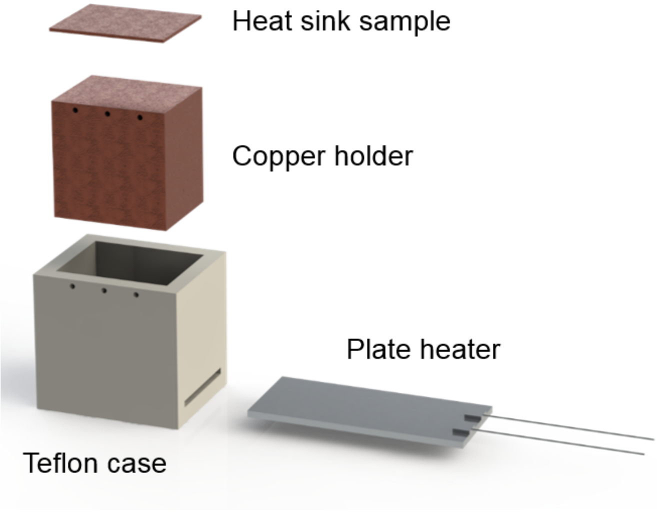

Figure 5-7. The disassembled schematic view of test jig.

5.3.2 Thermal convection coefficient

MGCN heat sinks made from 1 mg mL^{-1} GO solution (MGCN-1) showed superior heat dissipation performance as shown in Figure 5-8(a). The temperature of heat sink was decreased by 26% with MGCN-1. MGCN-1 heat sinks showed an optimized thickness of ~85 μm for heat dissipation. Initial improvement with increasing thickness is related to the increased surface area of MGCN. Little degradation with a thickness higher than 85 μm can be interpreted as the effect of excessive thick layer of MGCN which hinders convection flow.

Assuming that heat is dissipated only through heat sink, the rate of convection heat transfer equals to the rate of conduction heat transfer and heat generated by heater. Considering Equation 5-2, this is expressed as

$$q_{heater} = q_{cond} = q_{conv} = hA(T_s - T_\infty) \tag{5-3}$$

$$h = \frac{q_{heater}}{A(T_s - T_\infty)} \tag{5-4}$$

From Equation 5-4 and the data of Figure 5-8(b), the heat transfer coefficients of MGCN-1 heat sinks were calculated as shown in Figure 5-8(c). The coefficients were normalized to that of a copper block. The heat transfer coefficient of the copper block was increased by 36% with MGCN-1.

Figure 5-9 show the heat dissipation performances of MGCN-2 and MGCN-3 that were made from 2 and 3 mg mL^{-1} GO solution, respectively. MGCN-2 and MGCN-3 also brought out outstanding improvement in temperature drop of heat sink and heat transfer coefficients.

MGCN formed on Al (MGCN-Al) also showed excellent improvement in heat dissipation as shown in Figure 5-10. The heat transfer coefficient of MGCN-Al was 36% higher than that of copper block.

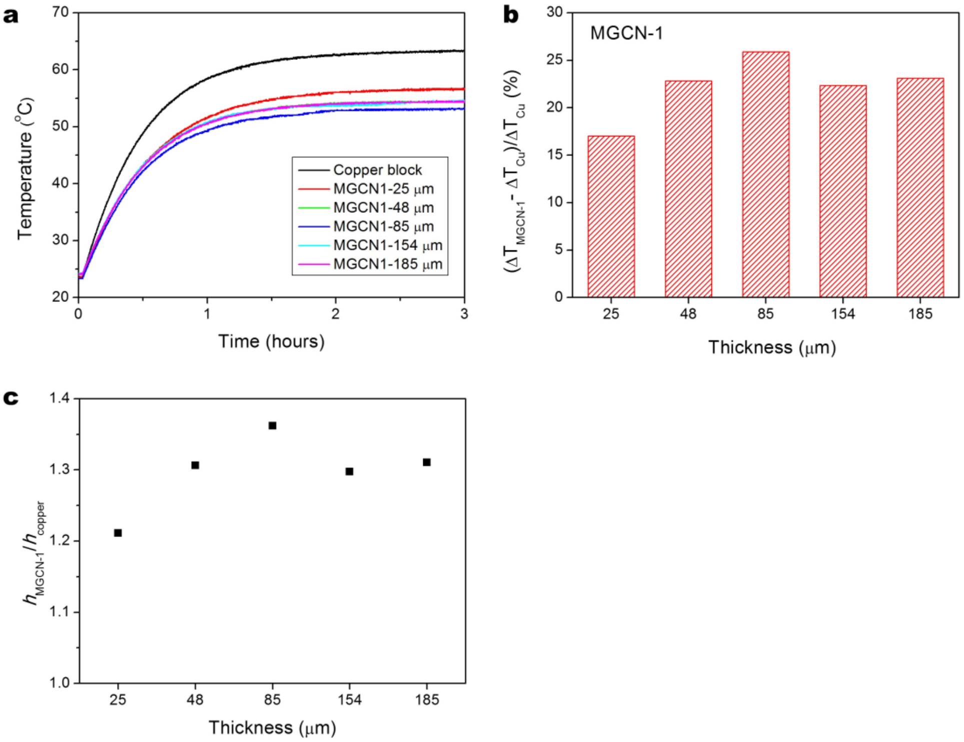

Figure 5-8. (a) Temperatures of copper block and MGCN-1 heat sinks as a function of time. MGCN-1 heat sinks was made from 1 mg mL^{-1} GO solution. (b) The percentage of temperature drop by MGCN-1 heat sinks. (c) Heat transfer coefficients of MGCN-1 heat sinks normalized to that of copper block.

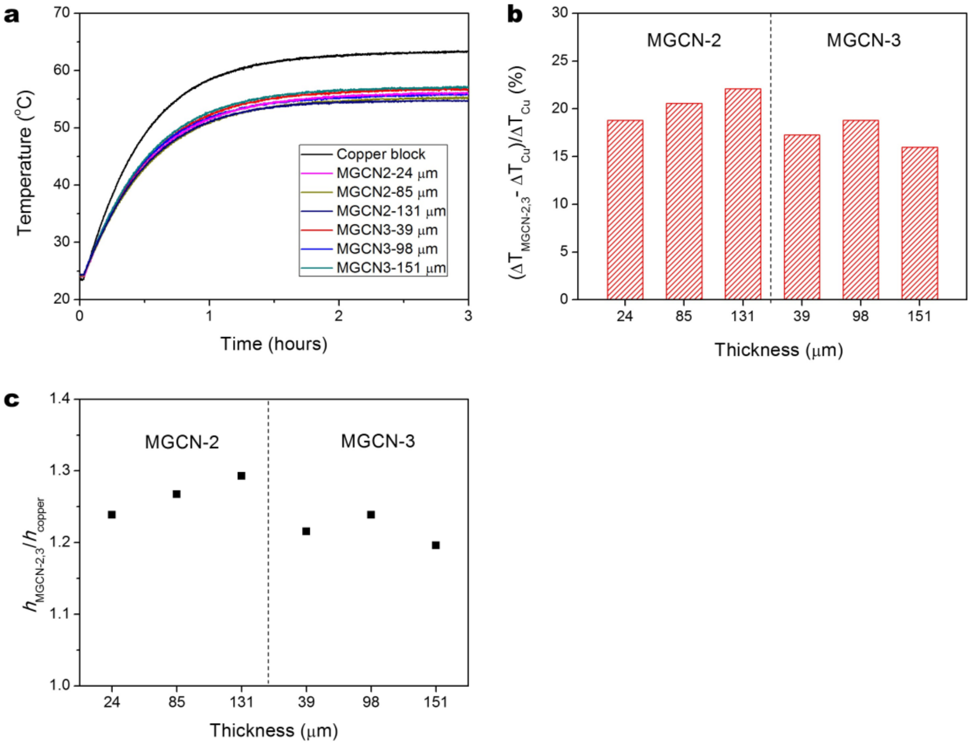

Figure 5-9. (a) Temperatures of heat sinks as a function of time for copper, MGCN-2, and MGCN-3 heat sinks. MGCN-2 and MGCN-3 heat sinks was made from 2 and 3 mg mL^{-1} GO solution, respectively. (b) The percentage of temperature drop by MGCN-2 and MGCN-3 heat sinks. (c) Heat transfer coefficients of MGCN-2 and MGCN-3 heat sinks normalized to that of copper block.

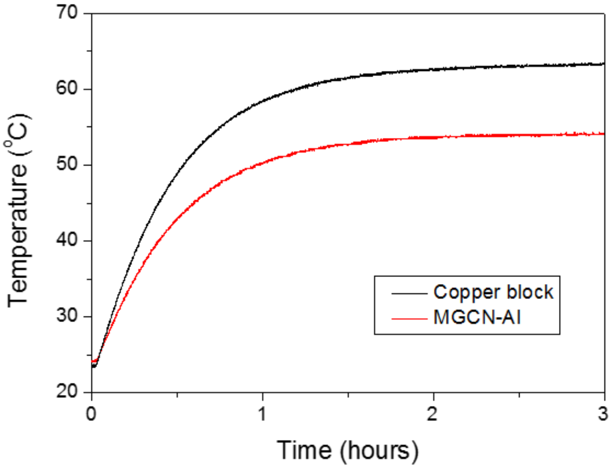

Figure 5-10. (a) Temperatures of heat sinks as a function of time for copper and MGCN-Al heat sinks.

Chapter 6. Conclusions

In this thesis, an ion-mediated assembly (IMA) method was developed for a substrate-initiated assembly of 3-D graphene structures. In particular, metal ions dissolved from a metal substrate by an applied voltage brought about the formation of 3-D coordination network of metal and graphene oxide (GO). This metal-graphene oxide coordination network (MGCN) was successfully fabricated on a plate, rod, wire, foil, or even mesh substrate, providing flexibility to meet the needs of applications.

The shape and dimension of MGCN was precisely controlled by modulating the process parameters of IMA including applied voltage, concentration of GO solution, and process time. Functional guests, such as MnO_2, SnO_2, and TiO_2, were decorated on MGCN by simply mixing the guests in GO solution in advance of IMA process. Copper nanoparticle decorated MGCN was also obtained through thermal annealing in Ar/H_2 atmosphere.

The interior microstructure of MGCN was investigated by scanning electron microscope. MGCN has well interconnected 3-D porous network where pore walls are continuously cross-linked by the partial overlapping and coalescing of GO sheets. The pore sizes are in the range of several micrometers to tens of micrometers. X-ray photoelectron spectroscopy and Fourier transform infrared spectroscopy analysis were performed to investigate the chemical structure of MGCN. C-O-C bond and C=O bond on GO were considerably removed by the coordination between metal ions and oxygen functional groups of GO. The atomic concentration of metal (copper) which determines the pore size of MGCN ranged from 3.7 to 5.3% depending on the process parameters. The density, surface area, and porosity of MGCN aerogel was estimated to be 12.3 mg cm^{-3}, 144.5 m^2 g^{-1}, and 90.8%, respectively.

The characteristic features of MGCN, including selective capillarity, countless sharp edges, and expanded thermal convection, were investigated and utilized for practical applications.

MGCN showed outstanding selective capillarity. MGCN rapidly absorbed oil by capillary force while it completely repelled water. MGCN formed on copper mesh was used for an oil permeable filter to separate oil and water. A proto-type graphene vessel, the hull of which was made of MGCN, was fabricated to selectively collect oil. Capillarity and gravity worked together to fill this proto-type graphene vessel with the spilled oil at a rate that is higher than 20,000 liters per square meter per hour (LMH) with oil purity better than 99.9%, and allowed the vessel to withstand a water head of 0.5 m. The vessel also had a superb chemical stability and recyclability. An expanded oil contact area, considerably greater than the thickness of the oil layer, formed at the MGCN interface upon contact with the spilled oil. This expanded contact area did not change much even when the oil layer thinned out. As a result, the high oil collection rate was maintained throughout the recovery of spilled oil.

Countless sharp edges of MGCN were favorable for field emission. With numerous countless sharp graphene edges, a MGCN foam emitter showed outstanding field emission properties, such as a low turn-on electric field of 1.06 V μm^{-1}, threshold field of 1.42 V μm^{-1}, and long-term emission stability with a current density of 9.2 mA cm^{-2} for 22 hours. The field enhancement factor of MGCN foam emitter (7140) was much higher than that of MGCN film emitter (1220) which has no sharp edge.

The field emission performance of MGCN emitter was superior to those of graphene emitters previously reported. MGCN emitter could be available to various geometries of substrates such as rod, plate, and flexible wire. By employing the flexibility of the electrode, the emitter is applicable to luminescent lighting tube and also provides a winding structure that requires high-current electron sources.

MGCN was also efficient for dissipating heat due to its high porosity and large surface area which promoted high rate of thermal convection. MGCN heat sink decreased the temperature of a device by 26%. Heat transfer coefficient of MGCN was 36% higher than that of copper block used for the substrate of MGCN. IMA process was applied to an aluminum block that is usually used for heat sink material but not suitable for the process. Deposition of thin copper layer on the block enabled the formation of MGCN on aluminum. MGCN formed on the aluminum block also showed outstanding heat dissipation performance.

Bibliography

[1] A. S. Mayorov, R. V. Gorbachev, S. V. Morozov, L. Britnell, R. Jalil, L. A. Ponomarenko, P. Blake, K. S. Novoselov, K. Watanabe, T. Taniguchi, A. K. Geim, Micrometer-Scale Ballistic Transport in Encapsulated Graphene at Room Temperature. *Nano Lett.* **11**, 2396 (2011).

[2] C. Lee, X. Wei, J. W. Kysar, J. Hone, Measurement of the Elastic Properties and Intrinsic Strength of Monolayer Graphene. *Science* **321**, 385 (2008).

[3] A. A. Balandin, Thermal properties of graphene and nanostructured carbon materials. *Nature Mater.* **10**, 569 (2011).

[4] W. Huang, G. Wang, F. Gao, Z. Qiao, G. Wang, L. Tao, M. Chen, F. Yu, H. Yang, L. Sun, Power generation from water flowing through three-dimensional graphene foam. *Nanoscale* **6**, 3921 (2014).

[5] W. Huang, G. Wang, F. Gao, Z. Qiao, G. Wang, M. Chen, Y. Deng, L. Tao, Y. Zhao, X. Fan, L. Sun, Energy Harvesting from the Mixture of Water and Ethanol Flowing through Three-Dimensional Graphene Foam. *J. Phys. Chem. C* **118**, 8783 (2014).

[6] M. F. El-Kady, V. Strong, S. Dubin, R. B. Kaner, Laser Scribing of High-Performance and Flexible Graphene-Based Electrochemical Capacitors. *Science* **335**, 1326 (2012).

[7] Y. Xu, K. Sheng, C. Li, G. Shi, Self-Assembled Graphene Hydrogel via a One-Step Hydrothermal Process. *ACS Nano* **4**, 4324 (2010).

[8] W. Chen, S. Li, C. Chen, L. Yan, Self-Assembly and Embedding of Nanoparticles by In Situ Reduced Graphene for Preparation of a 3D Graphene/Nanoparticle Aerogel. *Adv. Mater.* **23**, 5679 (2011).

[9] X. Cao, Y. Shi, W. Shi, X. Rui, Q. Yan, J. Kong, H. Zhang, Preparation of MoS2-Coated Three-Dimensional Graphene Networks for High-

Performance Anode Material in Lithium-Ion Batteries. *Small* **9**, 3433 (2013).

[10] Z. Chen, W. Ren, L. Gao, B. Liu, S. Pei, H.-M. Cheng, Three-dimensional flexible and conductive interconnected graphene networks grown by chemical vapour deposition. *Nature Mater.* **10**, 424 (2011).

[11] Y. Yao, X. Chen, H. Guo, Z. Wu, X. Li, Humidity sensing behaviors of graphene oxide-silicon bi-layer flexible structure. *Sens. Actuators, B* **161**, 1053 (2012).

[12] N. Li, Q. Zhang, S. Gao, Q. Song, R. Huang, L. Wang, L. Liu, J. Dai, M. Tang, G. Cheng, Three-dimensional graphene foam as a biocompatible and conductive scaffold for neural stem cells. *Sci. Rep.* **3**, 1604 (2013).

[13] H. Bi, X. Xie, K. Yin, Y. Zhou, S. Wan, L. He, F. Xu, F. Banhart, L. Sun, R. S. Ruoff, Spongy Graphene as a Highly Efficient and Recyclable Sorbent for Oils and Organic Solvents. *Adv. Funct. Mater.* **22**, 4421 (2012).

[14] H. Bi, X. Xie, K. Yin, Y. Zhou, S. Wan, R. S. Ruoff, L. Sun, Highly enhanced performance of spongy graphene as an oil sorbent. *J. Mater. Chem. A* **2**, 1652 (2014).

[15] S. J. Yang, J. H. Kang, H. Jung, T. Kim, C. R. Park, Preparation of a freestanding, macroporous reduced graphene oxide film as an efficient and recyclable sorbent for oils and organic solvents. *J. Mater. Chem. A* **1**, 9427 (2013).

[16] Z. Niu, J. Chen, H. H. Hng, J. Ma, X. Chen, A Leavening Strategy to Prepare Reduced Graphene Oxide Foams. *Adv. Mater.* **24**, 4144 (2012).

[17] Y. Zhu, S. Murali, M. D. Stoller, K. J. Ganesh, W. Cai, P. J. Ferreira, A. Pirkle, R. M. Wallace, K. A. Cychosz, M. Thommes, D. Su, E. A. Stach, R. S. Ruoff, Carbon-Based Supercapacitors Produced by Activation of Graphene. *Science* **332**, 1537 (2011).

[18] P. K. Sahoo, R. Aepuru, H. S. Panda, D. Bahadur, Ice-templated synthesis

of multifunctional three dimensional graphene/noble metal nanocomposites and their mechanical, electrical, catalytic, and electromagnetic shielding properties. *Sci. Rep.* **5**, 17726 (2015).

[19] C. Wu, X. Huang, G. Wang, L. Lv, G. Chen, G. Li, P. Jiang, Highly Conductive Nanocomposites with Three-Dimensional, Compactly Interconnected Graphene Networks via a Self-Assembly Process. *Adv. Funct. Mater.* **23**, 506 (2013).

[20] C.-M. Chen, Q. Zhang, C.-H. Huang, X.-C. Zhao, B.-S. Zhang, Q.-Q. Kong, M.-Z. Wang, Y.-G. Yang, R. Cai, D. Sheng Su, Macroporous 'bubble' graphene film via template-directed ordered-assembly for high rate supercapacitors. *Chem. Commun.* **48**, 7149 (2012).

[21] Y. Yao, X. Chen, H. Guo, Z. Wu, Graphene oxide thin film coated quartz crystal microbalance for humidity detection. *Appl. Surf. Sci.* **257**, 7778 (2011).

[22] M. A. Worsley, T. Y. Olson, J. R. I. Lee, T. M. Willey, M. H. Nielsen, S. K. Roberts, P. J. Pauzauskie, J. Biener, J. H. Satcher, T. F. Baumann, High Surface Area, sp2-Cross-Linked Three-Dimensional Graphene Monoliths. *J. Phys. Chem. Lett.* **2**, 921 (2011).

[23] M. A. Worsley, P. J. Pauzauskie, T. Y. Olson, J. Biener, J. H. Satcher, T. F. Baumann, Synthesis of Graphene Aerogel with High Electrical Conductivity. *J. Am. Chem. Soc.* **132**, 14067 (2010).

[24] P. Chen, J.-J. Yang, S.-S. Li, Z. Wang, T.-Y. Xiao, Y.-H. Qian, S.-H. Yu, Hydrothermal synthesis of macroscopic nitrogen-doped graphene hydrogels for ultrafast supercapacitor. *Nano Energy* **2**, 249 (2013).

[25] W. Zhang, J. Zhu, H. Ang, Y. Zeng, N. Xiao, Y. Gao, W. Liu, H. H. Hng, Q. Yan, Binder-free graphene foams for O2 electrodes of Li-O2 batteries. *Nanoscale* **5**, 9651 (2013).

[26] C. Liu, R. Younesi, C.-W. Tai, M. Valvo, K. Edstrom, T. Gustafsson, J. Zhu,

3-D binder-free graphene foam as a cathode for high capacity Li-O2 batteries. *J. Mater. Chem. A*, (2016).

[27] A. K. Geim, K. S. Novoselov, The rise of graphene. *Nature Mater.* **6**, 183 (2007).

[28] Y. W. Zhu, S. Murali, W. W. Cai, X. S. Li, J. W. Suk, J. R. Potts, R. S. Ruoff, Graphene and Graphene Oxide: Synthesis, Properties, and Applications. *Adv. Mater.* **22**, 3906 (2010).

[29] D. R. Dreyer, S. Park, C. W. Bielawski, R. S. Ruoff, The chemistry of graphene oxide. *Chem. Soc. Rev.* **39**, 228 (2010).

[30] K. S. Novoselov, V. I. Fal'ko, L. Colombo, P. R. Gellert, M. G. Schwab, K. Kim, A roadmap for graphene. *Nature* **490**, 192 (2012).

[31] J. Zhang, H. Yang, G. Shen, P. Cheng, J. Zhang, S. Guo, Reduction of graphene oxide vial-ascorbic acid. *Chem. Commun.* **46**, 1112 (2010).

[32] C. Gómez-Navarro, J. C. Meyer, R. S. Sundaram, A. Chuvilin, S. Kurasch, M. Burghard, K. Kern, U. Kaiser, Atomic Structure of Reduced Graphene Oxide. *Nano Lett.* **10**, 1144 (2010).

[33] K. Erickson, R. Erni, Z. Lee, N. Alem, W. Gannett, A. Zettl, Determination of the Local Chemical Structure of Graphene Oxide and Reduced Graphene Oxide. *Adv. Mater.* **22**, 4467 (2010).

[34] J. I. Paredes, S. Villar-Rodil, P. Solís-Fernández, A. Martínez-Alonso, J. M. D. Tascón, Atomic Force and Scanning Tunneling Microscopy Imaging of Graphene Nanosheets Derived from Graphite Oxide. *Langmuir* **25**, 5957 (2009).

[35] C. Gómez-Navarro, R. T. Weitz, A. M. Bittner, M. Scolari, A. Mews, M. Burghard, K. Kern, Electronic Transport Properties of Individual Chemically Reduced Graphene Oxide Sheets. *Nano Lett.* **7**, 3499 (2007).

[36] K. N. Kudin, B. Ozbas, H. C. Schniepp, R. K. Prud'homme, I. A. Aksay, R. Car, Raman Spectra of Graphite Oxide and Functionalized Graphene

Sheets. *Nano Lett.* **8**, 36 (2008).

[37] G. Eda, G. Fanchini, M. Chhowalla, Large-area ultrathin films of reduced graphene oxide as a transparent and flexible electronic material. *Nature Nanotech.* **3**, 270 (2008).

[38] D. R. Dreyer, A. D. Todd, C. W. Bielawski, Harnessing the chemistry of graphene oxide. *Chem. Soc. Rev.* **43**, 5288 (2014).

[39] W. Gao, L. B. Alemany, L. Ci, P. M. Ajayan, New insights into the structure and reduction of graphite oxide. *Nature Chem.* **1**, 403 (2009).

[40] W. Cai, R. D. Piner, F. J. Stadermann, S. Park, M. A. Shaibat, Y. Ishii, D. Yang, A. Velamakanni, S. J. An, M. Stoller, J. An, D. Chen, R. S. Ruoff, Synthesis and Solid-State NMR Structural Characterization of 13C-Labeled Graphite Oxide. *Science* **321**, 1815 (2008).

[41] Y. Si, E. T. Samulski, Synthesis of Water Soluble Graphene. *Nano Lett.* **8**, 1679 (2008).

[42] A. Bagri, C. Mattevi, M. Acik, Y. J. Chabal, M. Chhowalla, V. B. Shenoy, Structural evolution during the reduction of chemically derived graphene oxide. *Nature Chem.* **2**, 581 (2010).

[43] D. Yang, A. Velamakanni, G. Bozoklu, S. Park, M. Stoller, R. D. Piner, S. Stankovich, I. Jung, D. A. Field, C. A. Ventrice Jr, R. S. Ruoff, Chemical analysis of graphene oxide films after heat and chemical treatments by X-ray photoelectron and Micro-Raman spectroscopy. *Carbon* **47**, 145 (2009).

[44] N. Morimoto, T. Kubo, Y. Nishina, Tailoring the Oxygen Content of Graphite and Reduced Graphene Oxide for Specific Applications. *Sci. Rep.* **6**, 21715 (2016).

[45] T. Szabó, O. Berkesi, P. Forgó, K. Josepovits, Y. Sanakis, D. Petridis, I. Dékány, Evolution of Surface Functional Groups in a Series of Progressively Oxidized Graphite Oxides. *Chem. Mater.* **18**, 2740 (2006).

[46] S. Pei, H.-M. Cheng, The reduction of graphene oxide. *Carbon* **50**, 3210

(2012).

[47] W. S. Hummers, R. E. Offeman, Preparation of Graphitic Oxide. *J. Am. Chem. Soc.* **80**, 1339 (1958).

[48] N. I. Kovtyukhova, P. J. Ollivier, B. R. Martin, T. E. Mallouk, S. A. Chizhik, E. V. Buzaneva, A. D. Gorchinskiy, Layer-by-layer assembly of ultrathin composite films from micron-sized graphite oxide sheets and polycations. *Chem. Mater.* **11**, 771 (1999).

[49] M. Hirata, T. Gotou, S. Horiuchi, M. Fujiwara, M. Ohba, Thin-film particles of graphite oxide 1:: High-yield synthesis and flexibility of the particles. *Carbon* **42**, 2929 (2004).

[50] D. C. Marcano, D. V. Kosynkin, J. M. Berlin, A. Sinitskii, Z. Sun, A. Slesarev, L. B. Alemany, W. Lu, J. M. Tour, Improved Synthesis of Graphene Oxide. *ACS Nano* **4**, 4806 (2010).

[51] B. C. Brodie, On the Atomic Weight of Graphite. *Philos. Trans. R. Soc. London* **149**, 249 (1859).

[52] L. Staudenmaier, Verfahren zur Darstellung der Graphitsäure. *Ber. Dtsch. Chem. Ges.* **31**, 1481 (1898).

[53] U. Hofmann, E. König, Untersuchungen über Graphitoxyd. *Z. Anorg. Allg. Chem* **234**, 311 (1937).

[54] X. Wang, L. Zhi, K. Müllen, Transparent, Conductive Graphene Electrodes for Dye-Sensitized Solar Cells. *Nano Lett.* **8**, 323 (2008).

[55] C. Mattevi, G. Eda, S. Agnoli, S. Miller, K. A. Mkhoyan, O. Celik, D. Mastrogiovanni, G. Granozzi, E. Garfunkel, M. Chhowalla, Evolution of Electrical, Chemical, and Structural Properties of Transparent and Conducting Chemically Derived Graphene Thin Films. *Adv. Funct. Mater.* **19**, 2577 (2009).

[56] Y. Zhu, S. Murali, M. D. Stoller, A. Velamakanni, R. D. Piner, R. S. Ruoff, Microwave assisted exfoliation and reduction of graphite oxide for

ultracapacitors. *Carbon* **48**, 2118 (2010).

[57] L. J. Cote, R. Cruz-Silva, J. Huang, Flash Reduction and Patterning of Graphite Oxide and Its Polymer Composite. *J. Am. Chem. Soc.* **131**, 11027 (2009).

[58] D. Li, M. B. Muller, S. Gilje, R. B. Kaner, G. G. Wallace, Processable aqueous dispersions of graphene nanosheets. *Nature Nanotech.* **3**, 101 (2008).

[59] X. Qi, K.-Y. Pu, X. Zhou, H. Li, B. Liu, F. Boey, W. Huang, H. Zhang, Conjugated-Polyelectrolyte-Functionalized Reduced Graphene Oxide with Excellent Solubility and Stability in Polar Solvents. *Small* **6**, 663 (2010).

[60] H. Bi, K. Yin, X. Xie, Y. Zhou, N. Wan, F. Xu, F. Banhart, L. Sun, R. S. Ruoff, Low Temperature Casting of Graphene with High Compressive Strength. *Adv. Mater.* **24**, 5124 (2012).

[61] H. D. Pham, V. H. Pham, T. V. Cuong, T.-D. Nguyen-Phan, J. S. Chung, E. W. Shin, S. Kim, Synthesis of the chemically converted graphene xerogel with superior electrical conductivity. *Chem. Commun.* **47**, 9672 (2011).

[62] L. Zhang, G. Chen, M. N. Hedhili, H. Zhang, P. Wang, Three-dimensional assemblies of graphene prepared by a novel chemical reduction-induced self-assembly method. *Nanoscale* **4**, 7038 (2012).

[63] X. Cao, D. Qi, S. Yin, J. Bu, F. Li, C. F. Goh, S. Zhang, X. Chen, Ambient Fabrication of Large-Area Graphene Films via a Synchronous Reduction and Assembly Strategy. *Adv. Mater.* **25**, 2957 (2013).

[64] U. N. Maiti, J. Lim, K. E. Lee, W. J. Lee, S. O. Kim, Three-Dimensional Shape Engineered, Interfacial Gelation of Reduced Graphene Oxide for High Rate, Large Capacity Supercapacitors. *Adv. Mater.* **26**, 615 (2014).

[65] H. Bai, C. Li, X. Wang, G. Shi, A pH-sensitive graphene oxide composite hydrogel. *Chem. Commun.* **46**, 2376 (2010).

[66] H. Bai, C. Li, X. Wang, G. Shi, On the Gelation of Graphene Oxide. *J.*

Phys. Chem. C **115**, 5545 (2011).

[67] P. M. Sudeep, T. N. Narayanan, A. Ganesan, M. M. Shaijumon, H. Yang, S. Ozden, P. K. Patra, M. Pasquali, R. Vajtai, S. Ganguli, A. K. Roy, M. R. Anantharaman, P. M. Ajayan, Covalently Interconnected Three-Dimensional Graphene Oxide Solids. *ACS Nano* **7**, 7034 (2013).

[68] X. Jiang, Y. Ma, J. Li, Q. Fan, W. Huang, Self-Assembly of Reduced Graphene Oxide into Three-Dimensional Architecture by Divalent Ion Linkage. *J. Phys. Chem. C* **114**, 22462 (2010).

[69] H. Huang, P. Chen, X. Zhang, Y. Lu, W. Zhan, Edge-to-Edge Assembled Graphene Oxide Aerogels with Outstanding Mechanical Performance and Superhigh Chemical Activity. *Small* **9**, 1397 (2013).

[70] H. Huang, S. Lu, X. Zhang, Z. Shao, Glucono-[small delta]-lactone controlled assembly of graphene oxide hydrogels with selectively reversible gel-sol transition. *Soft Matter* **8**, 4609 (2012).

[71] S. Park, K.-S. Lee, G. Bozoklu, W. Cai, S. T. Nguyen, R. S. Ruoff, Graphene Oxide Papers Modified by Divalent Ions—Enhancing Mechanical Properties via Chemical Cross-Linking. *ACS Nano* **2**, 572 (2008).

[72] A. Ganguly, S. Sharma, P. Papakonstantinou, J. Hamilton, Probing the Thermal Deoxygenation of Graphene Oxide Using High-Resolution In Situ X-ray-Based Spectroscopies. *J. Phys. Chem. C* **115**, 17009 (2011).

[73] R. Peng-Gang, Y. Ding-Xiang, J. Xu, C. Tao, L. Zhong-Ming, Temperature dependence of graphene oxide reduced by hydrazine hydrate. *Nanotechnology* **22**, 055705 (2011).

[74] C. D. Zangmeister, Preparation and Evaluation of Graphite Oxide Reduced at 220 °C. *Chem. Mater.* **22**, 5625 (2010).

[75] J. L. Qi, X. Wang, W. T. Zheng, H. W. Tian, C. Q. Hu, Y. S. Peng, Ar plasma treatment on few layer graphene sheets for enhancing their field

emission properties. *J. Phys. D: Appl. Phys.* **43**, 055302 (2010).

[76] R. E. Parker, N. S. Isaacs, Mechanisms Of Epoxide Reactions. *Chem. Rev.* **59**, 737 (1959).

[77] K. Nakamoto, *Infrared and Raman Spectra of Inorganic and Coordination Compounds, Applications in Coordination, Organometallic, and Bioinorganic Chemistry*. (Wiley, 1997).

[78] G. Socrates, *Infrared and Raman Characteristic Group Frequencies: Tables and Charts*. (Wiley, 2004).

[79] C. Hu, X. Zhai, L. Liu, Y. Zhao, L. Jiang, L. Qu, Spontaneous Reduction and Assembly of Graphene oxide into Three-Dimensional Graphene Network on Arbitrary Conductive Substrates. *Sci. Rep.* **3**, (2013).

[80] S. J. An, Y. Zhu, S. H. Lee, M. D. Stoller, T. Emilsson, S. Park, A. Velamakanni, J. An, R. S. Ruoff, Thin Film Fabrication and Simultaneous Anodic Reduction of Deposited Graphene Oxide Platelets by Electrophoretic Deposition. *J. Phys. Chem. Lett.* **1**, 1259 (2010).

[81] L. Rossrucker, A. Samaniego, J.-P. Grote, A. M. Mingers, C. A. Laska, N. Birbilis, G. S. Frankel, K. J. J. Mayrhofer, The pH Dependence of Magnesium Dissolution and Hydrogen Evolution during Anodic Polarization. *J. Electrochem. Soc.* **162**, C333 (2015).

[82] G. Zhao, X. Ren, X. Gao, X. Tan, J. Li, C. Chen, Y. Huang, X. Wang, Removal of Pb(ii) ions from aqueous solutions on few-layered graphene oxide nanosheets. *Dalton Trans.* **40**, 10945 (2011).

[83] M. D. Lima, S. Fang, X. Lepró, C. Lewis, R. Ovalle-Robles, J. Carretero-González, E. Castillo-Martínez, M. E. Kozlov, J. Oh, N. Rawat, C. S. Haines, M. H. Haque, V. Aare, S. Stoughton, A. A. Zakhidov, R. H. Baughman, Biscrolling Nanotube Sheets and Functional Guests into Yarns. *Science* **331**, 51 (2011).

[84] G. He, C. J. Hart, X. Liang, A. Garsuch, L. F. Nazar, Stable Cycling of a

Scalable Graphene-Encapsulated Nanocomposite for Lithium–Sulfur Batteries. *ACS Appl. Mater. Inter.* **6**, 10917 (2014).

[85] H. Wang, Y. Yang, Y. Liang, J. T. Robinson, Y. Li, A. Jackson, Y. Cui, H. Dai, Graphene-Wrapped Sulfur Particles as a Rechargeable Lithium–Sulfur Battery Cathode Material with High Capacity and Cycling Stability. *Nano Lett.* **11**, 2644 (2011).

[86] Y. Sun, X. Hu, W. Luo, Y. Huang, Self-Assembled Hierarchical MoO2/Graphene Nanoarchitectures and Their Application as a High-Performance Anode Material for Lithium-Ion Batteries. *ACS Nano* **5**, 7100 (2011).

[87] C.-K. Wu, M. Yin, S. O'Brien, J. T. Koberstein, Quantitative Analysis of Copper Oxide Nanoparticle Composition and Structure by X-ray Photoelectron Spectroscopy. *Chem. Mater.* **18**, 6054 (2006).

[88] C. C. Chusuei, M. A. Brookshier, D. W. Goodman, Correlation of Relative X-ray Photoelectron Spectroscopy Shake-up Intensity with CuO Particle Size. *Langmuir* **15**, 2806 (1999).

[89] H. Bi, Z. Yin, X. Cao, X. Xie, C. Tan, X. Huang, B. Chen, F. Chen, Q. Yang, X. Bu, X. Lu, L. Sun, H. Zhang, Carbon Fiber Aerogel Made from Raw Cotton: A Novel, Efficient and Recyclable Sorbent for Oils and Organic Solvents. *Adv. Mater.* **25**, 5916 (2013).

[90] P. Montes-Navajas, N. G. Asenjo, R. Santamaría, R. Menéndez, A. Corma, H. García, Surface Area Measurement of Graphene Oxide in Aqueous Solutions. *Langmuir* **29**, 13443 (2013).

[91] T. J. Crone, M. Tolstoy, Magnitude of the 2010 Gulf of Mexico Oil Leak. *Science* **330**, 634 (2010).

[92] C. H. Peterson, S. D. Rice, J. W. Short, D. Esler, J. L. Bodkin, B. E. Ballachey, D. B. Irons, Long-Term Ecosystem Response to the Exxon Valdez Oil Spill. *Science* **302**, 2082 (2003).

[93] J. D. Kessler, D. L. Valentine, M. C. Redmond, M. Du, E. W. Chan, S. D. Mendes, E. W. Quiroz, C. J. Villanueva, S. S. Shusta, L. M. Werra, S. A. Yvon-Lewis, T. C. Weber, A Persistent Oxygen Anomaly Reveals the Fate of Spilled Methane in the Deep Gulf of Mexico. *Science* **331**, 312 (2011).

[94] *Technical information papers - Use of booms in oil pollution response*. (The International Tanker Owners Pollution Federation Limited, 2011).

[95] *Technical information papers - Use of skimmers in oil pollution response*. (The International Tanker Owners Pollution Federation Limited, 2011).

[96] *ITOPF Handbook 2016/17*. (The International Tanker Owners Pollution Federation Limited, 2016).

[97] D. D. Nguyen, N.-H. Tai, S.-B. Lee, W.-S. Kuo, Superhydrophobic and superoleophilic properties of graphene-based sponges fabricated using a facile dip coating method. *Energy Environ. Sci.* **5**, 7908 (2012).

[98] R. Zhang, Y. Cao, P. Li, X. Zang, P. Sun, K. Wang, M. Zhong, J. Wei, D. Wu, F. Kang, H. Zhu, Three-dimensional porous graphene sponges assembled with the combination of surfactant and freeze-drying. *Nano Res.* **7**, 1477 (2014).

[99] Y. Wu, N. Yi, L. Huang, T. Zhang, S. Fang, H. Chang, N. Li, J. Oh, J. A. Lee, M. Kozlov, A. C. Chipara, H. Terrones, P. Xiao, G. Long, Y. Huang, F. Zhang, L. Zhang, X. Lepró, C. Haines, M. D. Lima, N. P. Lopez, L. P. Rajukumar, A. L. Elias, S. Feng, S. J. Kim, N. T. Narayanan, P. M. Ajayan, M. Terrones, A. Aliev, P. Chu, Z. Zhang, R. H. Baughman, Y. Chen, Three-dimensionally bonded spongy graphene material with super compressive elasticity and near-zero Poisson’s ratio. *Nat. Commun.* **6**, 6141 (2015).

[100] X. Gui, Z. Zeng, Z. Lin, Q. Gan, R. Xiang, Y. Zhu, A. Cao, Z. Tang, Magnetic and Highly Recyclable Macroporous Carbon Nanotubes for Spilled Oil Sorption and Separation. *ACS Appl. Mater. Inter.* **5**, 5845 (2013).

[101] X. Gui, J. Wei, K. Wang, A. Cao, H. Zhu, Y. Jia, Q. Shu, D. Wu, Carbon Nanotube Sponges. *Adv. Mater.* **22**, 617 (2010).

[102] D. P. Hashim, N. T. Narayanan, J. M. Romo-Herrera, D. A. Cullen, M. G. Hahm, P. Lezzi, J. R. Suttle, D. Kelkhoff, E. Muñoz-Sandoval, S. Ganguli, A. K. Roy, D. J. Smith, R. Vajtai, B. G. Sumpter, V. Meunier, H. Terrones, M. Terrones, P. M. Ajayan, Covalently bonded three-dimensional carbon nanotube solids via boron induced nanojunctions. *Sci. Rep.* **2**, 363 (2012).

[103] C. Ruan, K. Ai, X. Li, L. Lu, A Superhydrophobic Sponge with Excellent Absorbency and Flame Retardancy. *Angew. Chem. Int. Ed.* **53**, 5556 (2014).

[104] Q. Zhu, Y. Chu, Z. Wang, N. Chen, L. Lin, F. Liu, Q. Pan, Robust superhydrophobic polyurethane sponge as a highly reusable oil-absorption material. *J. Mater. Chem. A* **1**, 5386 (2013).

[105] Z. Shi, W. Zhang, F. Zhang, X. Liu, D. Wang, J. Jin, L. Jiang, Ultrafast Separation of Emulsified Oil/Water Mixtures by Ultrathin Free-Standing Single-Walled Carbon Nanotube Network Films. *Adv. Mater.* **25**, 2422 (2013).

[106] J. Gu, P. Xiao, J. Chen, F. Liu, Y. Huang, G. Li, J. Zhang, T. Chen, Robust preparation of superhydrophobic polymer/carbon nanotube hybrid membranes for highly effective removal of oils and separation of water-in-oil emulsions. *J. Mater. Chem. A* **2**, 15268 (2014).

[107] L. Hu, S. Gao, X. Ding, D. Wang, J. Jiang, J. Jin, L. Jiang, Photothermal-Responsive Single-Walled Carbon Nanotube-Based Ultrathin Membranes for On/Off Switchable Separation of Oil-in-Water Nanoemulsions. *ACS Nano* **9**, 4835 (2015).

[108] M. Huang, Y. Si, X. Tang, Z. Zhu, B. Ding, L. Liu, G. Zheng, W. Luo, J. Yu, Gravity driven separation of emulsified oil-water mixtures utilizing in situ polymerized superhydrophobic and superoleophilic nanofibrous membranes. *J. Mater. Chem. A* **1**, 14071 (2013).

[109] M. Tao, L. Xue, F. Liu, L. Jiang, An Intelligent Superwetting PVDF Membrane Showing Switchable Transport Performance for Oil/Water Separation. *Adv. Mater.* **26**, 2943 (2014).

[110] Z. Xue, S. Wang, L. Lin, L. Chen, M. Liu, L. Feng, L. Jiang, A Novel Superhydrophilic and Underwater Superoleophobic Hydrogel-Coated Mesh for Oil/Water Separation. *Adv. Mater.* **23**, 4270 (2011).

[111] F. Zhang, W. B. Zhang, Z. Shi, D. Wang, J. Jin, L. Jiang, Nanowire-Haired Inorganic Membranes with Superhydrophilicity and Underwater Ultralow Adhesive Superoleophobicity for High-Efficiency Oil/Water Separation. *Adv. Mater.* **25**, 4192 (2013).

[112] L. Zhang, Y. Zhong, D. Cha, P. Wang, A self-cleaning underwater superoleophobic mesh for oil-water separation. *Sci. Rep.* **3**, 2326 (2013).

[113] Q. Wen, J. Di, L. Jiang, J. Yu, R. Xu, Zeolite-coated mesh film for efficient oil-water separation. *Chem. Sci.* **4**, 591 (2013).

[114] F. Wang, S. Lei, M. Xue, J. Ou, W. Li, In Situ Separation and Collection of Oil from Water Surface via a Novel Superoleophilic and Superhydrophobic Oil Containment Boom. *Langmuir* **30**, 1281 (2014).

[115] F. Wang, S. Lei, M. Xue, J. Ou, C. Li, W. Li, Superhydrophobic and Superoleophilic Miniature Device for the Collection of Oils from Water Surfaces. *J. Phys. Chem. C* **118**, 6344 (2014).

[116] D. A. Dikin, S. Stankovich, E. J. Zimney, R. D. Piner, G. H. B. Dommett, G. Evmenenko, S. T. Nguyen, R. S. Ruoff, Preparation and characterization of graphene oxide paper. *Nature* **448**, 457 (2007).

[117] S. Wang, Y. Zhang, N. Abidi, L. Cabrales, Wettability and Surface Free Energy of Graphene Films. *Langmuir* **25**, 11078 (2009).

[118] R. R. Nair, H. A. Wu, P. N. Jayaram, I. V. Grigorieva, A. K. Geim, Unimpeded Permeation of Water Through Helium-Leak–Tight Graphene-Based Membranes. *Science* **335**, 442 (2012).

[119] M. Hamdaoui, F. Fayala, S. B. Nasrallah, Dynamics of capillary rise in yarns: Influence of fiber and liquid characteristics. *J. Appl. Polym. Sci.* **104**, 3050 (2007).

[120] E. W. Washburn, The Dynamics of Capillary Flow. *Phys. Rev.* **17**, 273 (1921).

[121] X. Peng, J. Jin, Y. Nakamura, T. Ohno, I. Ichinose, Ultrafast permeation of water through protein-based membranes. *Nature Nanotech.* **4**, 353 (2009).

[122] R. W. Baker, *Membrane Technology and Applications*. (Wiley, 2012).

[123] G. S. Park, Y. H. Kim, H. Han, J. K. Han, J. Ahn, J. H. Son, W. Y. Park, Y. U. Jeong, *Convergence of Terahertz Sciences in Biomedical Systems*. (Springer Netherlands, 2012).

[124] B. A. Kakade, V. K. Pillai, D. J. Late, P. G. Chavan, F. J. Sheini, M. A. More, D. S. Joag, High current density, low threshold field emission from functionalized carbon nanotube bucky paper. *Appl. Phys. Lett.* **97**, 073102 (2010).

[125] R. B. Sharma, D. J. Late, D. S. Joag, A. Govindaraj, C. N. R. Rao, Field emission properties of boron and nitrogen doped carbon nanotubes. *Chem. Phys. Lett.* **428**, 102 (2006).

[126] L. Jeong Seok, K. Taewoo, K. Seul-Gi, C. Myung Rae, S. Dong Kyun, L. Minwoo, K. Seontae, K. Dae Weon, P. Gun-Sik, J. Dae Hong, P. Yun Daniel, Y. Ji-Beom, K. Tae June, K. Yong Hyup, High performance CNT point emitter with graphene interfacial layer. *Nanotechnology* **25**, 455601 (2014).

[127] J. S. Lee, T. Kim, H. Song, M. Lee, D. H. Jeong, J.-B. Yoo, T. J. Kang, Y. H. Kim, Binder-free, high-performance carbon nanotube line emitters fabricated using mechanical clamping process. *J. Alloys Compd.* **626**, 287 (2015).

[128] N. S. Ramgir, I. S. Mulla, K. Vijayamohanan, D. J. Late, A. B. Bhise, M. A.

More, D. S. Joag, Ultralow threshold field emission from a single multipod structure of ZnO. *Appl. Phys. Lett.* **88**, 042107 (2006).

[129] A. B. Bhise, D. J. Late, P. S. Walke, M. A. More, V. K. Pillai, I. S. Mulla, D. S. Joag, Sb-doped SnO2 wire: Highly stable field emitter. *J. Cryst. Growth* **307**, 87 (2007).

[130] S. R. Suryawanshi, P. K. Bankar, M. A. More, D. J. Late, Vapour-liquid-solid growth of one-dimensional In2Se3 nanostructures and their promising field emission behaviour. *RSC Adv.* **5**, 65274 (2015).

[131] D. Late, M. More, S. Sinha, K. Dasgupta, P. Misra, B. N. Singh, L. Kukreja, S. Bhoraskar, D. Joag, Synthesis and characterization of LaB6 thin films on tungsten, rhenium, silicon and other substrates and their investigations as field emitters. *Appl. Phys. A* **104**, 677 (2011).

[132] D. Late, R. Kashid, C. Sekhar Rout, M. More, D. Joag, Low threshold field electron emission from solvothermally synthesized WO2.72 nanowires. *Appl. Phys. A* **98**, 751 (2010).

[133] D. S. Joag, D. J. Late, U. D. Lanke, Field emission from a-GaN films deposited on Si (100). *Solid State Commun.* **130**, 305 (2004).

[134] S. R. Suryawanshi, P. S. Kolhe, C. S. Rout, D. J. Late, M. A. More, Spectral analysis of the emission current noise exhibited by few layer WS2 nanosheets emitter. *Ultramicroscopy* **149**, 51 (2015).

[135] R. V. Kashid, D. J. Late, S. S. Chou, Y.-K. Huang, M. De, D. S. Joag, M. A. More, V. P. Dravid, Enhanced Field-Emission Behavior of Layered MoS2 Sheets. *Small* **9**, 2730 (2013).

[136] K. K. Naik, R. Khare, D. Chakravarty, M. A. More, R. Thapa, D. J. Late, C. S. Rout, Field emission properties of ZnO nanosheet arrays. *Appl. Phys. Lett.* **105**, 233101 (2014).

[137] M. S. Pawar, P. K. Bankar, M. A. More, D. J. Late, Ultra-thin V2O5 nanosheet based humidity sensor, photodetector and its enhanced field

emission properties. *RSC Adv.* **5**, 88796 (2015).

[138] M. B. Erande, S. R. Suryawanshi, M. A. More, D. J. Late, Electrochemically Exfoliated Black Phosphorus Nanosheets – Prospective Field Emitters. *Eur. J. Inorg. Chem.* **2015**, 3102 (2015).

[139] N. Kusha Kumar, T. K. Ruchita, V. G. Rogerio, A. M. Mahendra, T. Ranjit, J. L. Dattatray, R. Chandra Sekhar, Enhanced electron field emission from NiCo 2 O 4 nanosheet arrays. *Mater. Res. Express* **2**, 095011 (2015).

[140] L. Jiang, T. Yang, F. Liu, J. Dong, Z. Yao, C. Shen, S. Deng, N. Xu, Y. Liu, H.-J. Gao, Controlled Synthesis of Large-Scale, Uniform, Vertically Standing Graphene for High-Performance Field Emitters. *Adv. Mater.* **25**, 250 (2013).

[141] Z.-S. Wu, S. Pei, W. Ren, D. Tang, L. Gao, B. Liu, F. Li, C. Liu, H.-M. Cheng, Field Emission of Single-Layer Graphene Films Prepared by Electrophoretic Deposition. *Adv. Mater.* **21**, 1756 (2009).

[142] H. J. Jeong, H. D. Jeong, H. Y. Kim, S. H. Kim, J. S. Kim, S. Y. Jeong, J. T. Han, G.-W. Lee, Flexible Field Emission from Thermally Welded Chemically Doped Graphene Thin Films. *Small* **8**, 272 (2012).

[143] R. T. Khare, R. V. Gelamo, M. A. More, D. J. Late, C. S. Rout, Enhanced field emission of plasma treated multilayer graphene. *Appl. Phys. Lett.* **107**, 123503 (2015).

[144] R. Khare, D. B. Shinde, S. Bansode, M. A. More, M. Majumder, V. K. Pillai, D. J. Late, Graphene nanoribbons as prospective field emitter. *Appl. Phys. Lett.* **106**, 023111 (2015).

[145] C. S. Rout, P. D. Joshi, R. V. Kashid, D. S. Joag, M. A. More, A. J. Simbeck, M. Washington, S. K. Nayak, D. J. Late, Enhanced field emission properties of doped graphene nanosheets with layered SnS2. *Appl. Phys. Lett.* **105**, 043109 (2014).

[146] C. S. Rout, P. D. Joshi, R. V. Kashid, D. S. Joag, M. A. More, A. J.

Simbeck, M. Washington, S. K. Nayak, D. J. Late, Superior Field Emission Properties of Layered WS2-RGO Nanocomposites. *Sci. Rep.* **3**, 3282 (2013).

[147] Y. Zhang, J. Du, S. Tang, P. Liu, S. Deng, J. Chen, N. Xu, Optimize the field emission character of a vertical few-layer graphene sheet by manipulating the morphology. *Nanotechnology* **23**, 015202 (2012).

[148] A. Malesevic, R. Kemps, A. Vanhulsel, M. P. Chowdhury, A. Volodin, C. V. Haesendonck, Field emission from vertically aligned few-layer graphene. *J. Appl. Phys.* **104**, 084301 (2008).

[149] S. K. Behura, I. Mukhopadhyay, A. Hirose, Q. Yang, O. Jani, Vertically oriented few-layer graphene as an electron field-emitter. *Phys. Status Solidi A* **210**, 1817 (2013).

[150] M. Qian, T. Feng, H. Ding, L. Lin, H. Li, Y. Chen, Z. Sun, Electron field emission from screen-printed graphene films. *Nanotechnology* **20**, 425702 (2009).

[151] C. Wu, F. Li, Y. Zhang, T. Guo, Field emission from vertical graphene sheets formed by screen-printing technique. *Vacuum* **94**, 48 (2013).

[152] J. Liu, B. Zeng, Z. Wu, H. Sun, Enhanced Field Electron Emission of Graphene Sheets by CsI Coating after Electrophoretic Deposition. *ACS Appl. Mater. Inter.* **4**, 1219 (2011).

[153] J. Chen, L. Cui, D. Sun, B. Yang, J. Yang, X. Yan, Enhanced field emission properties from aligned graphenes fabricated on micro-hole patterned stainless steel. *Appl. Phys. Lett.* **105**, 213111 (2014).

[154] H. J. Jeong, H. Y. Kim, H. D. Jeong, S. Y. Jeong, J. T. Han, G.-W. Lee, Arrays of vertically aligned tubular-structured graphene for flexible field emitters. *J. Mater. Chem.* **22**, 11277 (2012).

[155] T. T. Baby, S. Ramaprabhu, Cold field emission from hydrogen exfoliated graphene composites. *Appl. Phys. Lett.* **98**, 183111 (2011).

[156] H. Y. Kim, S. Jeong, S. Y. Jeong, K.-J. Baeg, J. T. Han, M. S. Jeong, G.-W. Lee, H. J. Jeong, Chemically doped three-dimensional porous graphene monoliths for high-performance flexible field emitters. *Nanoscale* **7**, 5495 (2015).

[157] A. T. T. Koh, Y. M. Foong, L. Pan, Z. Sun, D. H. C. Chua, Effective large-area free-standing graphene field emitters by electrophoretic deposition. *Appl. Phys. Lett.* **101**, 183107 (2012).

[158] Y. Wei, L. Xiao, F. Zhu, L. Liu, J. Tang, P. Liu, S. Fan, Cold linear cathodes with carbon nanotube emitters and their application in luminescent tubes. *Nanotechnology* **18**, 325702 (2007).

[159] M. Croci, I. Arfaoui, T. Stöckli, A. Chatelain, J.-M. Bonard, A fully sealed luminescent tube based on carbon nanotube field emission. *Microelectron. J.* **35**, 329 (2004).

[160] J.-M. Bonard, T. Stockli, O. Noury, A. Chatelain, Field emission from cylindrical carbon nanotube cathodes: Possibilities for luminescent tubes. *Appl. Phys. Lett.* **78**, 2775 (2001).

[161] R. H. Fowler, L. Nordheim, Electron Emission in Intense Electric Fields. *Proceedings of the Royal Society of London A: Mathematical, Physical and Engineering Sciences* **119**, 173 (1928).

[162] Z. Wang, Alignment of graphene nanoribbons by an electric field. *Carbon* **47**, 3050 (2009).

[163] M. Hirakawa, S. Sonoda, C. Tanaka, H. Murakami, H. Yamakawa, Electron emission properties of carbon nanotubes. *Appl. Surf. Sci.* **169–170**, 662 (2001).

[164] K. W. Wong, X. T. Zhou, F. C. K. Au, H. L. Lai, C. S. Lee, S. T. Lee, Field-emission characteristics of SiC nanowires prepared by chemical-vapor deposition. *Appl. Phys. Lett.* **75**, 2918 (1999).

[165] R. V. Kashid, M. Z. Yusop, C. Takahashi, G. Kalita, L. S. Panchakarla, D. S.

Joag, M. A. More, M. Tanemura, Field emission characteristics of pristine and N-doped graphene measured by in-situ transmission electron microscopy. *J. Appl. Phys.* **113**, 214311 (2013).

[166] E. Stratakis, G. Eda, H. Yamaguchi, E. Kymakis, C. Fotakis, M. Chhowalla, Free-standing graphene on microstructured silicon vertices for enhanced field emission properties. *Nanoscale* **4**, 3069 (2012).

[167] Z. Yu, D. Jiale, T. Shuai, L. Pei, D. Shaozhi, C. Jun, X. Ningsheng, Optimize the field emission character of a vertical few-layer graphene sheet by manipulating the morphology. *Nanotechnology* **23**, 015202 (2012).

[168] J. Dong, B. Zeng, Y. Lan, S. Tian, Y. Shan, X. Liu, Z. Yang, H. Wang, Z. F. Ren, Field Emission from Few-Layer Graphene Nanosheets Produced by Liquid Phase Exfoliation of Graphite. *J. Nanosci. Nanotechnol.* **10**, 5051 (2010).

[169] Q. Huang, G. Wang, L. Guo, Y. Jia, J. Lin, K. Li, W. Wang, X. Chen, Approaching the Intrinsic Electron Field-Emission of a Graphene Film Consisting of Quasi-Freestanding Graphene Strips. *Small* **7**, 450 (2011).

[170] M. M. Waldrop, The chips are down for Moore's law. *Nature* **530**, 144 (2016).

[171] M. R. Krames, O. B. Shchekin, R. Mueller-Mach, G. O. Mueller, L. Zhou, G. Harbers, M. G. Craford, Status and Future of High-Power Light-Emitting Diodes for Solid-State Lighting. *J. Disp. Technol.* **3**, 160 (2007).

[172] N. Narendran, Y. Gu, Life of LED-based white light sources. *J. Disp. Technol.* **1**, 167 (2005).

[173] K. M. F. Shahil, A. A. Balandin, Graphene–Multilayer Graphene Nanocomposites as Highly Efficient Thermal Interface Materials. *Nano Lett.* **12**, 861 (2012).

[174] S. H. Song, K. H. Park, B. H. Kim, Y. W. Choi, G. H. Jun, D. J. Lee, B.-S. Kong, K.-W. Paik, S. Jeon, Enhanced Thermal Conductivity of Epoxy–

Graphene Composites by Using Non-Oxidized Graphene Flakes with Non-Covalent Functionalization. *Adv. Mater.* **25**, 732 (2013).

[175] Z. Yan, G. Liu, J. M. Khan, A. A. Balandin, Graphene quilts for thermal management of high-power GaN transistors. *Nat. Commun.* **3**, 827 (2012).

[176] J. Zhang, G. Shi, C. Jiang, S. Ju, D. Jiang, 3D Bridged Carbon Nanoring/Graphene Hybrid Paper as a High-Performance Lateral Heat Spreader. *Small* **11**, 6197 (2015).

[177] Y. Zhang, H. Han, N. Wang, P. Zhang, Y. Fu, M. Murugesan, M. Edwards, K. Jeppson, S. Volz, J. Liu, Improved Heat Spreading Performance of Functionalized Graphene in Microelectronic Device Application. *Adv. Funct. Mater.* **25**, 4430 (2015).

[178] C.-T. Hsieh, C.-E. Lee, Y.-F. Chen, J.-K. Chang, H.-s. Teng, Thermal conductivity from hierarchical heat sinks using carbon nanotubes and graphene nanosheets. *Nanoscale* **7**, 18663 (2015).

[179] E.-C. Cho, J.-H. Huang, C.-P. Li, C.-W. Chang-Jian, K.-C. Lee, Y.-S. Hsiao, J.-H. Huang, Graphene-based thermoplastic composites and their application for LED thermal management. *Carbon* **102**, 66 (2016).

[180] F. Santagata, G. Almanno, S. Vollebregt, C. Silvestri, G. Q. Zhang, P. M. Sarro, Carbon Nanotube based heat-sink for solid state lighting. *Nano/Micro Engineered and Molecular Systems (NEMS), 2013 8th IEEE International Conference on*, 1214 (2013).

[181] Y. Fu, T. Wang, J. Liu, X. Wang, Y. Zhang, Carbon nanotubes as cooling fins in microelectronic systems. *Nanotechnology, 2009. IEEE-NANO 2009. 9th IEEE Conference on*, 44 (2009).

[182] X. Wang, H. Liu, J. Wang, W. Zhang, Z. Li, Package heat dissipation with integrated carbon nanotube micro heat sink. *Electronic Packaging Technology & High Density Packaging, 2009. ICEPT-HDP '09. International Conference on*, 73 (2009).

[183] K. Kordás, G. Tóth, P. Moilanen, M. Kumpumäki, J. Vähäkangas, A. Uusimäki, R. Vajtai, P. M. Ajayan, Chip cooling with integrated carbon nanotube microfin architectures. *Appl. Phys. Lett.* **90**, 123105 (2007).

초 록

거시적 규모의 3차원 그래핀 구조체는 넓은 표면적, 높은 공극률, 우수한 전기화학 특성을 요구하는 다양한 응용분야에 활용이 기대된다. 3차원 그래핀 구조체는 에너지 수집장치, 커패시터, 배터리, 신축성 전자소자, 센서, 세포 성장 지지대, 오일 흡수체 등의 응용분야에서 기존 재료 및 장치에 비해 우수한 성능을 나타내고 있다.

본 논문에서는 금속이온-산화그래핀 결합에 기반한 3차원 그래핀 구조체 제작방법인 이온결합 조립법을 개발하였다. 전압에 의해 산화그래핀 용액으로 용해된 금속이온이 3차원 금속-산화그래핀 결합 네트워크(metal-graphene oxide coordination network, MGCN)를 형성하는 원리를 규명하고, 공정변수에 따른 기계적, 화학적 물성 변화에 관한 연구를 수행하였다.

금속기판에 형성된 3차원 그래핀 구조체는 기존에 보고되지 않은 다양한 응용분야에 활용이 가능하다. 본 논문에서는 MGCN의 선택적 모세관 현상, 높은 전계집중 현상, 우수한 대류 열전달 특성을 분석하고, 각 특성에 적합한 응용분야에 MGCN을 적용하였다.

금속메쉬에 형성된 MGCN을 기름만 선택적으로 통과시키는 분리막으로 사용하여, 바다에 유출된 기름을 자동으로 회수하는 장치를 제작하였다. 이 장치는 99.9% 이상의 순도를 갖는 기름을 20,000 LHM의 빠른 속도로 회수하였다. 금속선 및 금속판에 형성된 MGCN을 이용해 원통형

및 평면 전계 방출소자를 제작하고 전계방출 특성을 분석하였다. MGCN 표면의 수많은 그래핀 모서리에 의해 높은 향상계수 및 낮은 문턱전계를 나타내었다. 금속판에 형성된 MGCN을 방열소자로 사용하여 대류에 의한 방열 특성을 분석하였다. MGCN은 금속판에 비해 36% 향상된 열전달 계수를 나타내었다.

주요어: 겔화, 이온결합 조립법, 그래핀, 3차원 구조체, 결합 네트워크, 금속-산화그래핀 결합

학 번: 2008-20727